SIMULATION OF MECHANICAL BEHAVIOUR OF PURE TITANIUM

SIMULATION OF MECHANICAL BEHAVIOUR OF PURE TITANIUM

By SHU DENG, B.ENG.

A Thesis

Submitted to the School of Graduate Studies

In Partial Fulfillment of the Requirements

For the Degree

Master of Applied Science

McMaster University

Masters of Applied Science
(Mechanical Engineering)

McMaster University
Hamilton, Ontario

TITLE: Simulation of Mechanical Behaviour of Pure Titanium

AUTHOR: Shu Deng, B.ENG. (Shanghai Jiao Tong University)

SUPERVISOR: Professor P.D. Wu

NUMBER OF PAGES: xi, 140

ABSTRACT

Titanium is a widely applied material in industries and characterized by highly anisotropic mechanical behaviour. To study the special property of titanium, many kinds of mechanical loading tests have been conducted. Moreover, researchers attempted to reproduce these experiments with numerical methods. This paper will present an overview about the deformation mechanisms and related representative studies of titanium.

Among the numerical methods, Taylor type and self-consistent crystal plasticity models are two of the most common ones seen in literature. Simulation of some mechanical loading tests using visco-plastic self-consistent model was carried out and compared with the results given by Taylor type model. It has been found that self-consistent model prevails in the reproduction of stress-strain response and texture evolution.

During the calculation of self-consistent model, there are totally 4 kinds of self-consistent schemes available for linearization process. The author investigated 4 groups of simulation works using different self-consistent schemes. But no evident distinction has been observed.

The application of visco-plastic self-consistent model in commercial purity titanium is studied at the end. The simulation results successfully captured the general features of 9 mechanical loading tests.

ACKNOWLEDGEMENT

I would like to present my sincerest gratitude to my supervisor Dr. Wu for his inspiring advice, patient instruction and motivational encouragement. The best fortune Dr. Wu has given to me is the method of solving problems independently. I could never manage to accomplish this master program without his kind guidance and incredible patience.

Thanks to those researchers whose studies provided much essential data for my thesis. They are: the research group of S. R. Kalidindi, the research group of R. Lebensohn and the research group of S. Bouvier.

I also would like to thank Dr. Jain and Dr. Ng for their insightful suggestions about my thesis in our discussion.

Many thanks to my colleagues in research group: Hua Qiao, Xiaoqian Guo, Yue Fu and Hanqing Ge for your support and selfless help. You are my best teammates and best friends during the hardest period of my life.

Special thanks to my girlfriend Mengmeng Lou and my parents, who gave much power and love to fulfill my work. You are my beloved family. I will keep fighting for our better future to make you proud.

TABLE OF CONTENTS

LIST OF FIGURES

LIST OF TABLES

LIST OF ABBREVIATIONS

BCC	body-centred cubic
CDC	channel die compression
CG	composite grain
CP-Ti	commercial purity titanium
CRSS	critical resolved shear stress
DHP	dynamic Hall-Petch
DSA	dynamic strain aging
EBSD	electron back-scatter diffraction
ECAP	equal channel angular pressing
EVPSC	elastic-viscoplastic self-consistent
FC	full constraints
FCC	face-centered cubic
FEA	finite element analysis
HCP	hexagonal close-packed
HEM	homogeneous effective medium
HP-Ti	high purity titanium
MC	Monte Carlo
MTS	Mechanical Threshold Stress
ND	normal direction
OIM	orientation imaging microscopy
OM	optical microscopy
PTR	predominant twin reorientation
PTS	predominant twin system
RC	relaxed constraints
RD	rolling direction
RRSS	relative resolved shear stress
RSS	resolved shear stress
SC	self-consistent
TD	transverse direction
TEM	transmission electron microscopy
TT	through-thickness
VFT	volume fraction transfer
VPSC	visco-plastic self-consistent

Chapter 1 Introduction

1.1 Motivation and Objectives

Titanium and its alloy are widely applied materials in industries. However, there are still various questions unsolved in this field. For high purity titanium (HP-Ti), Kalidindi et al. have carried out simulation works [Salem et al., 2005; Wu et al., 2007] based on their own experimental results of HP-Ti with Taylor type model and claimed better outcome should be obtained with self-consistent (SC) model. Besides the question of whether SC model can lead to improved results, it also interests the researcher which one of the SC schemes gives the best prediction. This question has been addressed with other materials [Wang et al., 2010a], but not titanium. Meanwhile, in the research field of deformation mechanisms in titanium, there are arguments about the existence and function of basal <a> slip mode in polycrystalline HP-Ti. The author tried to study into these questions with numerical method.

For commercial purity titanium (CP-Ti), Benmhenni et al. have conducted a series of uniaxial loading and simple shear tests [Benmhenni et al., 2013]. They also presented their simulation results with poor quality. Their experiments provided the author of this thesis a great chance to carry out a simulation work that takes 9 different mechanical tests into account at the same time, which has not been done by others to the best of the author's knowledge. So the objectives of the author's research are:

(1) Conduct a simulation work and to confirm the superiority of SC models to Taylor type models.

(2) Conduct simulations with different SC schemes and find out which of them works

best in the cases of titanium.

(3) Conduct a simulation work taking basal <a> mode into account and compare the result with that having basal <a> mode eliminated.

(4) Conduct a simulation work with 9 different mechanical tests reproduced at the same time and evaluate the results.

1.2 Thesis Outline

In this Chapter, the motivation and objectives of this thesis have been illustrated.

Chapter 2 will present a brief introduction to titanium and numerical methods applied to study this material. At the same time, the author will give the reader a comprehensive literature review on deformation behaviour of titanium. Both mechanical tests and simulation works of this material will be presented.

In Chapter 3, a simulation work of HP-Ti with self-consistent model applied is shown. A comparison between the author's result and that of another research group will reveal the difference between self-consistent model and Taylor type model.

In Chapter 4, the author will present a general discussion of which self-consistent scheme leads to the best simulation result in the research field of titanium. Meanwhile, through the comparison between the works of the author and others, the role of basal<a> is summarized.

Lastly, a systematic series of mechanical tests of CP-Ti will be simulated in Chapter 5. With the analysis of the results, the role played by the twinning mode in simple shear tests will be discussed.

All the conclusions will be summarized in Chapter 6 at the end.

Chapter 2 Literature Review

2.1 Overview of Titanium

Titanium has been found and used for more than 200 years. It is used extensively in many industrial products. As its name comes from “Titan” in the ancient myth, titanium and its alloys have many attractive material properties which many other metals or alloys cannot match. For examples, its low density, high strength and excellent corrosion resistance [Lütjering et al., 2007] make titanium one of the most favoured materials in aircraft, biomedical and many other industries.

To be specific, titanium is widely utilized in aircraft manufacture, due to its high strength to density ratio. In this way, strong aircraft structure can be obtained with less weight gained in the same time [Teixeira et al., 2007; Adib et al., 2007]. Also, in the aero-engines, titanium shows excellent performance for its high creep resistance up to 550℃ [Wang et al., 2008]. In the biomedical devices, titanium has good corrosion resistance, low Young’s modulus, high strength and impressive biocompatibility [Rack et al., 2006; Liu et al., 2004].

However, the application of titanium is restricted for its high cost relative to aluminium, iron and many other common metal materials. The high cost of titanium comes from not only the price of raw material, but also from the low efficiency and other manufacturing problems during the processing of titanium. Therefore, a more comprehensive understanding of titanium and its deformation mechanism is extremely desirable to make good use of this material by providing a balance between the structure performance and the cost for processing as compared to other relatively cheaper metals.

The production cost is an important consideration in the manufacturing industries, such as in the production of automobiles and aerospace structures. In aero-engines, the utilization of titanium can reduce the equipment weight by 25% [Lütjering et al., 2007], which is very attractive for fuel efficiency. Also, consumer products such as cameras, jewelry and sports equipments like golf clubs and bicycles are emerging as a large market for titanium, since many people are concerned more with the quality and durability of the product they use rather than the price.

In this thesis, the research work is focused on pure titanium materials which usually can be classified into two main types, HP-Ti and CP-Ti. The author has not found the official definition of HP-Ti (this may due to their limited application in industries). However, based on related literature, the concentration of titanium in the HP-Ti generally is higher than 99.999%. For CP-Ti, the leading 4 grades (Grade 1 to Grade 4) out of 31 grades of titanium and its alloys recognized by the American Society for Testing and Materials (ASTM) International are commercially pure, which means they are unalloyed. Generally, the purity of CP-Ti is higher than 99.2%. Different grades are distinguished by the varying tensile strength as a function of oxygen content. Grade 4 CP-Ti contains the most impurities with an oxygen content of 0.40% [Emsley & John, 2001].

2.2 Properties of Titanium

This section presents a review of the literature on the crystallography of α-titanium. This thesis is restricted to α-titanium, for it is the only structure discussed and studied in this project. Therefore, in the rest of the thesis, α-titanium will be referred to as titanium for simplicity.

2.2.1 Basic Physical Properties

The density of pure titanium is 4.507g/cm^3 at room temperature, which is between the density of aluminium and iron. However, the melting point of titanium is higher than iron, which is 1670℃. The higher melting point also leads to a wider range of application than other materials. At room temperature, titanium usually remains as hexagonal close-packed (HCP) structure, which is called alpha-titanium. When the temperature reaches 882.5℃ or above, it turns into β-titanium with body-centred cubic (BCC) structure. This process is called allotropic transformation. For alpha-titanium, the c/a ratio (1.587) of HCP structure is lower than the ideal 1.633 [Partridge, 1967], this leads to much complicated deformation behaviors of titanium as was earlier believed. In fact, the better ductility of titanium than other HCP metals comes from the fact that titanium has more densely packed lattice planes as described in the following and they are all easily activated.

2.2.2 Deformation Mechanisms

Deformation mechanism is rather complex in titanium as it has a HCP structure. Besides large amounts of slip and twinning modes, the interaction between these mechanisms and slip formation in the shear bands at high strains make the analysis significantly harder than the metals with cubic unit cell. Among those slip and twinning modes, it should be noted that the slip modes with direction of <a> component cannot accommodate the strains along c-axis alone. The <c+a> slip modes or the twinning modes must exist in the c-axis strain situation. In this chapter, a review of slip in single crystal, polycrystal and twinning of titanium is presented separately.

2.2.2.1 Slip in Single Crystal

Slip Modes

In α phase, which is stable at room temperature, the most densely packed lattice planes are the three $\{10\bar{1}0\}$ prismatic planes. Other densely packed lattice planes are basal $\{0001\}$ planes and $\{10\bar{1}0\}$ first-order pyramidal planes. The most compact directions are$< 11\bar{2}0 >$. They are also the basis vectors of HCP coordinate system. The fact that highest density planes are $\{10\bar{1}0\}$ prismatic planes is due to the c/a ratio of titanium. But not all HCP metals with such c/a ratio have the ductility that is superior to titanium, such as magnesium (1.624) and beryllium (1.567). Naka et al. [Naka et al., 1991] suggest that the easiest deformation modes in titanium come from the core structure of <a> type screw dislocations and depend on the electronic structure further. The <a> screw dislocations require less energy to move on the prismatic planes of titanium than other HCP metals. This gives α-titanium relatively high ductility.

In addition, interactions between slip and twinning lead to high elastic strength and high level of hardness as well.

Figure 2.1 shows the representative slip and twinning systems. Among them, prismatic slip system (P<a>) is the easiest deformation mode which has been confirmed by experimental data and numerical analysis [Legrand, 1985]. Many single crystal studies and data have been carried out on the P<a> and B<a> slip modes because they are most easily activated. Studies involving the single crystal of known orientation allow the researchers to select a dominant mode of deformation during the test. Conrad [Conrad, 1981] has summarised the critical resolved shear stress (CRSS) of the two slip modes in

titanium under different temperatures. The trends of the CRSS are similar for the two slip modes, which decrease rapidly at low temperature until 227℃ (500K). However, the value of CRSS does not change much as temperature increases further till 577℃ (850K). For temperature above 577℃, the CRSS decreases slowly yet non-negligibly, which indicates that the underlying deformation mechanism is continually changing. Although the CRSS trends of P<a> and B<a> slip modes are similar, the decreasing rates are notably different for the two modes. Moreover, the experimental data also reveals difference between these two modes about the dependence on interstitial content. Since the CRSS of P<a> slip mode increases much faster than B<a> slip mode at the same interstitial concentration, the P<a> and B<a> slip mode exhibit similar activity when the material is of low purity.

The Π_1<a> slip mode was reported very early in the titanium deformation [Churchman, 1954; McHargue & Hammond, 1953; Rosi et al., 1953; Rosi et al., 1956] as well as in the transmission electron microscopy (TEM) experiments [Naka et al., 1988]. In these experiments, the researchers also claimed that the slip direction can be <c+a>. Although only the <c+a> type slip modes can accommodate the c-axis strain in the plastic deformation, it is still hard to distinguish the slip planes between Π_1 and Π_2, which have the same slip direction. Williams & Blackburn [Williams et al., 1968] have found <c+a> dislocations distributed in the area between the poles of Π_1 and Π_2 planes with no test conditions provided. They suggested the result could be due to composite slip on these two planes. It is unfortunate that there is still a lack of data about the operation of <c+a> type slip. Cass [Cass, 1968] ran experiments on HP-Ti and CP-Ti compressed in the c-

axis direction. His study shows that twinning is the only active mode accommodating c-axis strain in HP-Ti, while <c+a> slip mode emerges on the Π_1 plane in the CP-Ti sample. In contrast, Paton & Backofen [Paton et al., 1970] discovered evidence of Π_1 plane slip by TEM in the compression experiment along the c-axis direction of single crystal HP-Ti. In their study, Π_1 <c+a> slip mode is much favoured at high temperature (400℃-800℃). At 800℃, even 90% of the strain is accommodated by this mode. Whereas at low temperature (25℃-300℃), Π_1 <c+a> just accommodates the shear ahead of propagating twins instead of a large amount of strain. Π_2 plane slip was found activated alone in titanium at 27℃ in a later research by Minonishi et al. [Minonishi et al., 1982a]. Minonishi et al. [Minonishi et al., 1985] also found both Π_1 and Π_2 <c+a> slips in the study at 600℃ and the Π_2 <c+a> slip was claimed to be the prevailing one. For the room temperature case, Xiaoli et al. [Xiaoli et al., 1994] studied into the underlying mechanism of HP-Ti. They pointed out that Π_2 <c+a> slip is activated after $\{11\bar{2}1\}$ tensile twinning, and then the P<a> slip occurs. Their studies led to the fact that Π_2 <c+a> slip mode is more favored at room temperature than Π_1 <c+a> mode.

Minonishi et al. did further atomic modelling work to study Π_1 <c+a> and Π_2 <c+a> slip modes [Minonishi et al., 1982b; Minonishi et al., 1981; Minonishi et al., 1982c]. They claimed that the $\frac{1}{3} < 11\bar{2}3 >$ screw dislocations glide on the Π_2 plane under c-axis compression, while under c-axis tension they glide on Π_1 planes. In contrast, $\frac{1}{3} < 11\bar{2}3 >$ edge dislocations are always gliding on Π_2 planes. It has to be admitted that their results

are impressive, but the effect of some other factors like the impurities and nucleation of dislocations are still unknown.

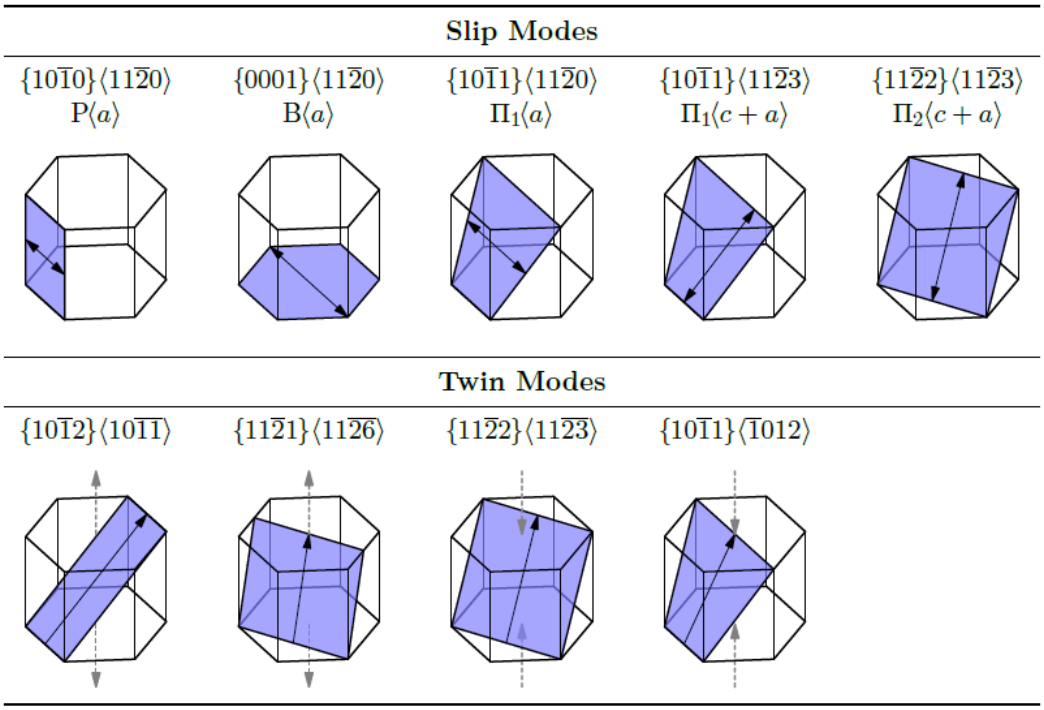

Figure 2.1. Slip and twinning systems in HCP crystals. Black arrows indicate the shear direction which slip systems have two and twinning systems have one. Grey arrows with dashed line indicate loading directions corresponding to tensile or compressive twinning. (Note the sign of Π_1 and Π_2 refer to first-order and second-order pyramidal lattice plane respectively) [Battaini, 2008].

2.2.2.2 Slip in Polycrystal

In the presence of grain boundaries, deformation behavior of polycrystal is significantly different from that in single crystal. The grain boundaries can act as the source of dislocations and the obstacles on the gliding path of them. Consequently, the stress state is greatly changed compared to that in single crystal. Furthermore, the size of the grain in polycrystal and the size of single crystal are always different, which gives rise to the

doubts as to whether the conclusion of single crystal can be applied in polycrystal. Because there are still difficulties in activating slip modes individually to obtain their information, most researches on the deformation mechanisms are semi-quantitative or merely qualitative for polycrystalline titanium.

TEM is an effective tool in studying polycrystal, but only a limited volume of sample can be analyzed with a long specimen preparation time. The space of the TEM apparatus restrains the strain level of the samples as well. However, there is an alternative method of X-ray line broadening. It can analyse the bulk material to get data for bulk deformation that can be applied at large strains. Also, dislocation densities can be obtained in X-ray line broadening as well. However, this method has problems. Researchers need to deconvolute the diffraction profiles. Moreover, the effect of texture is significant in the analysis of the large strain deformation. Also, the slip modes as well as the ratio of the edge to screw dislocation have to be assumed in advance.

Slip Modes

The easily activated slip modes that have already been found in the polycrystalline titanium are similar to those found in single crystal. Most of the investigations are run by TEM and the dominance of <a> type slip, especially the P<a> slip mode has been confirmed [Conrad, 1981; Chichili et al., 1998; Philippe et al., 1995; Shechtman et al., 1973; Williams et al., 1972]. However, it needs to be noted that these tests have textures or loading directions that favour the P<a> slip. Zaefferer [Zaefferer, 2003] has found B<a> and Π_1 <a> as the dominant slip modes instead of P<a> in their experiments, which is due to the low resolved shear stress for P<a>.

As for the <c+a> type slip modes, different test conditions lead to different investigation results as well. Shechtman & Brandon [Shechtman et al., 1973] found that there are not as many <c+a> type dislocations in polycrystal as those in single crystal of titanium because the texture of the sheet used in their experiments may not favour this slip mode. In other tests [Numakura et al., 1986; Pchettino et al., 1992], large amounts of Π_1 <c+a> dislocations were found in room temperature. Both studies were run with tension in the axial direction of a titanium rod and oxygen atmosphere was used to suppress twinning. The c-axes of the sample are aligned vertical to the axis of the rod, which is favourable for Π_1 <c+a> slip mode to activate. Among the various researchers, only few people have reported the observation of Π_2 <c+a>, such as Zaefferer [Zaefferer, 2003]. This indicates that Π_1<c+a> is preferred in the polycrystal deformation more than the Π_2 <c+a> slip mode.

Numakura et al. [Numakura et al., 1986] supported the preference of Π_1<c+a> mode and attribute the good ductility of titanium and zirconium to this favoured slip mode, while other HCP metals that favour Π_2<c+a> slip mode have poor ductility. They also claimed that Π_1<c+a> slip mode makes more contribution to the ductility than twinning. However, later research [Paton et al., 1970] shows that only $\{11\bar{2}2\}$ twinning can also cause good ductility in the single crystal titanium. Zaefferer [Zaefferer, 2003] has given an explanation to this by using a Sachs model calculation. Their results show lower CRSS of Π_1<c+a> slip mode in T40 alloy than T60 may cause the higher ductility in T40. Their research also pointed out that other predominant slip modes act in the same way. So the

change of CRSS may be a potential reason affecting the underlying mechanism in deformation.

The deformation process of titanium can be separated into different stages with apparently distinct behaviours. Between each adjacent stage, it is believed that the underlying mechanisms are changing and cause different strain hardening rates. However, it is not easy to distinguish the slip modes in the observation. Philippe et al. [Philippe et al., 1995] showed qualitative data about the evolution of slip modes during deformation in the rolling of T35 alloy at room temperature. At the beginning, P<a> slip dominates the deformation with little Π_1<a> and B<a> slip modes existing. Therefore, the activation of $\{10\bar{1}2\}$ and $\{11\bar{2}2\}$ twinning were observed. The <c+a> slip modes arise at the saturation of the twinning. In another test [Glavicic et al., 2004], the researchers have observed similar behaviours of deformation modes and provided their relative activities of T60 alloy, which were used to estimate CRSS for numerical calculations afterwards. However, the results of the simulation with the estimated CRSS from the experiment show disparity with the observation.

Slip Mode Activity

Since TEM is not an ideal method to study the dislocation activity in bulk material and most TEM experiments were done under the condition of low strain, only the X-ray line broadening tests will be discussed in this section.

Glavicic et al. [Glavicic et al., 2004] have done research into CP-Ti and their investigation systematically analysed the effect of temperature on polycrystalline titanium. Their results show that P<a> slip and <c+a> slip modes dominate the deformation with

no B<a> activated over a temperature range of 20-720℃. It appears that P<a> and <c+a> slip modes accommodate the strain and B<a> is absent over all temperatures. This result is not accordance with the prediction from single crystal CRSS values and also the identification of B<a> in other TEM experiments [Philippe et al., 1995; Zaefferer, 2003]. Glavicic also ran TEM in their experiment. The observation shows a homogeneous distribution of <a> and <c+a> dislocations, but the B<a> has not been identified among the <a> type slips. Moreover, the exact slip type of <c+a> remains unknown in all the studies above.

Dragomir et al. [Dragomir et al., 2005] extracted the dislocation activity over a wide range of strains. Their tests were conducted with CP-Ti under rolling deformation. They did not distinguish the <a> type modes in their study. Their results show that <c+a> slip modes have made a notable contribution to the deformation, while <a> slip mode is still the main deformation mode at all reductions. The activity of <c+a> slip mode decreases with the growth of reduction and the concentration of $< \bar{2}113 >$ poles parallel to the RD goes down. There are also a small amount of <c> type dislocations that have been involved during the growth of twinning [Song & Gray, 1995c]. However, in the experiment mentioned before [Glavicic et al., 2004], similar dislocation activities have been found in different reductions. Therefore, there is no significant change in the dislocations at different stages of deformation. The contradiction between these studies may result from the experimental differences.

2.2.2.3 Twinning

In HCP materials, twinning is reported to play a significant role in the deformation behaviour, especially in accommodating the c-axis strain. The twinning mechanism contributes significantly to the ductility and strain hardening of titanium, which will be discussed in detail later.

Twin Modes

The twin modes in titanium were identified very early like slip modes in the initial studies of this material [McHargue & Hammond, 1953; Rosi et al., 1953; Rosi et al., 1956; Rosi, 1954]. However, further studies appeared to be impeded for some reason for quantifying the details of this kind of mechanism in titanium. Most of the studies were conducted at room temperature and limited to a narrow range of conditions, such as temperatures, impurities and so on. The commonly observed twin modes are listed in Table 2.1.

$\{10\bar{1}2\}$ and $\{11\bar{2}2\}$ are the two most common modes of twinning in c-axis tension and compression according to the experimental investigation. These two modes are mostly found at and below the room temperature. At higher temperatures, $\{10\bar{1}1\}$ twinning mode are activated but not as the dominant deformation mode.

As for the effect of temperatures on the change of twining modes, the research of Paton & Backofen [Paton & Backofen, 1970] is noteworthy. From their observation, $\{11\bar{2}2\}$ compressive twinning mode accommodates the most strain from 25-300℃ in c-axis compression tests. However, the activity decreases with an increase in temperature. From 400 to 800℃, only the $\{10\bar{1}1\}$ compressive twinning was found and also decreased with increasing temperature. Also, a small amount of $\{11\bar{2}4\}$ twinning mode was identified in

the deformation. Experiments of this work were done in HP-Ti single crystal, while similar data of polycrystal has been rarely published.

Glavicic et al. [Glavicic et al., 2004] have made measurement of the twin volume fraction at a range of temperatures. However, the individual volume fraction of different twin modes was only measured at room temperature separately. The individual twin mode was identified by electron back-scatter diffraction (EBSD) method. Glavicic et al. have found that no twinning is activated above 315℃. However, Kim et al. [Kim et al., 2003] claimed that $\{10\bar{1}1\}$ twinning mode plays an important role in the severe equal channel angular pressing (ECAP) at 350℃. The different experimental conditions may have caused contradictory conclusions.

Table 2.1.
Twinning modes commonly observed in experiments of α-titanium and the corresponding temperature range reported in literature to date.

Twinning Type	Twin Mode	Temperature Range
Tensile	$\{10\bar{1}2\}<10\bar{1}\bar{1}>$	-196 to 800℃
	$\{11\bar{2}1\}<11\bar{2}\bar{6}>$	-196 to 25℃
	$\{11\bar{2}3\}<11\bar{2}\bar{2}>$	-196 to 25℃
Compressive	$\{11\bar{2}2\}<11\bar{2}\bar{3}>$	-196 to 300℃
	$\{10\bar{1}1\}<\bar{1}012>$	25 to 800℃
	$\{11\bar{2}4\}<11\bar{2}\bar{3}>$	-196 to 800℃

Another factor that influences the twinning mode activity is the orientation and specifically, the relationship between the stress state and the texture. Mullins & Patchett [Mullins & Patchett, 1981] approximately determined the ratios of different twinning modes for several stress conditions. Their results show that $\{10\bar{1}2\}$ twinning mode is

favored in the tension test, in which c-axes are less than $50°$ to the tension axis. In contrast, the $\{11\bar{2}2\}$ and $\{11\bar{2}4\}$ twinning modes were found in c-axis compression.

Twin Evolution

The twin area fraction with increasing strain is a common pattern studied for the evolution of twinning. Most data of this nature is measured at room temperature and generally shows that the twin area faction increases rapidly with a falling rate to saturation. Some of the researchers claimed that the twinning saturation occurs at $\varepsilon \approx 0.3$ [Philippe et al. 1995, Salem et al., 2003a]. Salem et al. [Salem et al., 2006] gave two explanations for the twinning saturation process:

(1) The texture is changed by the twinning which will be no longer needed to accommodate the strain in further deformation.

(2) The twinning boundaries make it more difficult to further form twins.

However, there is one possibility existing that makes the conclusion doubtful. If twinning consumes the entire grains, the situation will be different from what happened earlier. These grains may be neglected as grains that have no twinning, so the accuracy of results can be undermined. Moreover, the occurrence of secondary twinning may also influence the investigation in the same way. In all of published observation, not enough details on the identification of twinning have been provided. In the simulation of the results in Salem et al. [Salem et al., 2003a], the texture component of twinning is weaker in the predicted textures than in the experimental texture. This implies that the values taken in the experiment were underestimated. Also the optical micrographs in Salem et al. [Salem

et al., 2003a] show that at $\varepsilon \approx 0.5$ the microstructure is more fragmented than that at $\varepsilon \approx 0.3$.

Strain rate is one of the most significant factors that influences the twinning activity. It is well known that the increase of strain rate can promote the twinning activation and can also induce deformation modes that do not occur normally in the material [Christian & Mahajan, 1995]. In this way, strain rate can strongly influence the twin evolution. However, compression tests on CP-Ti [Chichili et al., 1998] show that with different strain rates or temperatures, the area fraction of twinning versus stress has the same curve, which gives strong evidence that the stress state is the most essential factor influencing twinning activity. This conclusion matches what was mentioned before, that the different orientations of the c-axis relative to the major stress component lead to different twinning behaviours.

Moreover, Song & Gray [Song & Gray, 1995a] found stress dependence in zirconium, which has similar properties to those of titanium. In their study, the most important discovery was that the onset of twinning occurred at the same stress level at all temperatures, even at higher strain rate. As the temperature goes higher, the stress-strain curve cannot reach the threshold stress and no twinning will be activated. This is a powerful proof that twinning activation stress is independent to temperature and strain rate. Even though the results came from experiments on zirconium, it is quite likely that they are also applicable to titanium.

It is clear that the activation of twinning is generally orientation dependent, but little data has been obtained to quantify this. To establish a CRSS law of twinning, the different

mechanisms of twin nucleation and propagation [Bell & Cahn, 1953] are the biggest challenges. The single crystal test done by Paton & Backofen [Paton & Backofen, 1970] shows that the nucleation stress of $\{11\bar{2}2\}$ twinning is higher than its propagation stress from 0℃ to 300℃. In contrast, for $\{10\bar{1}1\}$ twinning the nucleation stress is less than or equal to the propagation stress from the observation of the stress or load evolution. It is obvious that the nucleation mechanism of polycrystal is different from that of single crystal due to the existence of grain boundaries. However, more attention is still needed in this field.

Song & Gray [Song & Gray, 1995b] came up with a coincidence site lattice model, which can deal with the high velocity movement of twins. Moreover, most factors that affect the operation of a twin mode have been considered. Their model predicts that besides those factors mentioned above, the operation of twinning is related to the local dislocation density, twin step height and lattice mismatch. All these factors may show an explanation for the abnormal CRSS results of twinning.

Serra et al. [Serra & Bacon, 1996] proposed that movement of twinning dislocations is realized by the interaction of twin boundaries and B<a> dislocations, which is the growth mechanism of twinning. However, this model cannot account for the condition of high velocity of twinning. TEM studies by Braisaz et al. [Braisaz et al., 1996] support this dislocation-twin reaction theory, but the B<a> dislocation in titanium remains unproven.

In summary, the understanding of twinning mechanism needs more investigation or observation by appropriate experimental techniques. However, the quantitative data

collection of twinning activity like slip modes in single crystal titanium is still useful in the modelling work on this material.

2.2.2.4 Mechanism of Strain Hardening

It is well known that the strain hardening usually occurs at the beginning of Stage Two (see Section 1.2.3) during deformation. Therefore, it would be useful to find out the dominant mechanism or the evolution of microstructure in this stage. Garde et al. [Grade et al., 1973] pointed out that the second stage begins with an apparent increase of twinning activity in both HP-Ti and CP-Ti. On the other hand, strain hardening in CP-Ti is not as strong as in HP-Ti with a lower twinning activity as well. Moreover, the Stage Three shows decreasing strain hardening rate with the saturation of twinning. All of the evidence listed above strongly supports that strain hardening in Stage Two is caused by twinning. Other researchers have come to the same conclusion with different strain rates, grain sizes and temperatures [Mullins & Patchett, 1981; Salem et al., 2003a; Gray, 1997, Huang et al., 2007; Murayama et al., 1991;Murayama et al., 1987]. In these experiments, the commencement or growth of strain hardening of Stage Two is always concomitant with increasing twinning activity.

The mechanisms of how twin activity affects the strain hardening can be summarized as follows.

(1) Orientation hardening (softening): the twinning changes the orientation of the grain, which makes it easier or harder to activate some modes with further deformation.

(2) Dynamic Hall-Petch (DHP) hardening: the twinning process divides the grains into small regions, which serve as obstacles for deformation modes.

(3) Basinski hardening: twinning changes the structure of matrix, which makes the former glissile dislocations turn into sessile ones and leads to the increase in hardness.

Realistically, one cannot claim that twinning is the only mechanism for strain hardening and even that twinning is an essential mechanism for titanium. It is well known that slip is the most common mechanism of plastic deformation and the effect of twinning always functions with its influence on slip. In this way, twinning may be an indirect factor for strain hardening, but not a negligible factor that can be set aside. On the other hand, at low temperature, titanium with high density of interstitial content usually shows less twinning. However, the strain hardening in Stage Two is still favoured. As for the mechanism causing this, more data and experiments are still required.

Notwithstanding the above, there has been much evidence supporting the important role of twinning mechanism in Stage Two deformation of titanium. The measurements of orientation of twins support the orientation hardening or softening theory [Salem et al., 2006; Murayama et al., 1991;Murayama et al., 1987]. The second theory has been investigated by comparing the experimental with the calculated effective grain sizes. The calculated grain size has been obtained by fitting the strain hardening curve using the Hall-Petch law [Salem et al., 2002]. The result shows that the experimental data is somewhat higher than the calculated one using Hall-Petch law indicating that there is a softening mechanism. However, the trends of both values are similar showing the validity of this mechanism. As for Basinski hardening, the evidence is provided by the measurements of microhardness and nanohardness in the twinning and the surrounding area [Salem et al., 2006].

There is another type of experiment, reload test, which helps to support the twinning mechanism. Chichili et al. [Chichili et al., 1998] did an experiment comparing one CP-Ti sample deformed at -196℃ and reloaded at 25℃ with another sample only loaded at 25℃. In the pre-deformed sample, a lower yield stress and higher strain hardening rate was observed. This can be explained by the orientation softening and the Hall-Petch hardening law [Kalidindi et al., 2003]. Smirnov & Moskalenko [Smirnov & Moskalenko, 2002] did similar experiments on CP-Ti foil, but the results were different. The reloaded sample shows increased flow stress and hardening rate at second loading test. This is due to the texture and test condition favouring the orientation hardening mechanism. They also did an opposite test in which the sample pre-loaded at higher temperature was reloaded at low temperature. The yield stress decreases compared with the sample loaded at -196℃. Since twinning is insignificant above the room temperature, it is possible that the test results are caused by other mechanisms, like evolution of dislocation structure.

However, after doing a similar experiment and getting similar result to Chichili et al. [Chichili et al., 1998], Nemat-Nasser et al. [Nemat-Nasser et al., 1999] proposed that a variation of dynamic strain aging (DSA) mechanism is the reason for the phenomena observed. But Salem et al. [Salem et al., 2003a] showed different opinion to this explanation. First, the Stage Two can be observed at very high strain rates in CP-Ti and below the temperature range in which the DSA mechanism is expected. Second, Stage Two can be found at room temperature in HP-Ti in which DSA effect should be reduced significantly. Nevertheless, Salem et al. [Salem et al., 2003b] still used the DSA to explain some of their experiment results. On the other hand, using the theory of twinning

effect can also explain the experiment results well. It is hard to clarify because they presented little information of twinning. If the results were caused by twinning effect but in a different way, it will highlight an issue that is noteworthy – the simple method of labelling the flow curves may be too subjective to show the essential changes of deformation, because similar mechanism can manifest differently in different conditions.

There is also a conventional way of explaining the strain hardening in Stage Two – the evolution of slip. Akhtar & Teghtsoonian [Akhtar & Teghtsoonian, 1975] did experiment in single crystal HP-Ti which was oriented for P<a> slip. They attributed the Stage Two stain hardening to secondary P<a> slips by the observation. Naka et al. [Naka et al., 1988] supported their results in the experiment of CP-Ti and Naka et al. & Lasalmonie [Naka & Lasalmonie, 1982] also suggested that the Stage Two hardening is due to a cross-slip mechanism, in which the P<a> dislocations dissociate in Π_1<c+a> planes. As for the situation in polycrystal, the different dislocation structures can be correlated to the stages as well [Conrad, 1981]. However, the activity of twinning appears to be ignored in this reference.

It is obvious that the majority of work focused on the second stage of flow curves whereas, the Stage One received little attention. Generally, the parabolic shape of Stage One is supposed to be caused by dynamic recovery, such as in other metals. Competition between the dislocation multiplication and annihilation is the essential part of dynamic recovery [Chichili et al., 1998, Salem et al., 2006]. In the early stages, the dislocation density increases rapidly and the space of slip lines decreases apparently [Rosi et al., 1956; Akhtar & Teghtsoonian, 1975]. The hardening effect in Stage One can be attributed to the

elasto-plastic transition. In this process, the grains never deform plastically together. Instead, those grains favoured by the stress state will reorient first and others will stay at higher stresses and yield later. This is not the traditional plastic deformation just caused by defect interaction. This is an apparent factor that should be noted in the studies of titanium, such as in zirconium [MacEwen et al., 1989] and magnesium [Agnew et al., 2003].

2.2.3 Flow Curves

The flow curve (stress-strain curve) is a macroscopic property of material. It is the result of all deformation mechanisms mentioned above and should be discussed individually, since it is the most common experimental data in the calibration of modelling. Generally, the flow curves of titanium can be divided into three stages as shown in Figure 2.2.

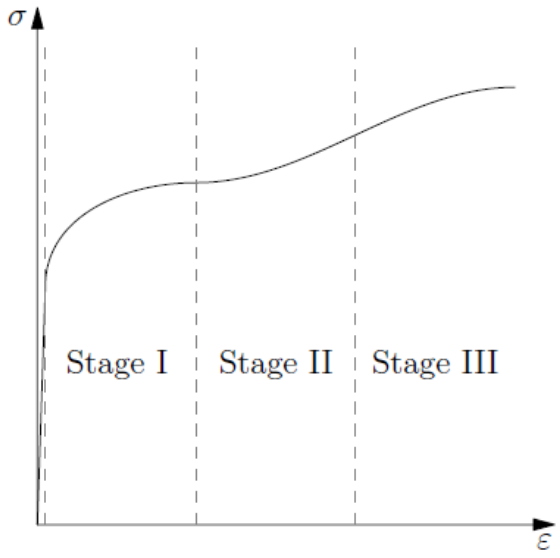

Figure 2.2. General shape of the flow curve of titanium and the definition of three stages according to the strain hardening rate change [Battaini, 2008].

2.2.3.1 Effect of Temperature

The effect of temperature and strain-rate change on the flow curve has been studied in CP-Ti in tension [Döner & Conrad, 1973; Santhanam & Reed-Hill, 1971]. In these studies, the range of strain rate considered is rather small ($\approx 10^{-3}$-$10^{-5} s^{-1}$). In addition, the strain hardening rate is measured in the strain range, ε = 0.005 to 0.05, which can be regarded as largely Stage One. The range of different conditions cannot be regarded as "wide", but still the result revealed a rather complicated relation between strain hardening and temperature. The strain hardening rate stays at high level and decreases slowly from the temperature of -196℃ to 377℃. Then there is a sudden peak which rapidly decreases to 0. The peak is found to be controlled by DSA mechanism. At higher strain-rate, the peak occurs at higher temperature, which indicates that this is a diffusion controlled process. In the rate change experiments [Santhanam & Reed-Hill, 1971], the instantaneous rate change leads to little influence on the flow stress but a significant increase in the subsequent hardening rate. There is another evidence for the DSA hypothesis. Fine serrations in the flow curves were observed indicating occurrence of the interaction between dislocations and the solute, which leads to load drops in a periodic manner. This is called the "Portevin-Le Châtelier effect" [Döner & Conrad, 1973].

Apparently, the DSA behaviour will not occur in the HP-Ti. This is proved by Garde et al. [Garde et al., 1972]. They found with the growth of temperature, the work hardening rate is dropping steadily. Their experiment also shows strain hardening rates of HP-Ti and CP-Ti start to diverge from about 127℃, which is lower than the temperature at which the

peak shows up. Because the conditions for twinning are almost the same in these two types of titanium, the DSA appears to occur at a relatively low temperature.

As to the higher temperature zone above the DSA region (the peak), Döner & Conrad [Döner & Conrad, 1973] thought thermally activated mechanisms, such as creep, dominate there. Inspired by other metals, it is reasonable to believe that there is a diffusion controlled creep mechanism functioning.

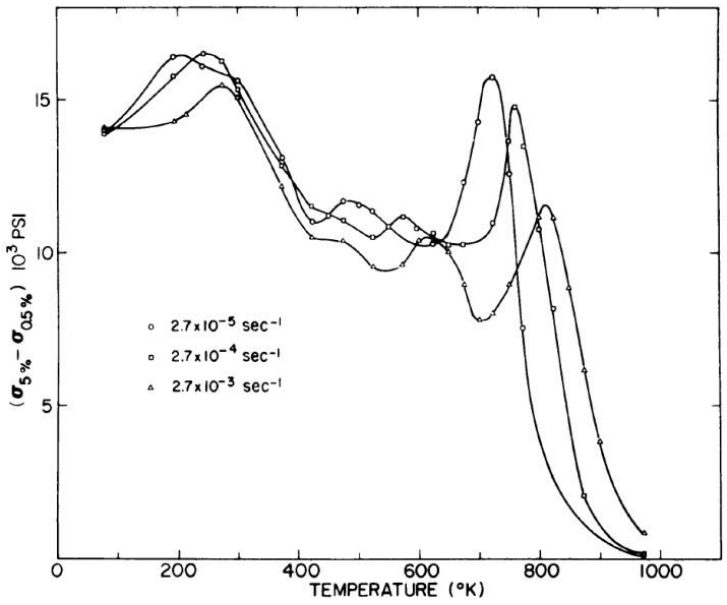

Figure 2.3. The effect of temperature on strain hardening rate in tests with different strain rates [Santhanam & Reed-Hill, 1971].

Usually, the yield strength (σ_y) decreases with the temperature increasing, except a region in the range of 325-500℃ [Döner & Conrad, 1973; Gray, 1997; Huang et al., 2007; Nemat-Nasser et al., 1999; Salem et al., 2003b]. When the strain rate is very high, that region can extend to as low as 125℃ [Nemat-Nasser et al., 1999]. However, there is one

exceptional case reported on the single crystal HP-Ti [Paton & Backofen, 1970]. It is not certain that the result of this experiment can be applicable to the polycrystalline case.

The strain hardening rate of Stage Two usually decreases with the growth of temperature up to about 325℃. After that, the flow stress tends to be constant [Gray, 1997; Huang et al., 2007; Nemat-Nasser et al., 1999; Salem et al., 2003b]. The transition, in which flow stress starts to be constant, moves up to a higher temperature with strain rate increasing [Nemat-Nasser et al., 1999]. Accompanying this change is the decreasing activity of twinning, which makes DSA again probably the underlying mechanism.

In reality, the situation can be very complicated, because the variables never influence the flow curve individually. The pattern of the relation between temperature and flow curve can be inconsistent with different textures considered. But it is still practical to analyse them separately. In this thesis, the author will discuss all the different variables in this way and assemble them together comprehensively when dealing with the individual cases.

2.2.3.2 Effect of Texture and Stress State

As mentioned before, the texture or the orientations of the grains relative to the stress state has a significant effect on the operative mechanisms in deformation process. In other words, the flow curves are strongly anisotropic.

Mullins & Patchett [Mullins & Patchett, 1981] did research on CP-Ti in plane strain, uniaxial and equi-biaxial tension tests. The tests, which applied more strain in the through thickness direction, show higher flow stress, an extended Stage Two and stronger twin activity. Murayama et al. [Murayama et al., 1991] showed similar results in plane strain compression and tension with various textures in CP-Ti sheet. They found that plane

strain compression leads to stronger strain hardening and activity of twinning as well. Also, as the applied stress increases, the strain hardening effect correlates well with textures and more twinning is activated [Murayama et al., 1991; Murayama et al., 1987]. Gray [Gray, 1997] conducted an in-plane and a through-thickness compression on HP-Ti. The in-plane test results show a lower yield stress with a higher strain hardening rate in Stage Two. They also claimed that the strain hardening rate was due to the strong effect of twinning, even though the twin activity was low in the in-plane test.

2.2.3.3 Effect of Strain Rate

Generally, the flow stress increases with the increasing strain rate in both HP-Ti and CP-Ti [Chichili et al., 1998; Gary, 1997; Huang et al., 2007; Nemat-Nasser et al., 1999]. Furthermore, when temperature decreases, the distinction between flow stresses under different strain rates becomes smaller [Gray, 1997; Nemat-Nasser et al., 1999]. As for the effect on strain hardening, Gray [Gray, 1997] found a higher strain hardening rate in the Stage Two of a dynamic test of HP-Ti than the quasi-static test. This is due to the increased activity of twinning and they serve as obstacles on the slip path. Chichili et al. [Chichili et al., 1998] have obtained a similar result. However, they claim that twin activity is just the consequence of a higher stress level, and it is the dislocation accumulation and recovery that cause the strain hardening.

2.2.3.4 Effect of Composition

For single crystal titanium, Naka et al. [Naka et al., 1988] found that the CRSS for P<a> increases with higher impurity and the difference of CRSS decreases at higher temperature. They also proposed a new hypothesis for impurity effect on CRSS for

temperature zone below 227℃. They suggested that the effect of impurity is due to a modification of the dislocation structure, which increases the lattice friction. Farenc et al. [Farenc et al., 1993] found similar rules in the prediction using a locking-unlocking mechanism of P<a>, which showed higher energy for slipping in the titanium with greater impurity.

In polycrystalline tests, Garde et al. [Garde et al., 1973] studied the effect of impurity at -196℃ in tension. It is different from the status in single crystal that the increasing impurity causes the reduction in strain hardening in Stage Two with the twin activity decreasing as well.

2.2.3.5 Effect of Grain Size

The effect of grain size was studied and quantified mostly by Conrad [Conrad, 1981]. The data concurred with the Hall-Petch equation [Armstrong et al., 1961] which is often used in analyzing the grain size effect. The variables in Hall-Petch equation are not independent of other factors influencing the flow curves. For example, in the strain hardening analysis, the rate is found to increase with the increasing grain size at low strains (<0.1). Gray [Gray, 1997] found that in Stage Two the strain hardening rate still obeyed the former rule in the grain size range from 20μm to 240μm. The increased activation of twinning is thought to be the trigger.

2.3 Overview of Deformation Modelling

The complexity of the deformation mechanisms in titanium does not only make the experimental studies difficult, but also the modelling work. One possible way to avoid this problem is to model at the atomic scale, which can more easily reproduce the real

situation inside the material. However, this micro-scale method of modelling requires a large amount of calculation work on computer. Needless to say, the type of atomic model chosen can significantly affect the efficiency of the calculation. Moreover, atomic model remains as a tool to investigate specific mechanism. It is still difficult to simulate the experiments and provide information to the models at coarser scales.

Besides the atomic modelling at micro-scale, more success has been achieved by coarser scale modelling approaches. Using empirical equations, an average value of parameters and a broad description of the essential mechanism can be obtained. In this way, this kind of method is perhaps more efficient in determining the parameters at a coarser scale, like the yielding parameters, than the finer scale methods. Usually, an inverse approach is implemented, in which the modelling results are fitted to gain the experimental results by calibrating the parameters. In this way, reasonable amount of effort is needed to justify the model. As to the model at coarser scales, there is always loss of flexibility to some extent, which may lead to different parameters for different experiments, even if only one variable of the experiment changes. So this is still a much active field in titanium deformation research to promote the flexibility of the models.

In order to provide a quantitative analysis of the anisotropic properties of titanium, the most promising model is that which considers diverse slip and twining modes as well as the interactions between slip and twinning in this material. Such models with texture evolution and strain hardening taken into account are the most favoured. In the following, previous achievements with respect to this type of models will be reviewed.

Generally, the crystal plasticity modelling is the simulation of plastic deformation in crystalline materials based on the microscopic deformation mechanisms at the crystal level [Battaini, 2008]. Slip and twinning are usually the most common deformation mechanisms. They are assumed to obey the Schmid law in most practical cases, although opposing evidence exists against this [Naka et al., 1988; Jones & Hutchinson, 1981; Akhtar, 1975]. There are three significant issues about this type of models that attract most attention. The foremost is the homogenisation scheme adopted to describe the behaviour of polycrystal to the individual constituent grain. The development of this part of model corresponds to the evolution of the whole model. The second issue is the description of hardening mechanisms, which determines the resistance for the activation of deformation modes. At last, the twinning models are applied to numerically reproduce the influence of twinning on the textures of materials. All the development regarding these issues in α-titanium will be reviewed in the following.

2.3.1 Homogenisation Schemes

The earliest homogenisation scheme was proposed as Sachs. It assumes equal stress in all the grains and yielding occurs simultaneously in all the grains [Kocks et al., 1998]. This assumption turns out to be a lower bound of prediction. Also, it assumes only single slip in each of the grains and, consequently, the compatibility between the grains is impossible to achieve [Hosford, 1993; Taylor, 1938-1939]. In contrast, Taylor [Taylor, 1938-1939] suggested a scheme assuming equal strain in each grain of the polycrystal. One of the assumptions of Taylor scheme is that at least five independent components of strain are should be present to accommodate the change in shape with constant volume.

At the beginning, Taylor scheme worked well in the deformation of polycrystalline face-centered cubic (FCC) metals and obtained reasonable results. Bishop & Hill [Bishop & Hill, 1951a; Bishop & Hill, 1951b] presented another way to determine the slip systems activated by the principal of maximum virtual work, which turned out to be an equivalent method of Taylor [Taylor, 1938-1939; Bishop & Hill, 1951b]. With the development of computers, it is feasible to extend the model to multiple slip mode case [Chin & Mammel, 1967] and to lattice rotation [Chin et al., 1967] which is closer to the reality and more practical.

Kocks & Chandra [Kocks & Chandra, 1982] claimed a poor performance of Taylor scheme under the partially constrained conditions, when all components of strain were prescribed. The partially constrained conditions refer to some types of deformation, such as channel die compression (CDC) and deformation of heavily pre-deformed flat grains. The simulation results can be optimised by reducing the numbers of imposed strain components, which is called the relaxed constraints (RC) Taylor scheme. In contrast, the former version of Taylor scheme is called full constraints (FC). Tomé et al. [Tomé et al., 1984] have illustrated the effect of the RC Taylor scheme on the flow curve at macro-scale and large strains. Following this, more work around RC scheme has been done. Recent studies on RC scheme incorporate some local grain interactions and try to improve the prediction of textures in this way [Van Houtte et al., 2006].

The SC schemes were developed as another type of homogenisation schemes [Hill, 1965; Hill, 1967; Hutchinson, 1970]. This kind of schemes can be regarded as the mathematical generalisations of RC scheme [Van Houtte et al., 2004]. The SC schemes regard each

grain as an inclusion, which is embedded in the homogeneous effective medium (HEM) representing the average of surrounding grains. Each grain has been assumed to represent all the same oriented grains. Interaction between the inclusion and the HEM is obtained with the solution of local stress equilibrium equations. The SC scheme cost more computer power than RC scheme. However, the SC scheme has been developed to take into account interaction between two or more grains [Lebensohn & Canova, 1997; Lebensohn et al., 1997; Canova, 1994; Solas & Tomé, 2001] and, consequently, the results of multi-phase materials can be promoted. It needs to be noted that SC schemes consist of many subtypes with different mathematical assumptions, such as "affine", "secant", "tangent" and "neff=10". SC schemes will be discussed with more details in Section 1.4.2.5.

The models mentioned above only perform well in simple deformation conditions, like uniaxial compression or tension. More complex deformation using the crystal plasticity model should incorporate it in the finite element analysis (FEA) program. Many studies have been done in this way using Taylor scheme [Beaudoin et al., 1994; Kalidindi et al., 1992; Marin & Dawson, 1998] and SC schemes [Tomé et al., 2001].

2.3.2 Hardening and Saturation Law

The hardening or saturation law is developed to describe the evolution of slip and twinning activities or resistance to their activation during deformation. Without this law, simulation may result in a twinning volume fraction of 100%, which is obviously unrealistic.

Myagchilov & Dawson [Myagchilov & Dawson, 1999] proposed a mechanistic model for the saturation of twinning based on their observation showing that twins hardly intersect other existing twins. However, the activity of twinning becomes very high at the beginning of deformation and saturates quickly, which is against the reality. It is not certain to attribute the problem to Taylor scheme or choosing the low relative resolved shear stress (RRSS) value of twinning. Needless to say, these flaws cannot undermine the significance of this promising idea.

More extensive saturation law for slip and twinning is presented in Salem et al. [Salem et al., 2005] and Wu et al. [Wu et al., 2007]. The original model comes from Kalidindi [Kalidindi, 2001]. This twinning model is incorporated in the Taylor scheme and was developed by adding an extra term to an original slip CRSS evolution equation. The original slip CRSS equation is a saturation law itself with the added term expressing the interaction between slips and twins. The final expression of this hardening model is:

$$\dot{s}^{\alpha} = h_s^{\alpha}(1 - \frac{s^{\alpha}}{s_s^{\alpha}}) \sum_k^{N^s} \dot{\gamma}^k \quad (1.3.1\text{-}1)$$

$$h_s^{\alpha} = h_{so}(1 + C(\sum_{\beta} f^{\beta})^b) \quad (1.3.1\text{-}2)$$

$$s_s^{\alpha} = s_{so} + s_{pr}(\sum_{\beta} f^{\beta})^{0.5} \quad (1.3.1\text{-}3)$$

In these equations, s^{α} is the CRSS value of one particular slip system α, s_s^{α} is the CRSS saturation value and s_{so} is the initial saturation value without twinning; h_s^{α} and h_{so} represent the hardening rate and initial hardening rate of one slip mode; the summation term with N^s is over all slip systems of one slip mode. The $\sum_{\beta} f^{\beta}$ term represents the summation of twin volume fraction for β twin systems. C, b and s_{pr} are all hardening

parameters that need to be fitted by the experimental results. For more accurate modelling, different h_{so} and s_{so} should be assigned to different slip systems and the final result should be the sum of all terms corresponding to different slip modes. For more details of this model, the readers should refer to the work of Wu et al. [Wu et al., 2007]. Equation (1.3.1-2) gives the hardening effect due to Basinski mechanism with an assumption that Basinski hardening can be applied to the whole region of grains instead of the twinned regions only. Equation (1.3.1-1) shows a similar form of Hall-Petch hardening law. However, it would be better if the model could be linked to the physical parameters *k* and *d* in the original form of Hall-Petch equation. This has been done in the composite grain (CG) model by Proust et al. [Proust et al., 2007]. There is another thing that needs to be noted that the twin hardening is applied in Salem et al. [Salem et al., 2005], but in the later work [Wu et al., 2007], no hardening law for twinning is adopted and the evolution of twinning is described in a different way.

Besides the saturation law, there are also Voce hardening law (see Section 1.4.3) and Mechanical Threshold Stress (MTS) type hardening that have been implemented in programs to realize the similar function. More details about these laws will not be discussed in this section and can be referred to easily in related literature.

2.3.3 Twinning Model

Twinning model is used to account for the formation of twins, which needs to be designed in a manner considering computational efficiency. This thesis will introduce in this section several popular twinning models which are usually adopted by researchers.

The first is the predominant twin reorientation (PTR) model [Tomé et al., 1991] and its further enhancement by Van Houtte [Van Houtte, 1978]. In this model, the grains are chosen by a criterion for reorientation. During deformation process, the volume fractions of all twinning systems in each grain are tracked. When an accumulated volume fraction of a twin system exceeds a threshold value which is obtained by an empirical equation, that corresponding grain will be fully reoriented. That twin system with an exceeding volume fraction is called the predominant twin system (PTS) and determines the reorientation of the grain. The threshold value will be updated after each reorientation at each step. This model performs very well, when one twin system prevails in the grains. However, similar activities of different twinning systems may lead to unrealistic results by this model. Since the author will apply this model in the simulation work of this thesis, more details of this model will be presented in Section 1.4.4.

The second is the volume fraction transfer (VFT) scheme, which is developed to avoid this disadvantage. This scheme describes the initial texture using volume fractions in a regular grid of orientations in Euler space and the change of volume fractions is used to represent the reorientation process. In this way, the real quantitative status of twinning can be modelled explicitly. However, the history of deformation will be lost. The two twinning schemes above are mainly employed in the simulation work of zirconium which is quite similar to titanium for some properties.

Kalidindi [Kalidindi, 1998] proposed a new kind of interpretation of the multiplicative decomposition of the deformation gradient to its elastic and plastic components, basing on a total Lagrangian crystal plasticity model which was initially developed for materials

with slip mechanisms only. This method allows crystal plasticity theory with deformation twinning to be applied to a single crystal and takes full advantage of the fully implicit time integration schemes. However, this method still cannot easily deal with the slip inside the twinned areas, which has been confirmed to have a significant role in the plastic deformation.

Subsequently, a more extensive model based on the former one [Kalidindi, 1998] has been proposed [Wu et al., 2007]. In this model, hardening of twinning is not considered at all and the CRSS is regarded as constant. But the twin saturation has been enforced and as soon as the twin volume fraction reaches a critical value, that part of grain is separated from the matrix as a new grain. After the fragmentation, slip remains as the only mechanism in the new grain without twinning. This is reasonable because secondary twinning makes little contribution to the strain, which has been confirmed by experiments. However, the possible grain refinement and DHP hardening resulting from the twinning are neglected after the fragmentation.

A new constitutive twinning model has been developed by Wu and co-workers in recent years [Wang et al., 2012]. This twinning-detwinning (TDT) model is able to capture the key features related to twinning and detwinning behaviour observed in experiments. The growth of twinning and detwinning processes of twin system "α" are represented by four "operations" (A, B, C, D) in the model. The twin volume fractions of "α" due to each of the operations are tracked and used to obtain the total twin volume fraction of "α". A threshold value for termination of reorientation by twinning is defined with accumulated twin fraction and effective twinned fraction (volume fraction of twin terminated grains).

After the comparison between total twin volume fraction and threshold value, a decision with regard to reorientation of the twinned area can be made. It is worth noting that no additional parameter for detwinning is introduced in this model. Moreover, TDT model gives out more accurate simulated result during strain path changes tests than the CG model which is also a twinning model aimed at both twinning and detwinning behaviours. The readers are referred to Proust et al. [Proust et al., 2007; Proust et al., 2009] for more details about CG model.

2.3.4 Crystal Plasticity Modelling of Titanium

In the earlier times, prior to any computer simulations, Calnan and Clews method was proposed to analyze texture [Calnan & Clews, 1951]. The cold rolling texture of titanium could be qualitatively predicted [Williams, 1952-1953b]. The attempts to predict titanium properties using crystal plasticity modelling have been made in recent years. Cheneau-Späth & Driver [Cheneau-Späth & Driver, 1994] developed a limited model for single crystal or bi-crystal using Taylor scheme. Their result revealed a significant issue that the difference between RRSS values of single crystals and polycrystal can be quite large.

There are more extensive modelling works carried out by one research group [Fundenberger et al., 1997; Philippe et al., 1998; Philippe et al., 1995]. They used two types of Taylor schemes with the RRSS values from TEM and optical microscopy (OM) observations. Their hardening model was developed in an ad-hoc manner, which modifies the RRSS values at each stage of the deformation. As to the twinning model, they employed the Monte Carlo (MC) method and modelled the twinning behaviour based on Van Houtte model [Van Houtte, 1978]. One apparent disadvantage of MC method is

similar to that of VFT twinning scheme, which is the loss of deformation history. Moreover, the MC method requires large amount of initial grains to make the result accurate. The results of these modelling works using MC method turned out to match the experimental data well. The most significant feature of one study [Fundenberger et al., 1997] is that different RRSS values are used for the positive and negative sense of <c+a> slip. The asymmetry of Π_1<c+a> slip has been investigated and reported in Ti-6Al-4V [Jones & Hutchinson, 1981; Medina Perilla & Gil Sevillano, 1995] but not in α-titanium.

Myagchilov & Dawson [Myagchilov & Dawson, 1999] tried to use their model to capture the saturation of twinning. However, the predictions of texture from their model were rather poor and additional work by a number of authors has led to a better prediction [Kalidindi, 2001; Salem et al., 2005; Wu et al., 2007]. As to the remaining difference between the modelling and the experimental results, the above researchers have attributed this to the use of Taylor type scheme.

Balasubramanian & Anand [Balasubramanian & Anand, 2002] carried out the crystal plasticity modelling for titanium at 750℃. They simplified the latent hardening into coplanar or non-coplanar interactions, which have one parameter determining the strength with each of them. As a result, the interactions of these two types of dislocations have the same effect. As for the self-hardening behaviour, it is simulated by a saturation law. The result of this model turned out to give a good fit to the experimental results.

2.4 Visco-Plastic Self-Consistent (VPSC) Model

The outline of deformation modelling in the field of titanium research has been shown in the former sections. The numerical model used in the present work is the VPSC model of

Proust et al. [Proust et al., 2007]. The code is referred to as "VPSC7a" in the thesis. It is necessary for the author of this thesis to describe the main parts of this model in this section, and especially the constitutive equations and SC schemes. Although the equations are available in the literature, it would be useful to describe them here as they constitute the core of simulation work in this thesis. It needs to be noted that the VPSC model is focused on the plastic deformation of materials, since the elastic deformation is negligible when compared with plastic deformation up to large strains. The author's research group has carried out a study about the self-consistent model with elastic deformation taken into account. More details of this model named "elastic-viscoplastic self-consistent (EVPSC)" can be found in Wang et al. [Wang et al., 2010b].

2.4.1 Kinematics

X is defined as the initial coordinates of a point in the undeformed crystal, $x(X)$ as the final coordinates of a point in the deformed crystal and $u = x - X$ as the displacement of the point. Assuming the deformation in grains is characterized by L^c which is the displacement gradient tensor and F^c which is the deformation gradient tensor. They are defined as:

$$L_{ij}^c = \frac{\partial \dot{u}_i^c}{\partial x_j} \tag{1.4.1-1}$$

$$F_{ij}^c = \frac{\partial x_i}{\partial X_j} \tag{1.4.1-2}$$

They have a relationship as:

$$\dot{F}^c = L^c F^c \tag{1.4.1-3}$$

$$x = \mathrm{F}^c X \tag{1.4.1-4}$$

Moreover, plastic deformation is accommodated by shear and it maintains the orientation of the crystal, so deformation gradient can be decomposed into a "plastic stretch" F_o^c and a rigid crystal rotation R^c.

$$F^c = R^c F_o^c \tag{1.4.1-5}$$

Also, the plastic stretch obeys the same rule:

$$\dot{F}_o^c = L_o^c F_o^c \tag{1.4.1-6}$$

$$L_{oij}^c = \frac{\partial \dot{u}_i^c}{\partial X_j} \tag{1.4.1-7}$$

This equation describes the velocity gradient in the initial crystal axes. It can be given in the form of linear superposition of shear rates on all the active slip and twinning systems:

$$L_{oij}^c = \sum_s \dot{\gamma}^s b_i^s n_j^s \tag{1.4.1-8}$$

The Schmid tensor $b^s \otimes n^s$ can be decomposed into a symmetric and a skew symmetric components, in which b^s and n^s are the Burgers and normal vector of slip or twinning system "s":

$$\mathrm{m}_{ij}^s = \frac{1}{2}(b_i^s n_j^s + b_j^s n_i^s) \tag{1.4.1-9a}$$

$$q_{ij}^s = \frac{1}{2}(b_i^s n_j^s - b_j^s n_i^s) \tag{1.4.1-9b}$$

This allows one to do decomposition to the velocity gradient and turn it into a strain rate and a rotation rate (spin):

$$L_{oij}^c = D_{oij}^c + W_{oij}^c \tag{1.4.1-10}$$

$$D^c_{o\,ij} = \sum_s \dot{\gamma}^s m^s_{ij} \text{ and } W^c_{o\,ij} = \sum_s \dot{\gamma}^s q^s_{ij} \tag{1.4.1-11}$$

Then decomposition of the general velocity gradient is given by:

$$L^c_{ij} = D^c_{ij} + W^c_{ij} \tag{1.4.1-12}$$

$$\begin{cases} D^c = R^c D^c_o (R^c)^T \\ W^c = R^c W^c_o (R^c)^T + \dot{R}^c (R^c)^T \end{cases} \tag{1.4.1-13}$$

It can be seen that distortion rate D^c is just a transformation from crystal axes to sample axes, while the rotation rate has an extra term.

2.4.2 Self-Consistent Polycrystal Formalism

In this section, basic equations of the 1-site VPSC model are presented. The derivation here is completely general and the comprehensive derivations can be found in references [Lebensohn et al., 2004; Tomé& Lebensohn, 2004].

In brief, polycrystal is represented here by a certain number of weighted orientations which can be input through a separate file. The orientations of the grains stand for themselves and weights for their volume fractions. The latter set of data can be used to reproduce texture profile. Every grain is regarded as an ellipsoidal visco-plastic inclusion which is embedded in an effective visco-plastic medium. Deformation is achieved through crystal plasticity mechanisms, such as slip and twinning systems which are activated by resolved shear stress (RSS).

2.4.2.1 Local Constitutive Behavior and homogenization

The visco-plastic constitutive behavior at local level can be described by a non-linear rate sensitivity equation.

$$\dot{\varepsilon}_{ij}(\bar{x}) = \sum_s m_{ij}^s \dot{\gamma}^s(\bar{x}) == \dot{\gamma}_o \sum_s m_{ij}^s \left(\frac{m_{kl}^s \sigma_{kl}(\bar{x})}{\tau_o^s} \right)^n \tag{1.4.2-1}$$

In this equation, τ^s is the threshold stress or critical resolved shear stress, $\sigma_{kl}(\bar{x})$ and $\dot{\varepsilon}_{ij}(\bar{x})$ are the deviatoric stress and strain-rate, and $\dot{\gamma}^s(\bar{x})$ is the local shear strain-rate on slip or twinning system "s". In the expression for $\dot{\gamma}^s(\bar{x})$, $\dot{\gamma}_o$ is a normalization factor and "n" is the rate sensitivity.

The equation for $\dot{\varepsilon}_{ij}(\bar{x})$ can be linearized inside the domain of one grain "r":

$$\dot{\varepsilon}_{ij}(\bar{x}) = M_{ijkl}^{(r)} \sigma_{kl}(\bar{x}) + \dot{\varepsilon}_{ij}^{o(r)} \tag{1.4.2-2}$$

$M_{ijkl}^{(r)}$ and $\dot{\varepsilon}_{ij}^{o(r)}$ are the visco-plastic compliance and back-extrapolated term of grain "r". The same relation exists for the average stress and strain-rate in this grain.

$$\dot{\varepsilon}_{ij}^{(r)} = M_{ijkl}^{(r)} \sigma_{kl}^{(r)} + \dot{\varepsilon}_{ij}^{o(r)} \tag{1.4.2-3}$$

According to different linearization assumptions, $M_{ijkl}^{(r)}$ and $\dot{\varepsilon}_{ij}^{o(r)}$ can be chosen variously. This will be discussed in the section about SC schemes. Then the homogenization can be done on the linearized heterogeneous medium by assuming that it has a similar relation:

$$\dot{E}_{ij} = \overline{M}_{ijkl} \Sigma_{kl} + \dot{E}_{ij}^o \tag{1.4.2-4}$$

In this equation, $\dot{E}_{ij}$ and Σ_{kl} are macroscopic magnitudes of strain-rate and stress. $\overline{M}_{ijkl}$ and $\dot{E}_{ij}^o$ are the macroscopic visco-plastic compliance and back-extrapolated term, respectively. Then $\dot{\varepsilon}_{ij}(\bar{x})$ can be rewritten:

$$\dot{\varepsilon}_{ij}(\bar{x}) = \overline{M}_{ijkl} \sigma_{kl}(\bar{x}) + \dot{E}_{ij}^o + \varepsilon_{ij}^*(\bar{x}) \tag{1.4.2-5}$$

$\varepsilon_{ij}^{*}(\bar{x})$ is the eigen-strain-rate field. It follows from replacing the inhomogeneity by an equivalent inclusion. After some tensor algebraic manipulation, the following equation can be obtained:

$$\tilde{\sigma}_{ij}(\bar{x}) = \bar{L}_{ijkl}\left(\tilde{\dot{\varepsilon}}_{kl}(\bar{x}) - \dot{\varepsilon}_{kl}^{*}(\bar{x})\right) \tag{1.4.2-6}$$

The symbol "~" in the expression indicates local deviation of the corresponding tensor from macroscopic values. Also, $\bar{L}_{ijkl} = \bar{M}_{ijkl}^{-1}$. Combining this equation with equilibrium condition:

$$\sigma_{ij,j}^{c}(\bar{x}) = \tilde{\sigma}_{ij,j}^{c}(\bar{x}) = \tilde{\sigma}_{ij,j}(\bar{x}) + \tilde{\sigma}_{,i}^{m}(\bar{x}) \tag{1.4.2-7}$$

σ^{c} and σ^{m} are the Cauchy and mean stresses. With incompressibility condition and the relation between strain-rate and velocity gradient $\tilde{\varepsilon}_{ij}(\bar{x}) = \frac{1}{2}\left(\tilde{u}_{i,j}(\bar{x}) + \tilde{u}_{j,i}(\bar{x})\right)$, these equations can be obtained:

$$\begin{cases} \bar{L}_{ijkl}\tilde{u}_{k,lj}(\bar{x}) + \tilde{\sigma}_{,i}^{m}(\bar{x}) + f_i(\bar{x}) = 0 \\ \tilde{u}_{k,k}(\bar{x}) = 0 \end{cases} \tag{1.4.2-8}$$

In these equations,

$$f_i(\bar{x}) = -\bar{L}_{ijkl}\varepsilon_{kl,j}^{*}(\bar{x}) = \sigma_{ij,j}^{*}(\bar{x}) \tag{1.4.2-9}$$

The equation set above can be solved using Green function method along with Fourier transform method. After some rearrangement and derivation, the following expressions can be obtained:

$$\tilde{\varepsilon}_{ij}^{(r)} = S_{ijkl}\varepsilon_{kl}^{*(r)} \tag{1.4.2-10}$$

$$\tilde{\omega}_{ij}^{(r)} = \Pi_{ijkl}\varepsilon_{kl}^{*(r)} = \Pi_{ijkl}S_{klmn}^{-1}\tilde{\varepsilon}_{mn}^{(r)} \tag{1.4.2-11}$$

In these expressions, S_{ijkl} and Π_{ijkl} are the symmetric and skew symmetric Eshelby tensors.

2.4.2.2 Interaction and Localization Equations

With the equation presented in the previous sub-section,

$$\tilde{\sigma}_{ij}(\bar{x}) = \bar{L}_{ijkl}\left(\tilde{\tilde{\varepsilon}}_{kl}(\bar{x}) - \dot{\varepsilon}^{*}_{kl}(\bar{x})\right) \tag{1.4.2-12}$$

This expression can be rewritten into interaction equation as:

$$\tilde{\tilde{\varepsilon}}^{(r)}_{ij} = -\tilde{M}_{ijkl}\tilde{\sigma}^{(r)}_{kl} \tag{1.4.2-13}$$

The interaction tensor is given by

$$\tilde{M}_{ijkl} = (I - S)^{-1}_{ijmn} S_{mnpq} \overline{M}_{pqkl} \tag{1.4.2-14}$$

Replacing the local and general deviatoric constitutive relations into the interaction equation and after carrying out some further manipulation. This equation can be obtained:

$$\sigma^{(r)}_{ij} = B^{(r)}_{ijkl}\Sigma_{kl} + b^{(r)}_{ij} \tag{1.4.2-15}$$

where the localization tensors are:

$$B^{(r)}_{ijkl} = \left(M^{(r)} + \tilde{M}\right)^{-1}_{ijmn}\left(\overline{M} + \tilde{M}\right)_{mnkl} \tag{1.4.2-16}$$

$$b^{(r)}_{ij} = \left(M^{(r)} + \tilde{M}\right)^{-1}_{ijkl}\left(\dot{E}^{o}_{kl} - \dot{\varepsilon}^{o(r)}_{kl}\right) \tag{1.4.2-17}$$

2.4.2.3 Self-Consistent Equations

In this section, the author will present the derivation around the iteration to find the properties of the effective medium. Results from previous sections will be applied to construct the whole polycrystal model.

After rewriting the former equation by replacing Equation (1.4.2-16) and (1.4.2-17), this equation can be obtained:

$$\dot{\varepsilon}_{ij}^{(r)} = M_{ijkl}^{(r)}\sigma_{kl}^{(r)} + \dot{\varepsilon}_{ij}^{o(r)} = M_{ijkl}^{(r)}B_{klmn}^{(r)}\Sigma_{mn} + M_{ijkl}^{(r)}b_{kl}^{(r)} + \dot{\varepsilon}_{ij}^{o(r)} \tag{1.4.2-18}$$

The condition has to be enforced that weighted average strain-rate should be equal to the macroscopic quantity:

$$\dot{E}_{ij} = \left\langle \dot{\varepsilon}_{ij}^{(r)} \right\rangle \tag{1.4.2-19}$$

The arrow bracket "<>" denotes the calculation over all the grains to get the average value with weight factor considered. Similarly, about the macroscopic constitutive equations:

$$\overline{M}_{ijmn}\Sigma_{mn} + \dot{E}_{ij}^{o} = \left\langle M_{ijkl}^{(r)}B_{klmn}^{(r)} \right\rangle \Sigma_{mn} + \left\langle M_{ijkl}^{(r)}b_{kl}^{(r)} + \dot{\varepsilon}_{ij}^{o(r)} \right\rangle \tag{1.4.2-20}$$

So it is easy to have these equations:

$$\overline{M}_{ijkl} = \left\langle M^{(r)} : B^{(r)} \right\rangle \tag{1.4.2-21a}$$

$$\dot{E}_{ij}^{o} = \left\langle M^{(r)} : b^{(r)} + \dot{\varepsilon}^{o(r)} \right\rangle \tag{1.4.2-21b}$$

If each of the grains has a different shape and has associated different Eshelby tensors, the interaction tensors cannot be factored from the average. Also, the general expressions of SC procedure should be applied [Lebensohn et al., 2004; Walpole, 1969; Lebensohn et al., 1996; Lebensohn et al., 2003]:

$$\overline{M}_{ijkl} = \left\langle M^{(r)} : B^{(r)} \right\rangle : \left\langle B^{(r)} \right\rangle^{-1} \tag{1.4.2-22a}$$

$$\dot{E}_{ij}^{o} = \left\langle M^{(r)} : b^{(r)} + \dot{\varepsilon}^{o(r)} \right\rangle - \left\langle M^{(r)} : B^{(r)} \right\rangle : \left\langle B^{(r)} \right\rangle^{-1} : \left\langle b^{(r)} \right\rangle \tag{1.4.2-22b}$$

2.4.2.4 Algorithm

To explain the implementation of this formulation, the author here presents the steps to predict the local and overall visco-plastic response.

For an applied macroscopic velocity gradient $U_{i,j} = \dot{E}_{ij} + W_{ij}$, $\dot{E}_{ij}$ and W_{ij} are the symmetric strain-rate and skew-symmetric rotation-rate. To start iteration for searching the local states, the initial values for local deviatoric stress and moduli should be assumed. The program takes Taylor guess for initial state: $\dot{\varepsilon}_{ij}^{(r)} = \dot{E}_{ij}$ for all grains. Then the program solves the non-linear equation (1.4.2-1) and a linearization scheme (see next section) to obtain the initial values of $\sigma_{ij}^{(r)}$, $M_{ijkl}^{(r)}$ and $\dot{\varepsilon}_{ij}^{o(r)}$ with equation (1.4.2-3). Next, initial guess for macroscopic moduli $\overline{M}_{ijkl}$ and $\dot{E}_{ij}^{o}$ can be calculated. After that, the applied strain-rate $\dot{E}_{ij}$, and the initial guess for macroscopic stress are obtained by the inversion of the macroscopic constitutive law (1.4.2-4). Meanwhile, the value of Eshelby tensors S_{ijkl} and Π_{ijkl} can be accessed using the macroscopic moduli and the grain shape. Next, the interaction tensor $\tilde{M}_{ijkl}$ (1.4.2-14), as well as the localization tensors $B_{ijkl}^{(r)}$ and $b_{ij}^{(r)}$ (1.4.2-16, 1.4.2-17), can be obtained. With the above tensors at hand, estimates of $\overline{M}_{ijkl}$ and $\dot{E}_{ij}^{o}$ is obtained by solving the SC equations (1.4.2-21 or 1.4.2-22) iteratively. Subsequently, once the convergence is achieved on the macroscopic moduli, new estimate of grain stress can be obtained by combining the local constitutive equation and interaction equation together as:

$$\dot{\gamma}_o \sum_s m_{ij}^s \left(\frac{m_{pq}^s \sigma_{pq}^{(r)}}{\tau^s} \right)^n - E_{ij} = -\tilde{M}_{ijkl} \left(\sigma_{kl}^{(r)} - \Sigma_{kl} \right) \quad (1.4.2\text{-}23)$$

Solving this equation set will lead to five independent components of the deviatoric stress tensor of the grain $\sigma_{kl}^{(r)}$. However, if the new local stresses are different from the input values, new iteration should be carried out. Otherwise, the iterative calculation is done and the shear rates on slip or twinning for each system "s" in grain "r" can be obtained as:

$$\dot{\gamma}^{s(r)} = \dot{\gamma}_o \left(\frac{m_{pq}^s \sigma_{pq}^{(r)}}{\tau_o^s} \right)^n \quad (1.4.2\text{-}24)$$

Subsequently, the rotation rates and the lattice associated with each grain follow as:

$$\omega_{ij}^{inc(r)} = W_{ij} + \tilde{\omega}_{ij}^{(r)} \quad (1.4.2\text{-}25)$$

$$\omega_{ij}^{lat(r)} = W_{ij} + \tilde{\omega}_{ij}^{(r)} - W_{oij}^{(r)} \quad (1.4.2\text{-}26)$$

$$W_{oij}^{(r)} = \sum_s q_{ij}^s \gamma^{s(r)} \text{ and } q_{ij}^s = \frac{1}{2}(b_i^s n_j^s - b_j^s n_i^s) \quad (1.4.2\text{-}27 \text{ and } 28)$$

2.4.2.5 Self-Consistent Schemes

As mentioned earlier, for the linearization behavior, different choices are available. There are several SC linearization schemes implemented in VPSC:

1) Secant [Hutchinson, 1976]

$$M_{ijkl}^{(r),\text{sec}} = \dot{\gamma}_o \sum_s \frac{m_{ij}^s m_{kl}^s}{\tau_o^s} \left(\frac{m_{pq}^s \sigma_{pq}^{(r)}}{\tau_o^s} \right)^{n-1} \quad (1.4.2\text{-}29)$$

$$\varepsilon_{ij}^{o(r),\text{sec}} = 0 \quad (1.4.2\text{-}30)$$

2) Affine [Lebensohn et al., 2003; Masson et al., 2000; Lebensohn et al., 2004]

$$M_{ijkl}^{(r),aff} = n\dot{\gamma}_o \sum_s \frac{m_{ij}^s m_{kl}^s}{\tau_o^s} \left(\frac{m_{pq}^s \sigma_{pq}^{(r)}}{\tau_o^s} \right)^{n-1} \tag{1.4.2-31}$$

$$\varepsilon_{ij}^{o(r),aff} = \left(M_{ijkl}^{(r),\sec} - M_{ijkl}^{(r),aff} \right) \sigma_{kl}^{(r)} = (1-n)\varepsilon^{(r)} \tag{1.4.2-32}$$

3) Tangent [Lebensohn & Tomé, 1993]

$$M_{ijkl}^{(r),tg} = n\dot{\gamma}_o \sum_s \frac{m_{ij}^s m_{kl}^s}{\tau_o^s} \left(\frac{m_{pq}^s \sigma_{pq}^{(r)}}{\tau_o^s} \right)^{n-1} \tag{1.4.2-33}$$

$$\varepsilon_{ij}^{o(r),tg} = 0 \tag{1.4.2-34}$$

4) n^{eff} ($1<n^{eff}<n$)

$$M_{ijkl}^{(r),neff} = n^{eff}\dot{\gamma}_o \sum_s \frac{m_{ij}^s m_{kl}^s}{\tau_o^s} \left(\frac{m_{pq}^s \sigma_{pq}^{(r)}}{\tau_o^s} \right)^{n-1} \tag{1.4.2-35}$$

$$\varepsilon_{ij}^{o(r),neff} = 0 \tag{1.4.2-36}$$

From the equations above, it can be deduced that the smaller the compliance, the smaller is the local deviation of the strain-rate with respect to the average. Consequently, for $n \to \infty$, tangent approximation tends to a uniform stress state, like the Sachs or lower bound approximation. On the contrary, secant interaction is stiff and tends to a uniform strain-rate state, such as in the Taylor or upper bound approximation. For affine and n^{eff} scheme, they remain between those bounds for $n \to \infty$. All of the above schemes are first-order approximations, in which the linearized moduli assigned to grains depend only on the average stress $\sigma_{ij}^{(r)}$. VPSC7 code allows using the more sophisticated second-order moments, but this researcher applied SC schemes in the simulation instead.

2.4.3 Hardening of Slip and Twinning Systems

In the equation mentioned earlier in this chapter:

$$\dot{\varepsilon}_{ij}(\bar{x}) = \sum_s m_{ij}^s \dot{\gamma}^s(\bar{x}) == \dot{\gamma}_o \sum_s m_{ij}^s \left(\frac{m_{kl}^s \sigma_{kl}(\bar{x})}{\tau_o^s} \right)^n \tag{1.4.3-1}$$

there is a threshold value τ_o^s describing the resistance for activation of deformation modes and it usually increases with deformation. This is used to simulate the hardening process in the material and in this section, an extended Voce hardening law [Tomé et al., 1984] will be presented, which is adopted in the present work.

In Voce hardening law, threshold value of resistance is related to accumulated shear strain in each grain with several other parameters.

$$\hat{\tau}^s = \tau_0^s + \left(\tau_1^s + \theta_1^s\right)\left(1 - \exp\left(-\Gamma \left| \frac{\theta_0^s}{\tau_1^s} \right| \right)\right) \tag{1.4.3-2}$$

where $\Gamma = \sum_s \Delta\gamma^s$ is the accumulated shear strain in the grain. τ_0^s, τ_1^s, θ_0^s, θ_1^s are the initial CRSS, the back-extrapolated CRSS, the initial hardening rate and the asymptotic hardening rate. Moreover, the possibility of "self" and "latent" hardening are considered in the hardening process. A coupling coefficient $h^{ss'}$ is introduced which empirically accounts for the mutual impeding of each two deformation mode. In this case, the increase in the threshold stress of a system due to shear $\Delta\gamma^{s'}$ is:

$$\Delta\tau^s = \frac{d\hat{\tau}^s}{d\Gamma} \sum_{s'} h^{ss'} \Delta\gamma^{s'} \tag{1.4.3-3}$$

where $\frac{d\hat{\tau}^s}{d\Gamma} = \left[\theta_1 + \left(\left|\frac{\theta_0}{\tau_1}\right|\tau_1 - \theta_1\right)\exp\left(-\Gamma\left|\frac{\theta_0}{\tau_1}\right|\right) + \left|\frac{\theta_0}{\tau_1}\right|\theta_1\Gamma\exp\left(-\Gamma\left|\frac{\theta_0}{\tau_1}\right|\right)\right]$ (1.4.3-4)

2.4.4 Twinning Model

In the VPSC code, it is assumed that the twinning has been associated with a CRSS for the activation in twinning plane and along the twinning direction like the slip. However, it differs from slip for its unidirectional feature.

Another aspect of twinning that needs to be accounted for is the fact that twinned regions have different orientation from the matrix or parent grains. These twinned regions make contribution to the texture evolution as well as the obstacles for activating other slip and twinning systems. The latter problem is dealt with by the enforced high values of the latent hardening coefficients $h^{ss'}$ describing the mutual interactions between each two deformation modes.

As for the problem of orientation evolution, the PTR model is used [Tomé et al., 1991], which has been mentioned earlier in Section 1.3.1.2. In this model, the program keeps track of the shear strain $\gamma^{t,g}$ contributed by each twinning system "t", in each grain "g". The program also keeps records of the associated volume fraction $V^{t,g} = \frac{\gamma^{t,g}}{S^t}$ (S^t is the characteristic twin shear). The sum over all twin systems of one given twin mode, and over all grains is the "accumulated twin fraction" $V^{acc,\text{mode}}$.

$$V^{acc,\text{mode}} = \sum_g \sum_t \frac{\gamma^{t,g}}{S^t} \quad (1.4.4\text{-}1)$$

Next, the problem of the reorientation of the twinned area has to be solved. However, it is not numerically feasible to take each twinned fraction as a new orientation. So PTR scheme applies a statistical approach. During each incremental step, the program entirely reorients some grains provided certain conditions are fulfilled. The PTR model introduces an "effective twinned fraction" $V^{eff,\text{mode}}$ as the volume associated with the fully reoriented grains for that mode. Also, this model defines a threshold volume fraction:

$$V^{th,\text{mode}} = A^{th1} + A^{th2} \frac{V^{eff,\text{mode}}}{V^{acc,\text{mode}}} \tag{1.4.4-2}$$

After each deformation increment or step, the program randomly picks a grain and identify the twin system with the highest accumulated volume fraction. If it is larger than $V^{th,\text{mode}}$, then the grain is reoriented with $V^{th,\text{mode}}$ and $V^{eff,\text{mode}}$ updated. This process is repeated until all grains are checked or until the effective twin volume exceeds the accumulated twin volume. If the repeating process comes to an end, the program continues to the next deformation step.

Chapter 3 Simulation of Mechanical Behaviours of HP-Ti

3.1 Introduction

HP-Ti has drawn far less attention in the academic community than the CP-Ti. This material has limited application due to its much lower yield stress. However, from a theoretical perspective, it still occupies an important place in the family of titanium alloys. Up until recently, only a few researchers had conducted systematic mechanical tests to identify the deformation mechanisms in HP-Ti or carried out simulation of these experiments [Salem et al., 2003a; Nixon et al., 2010; Bouvier et al., 2012]. In these works, HP-Ti samples with two different types of textures have undergone uniaxial loading, simple shear and plane strain loading tests. These mechanical loading tests have been simulated by the corresponding research groups with different numerical models, including VPSC model. However, there are evident flaws that can be improved in their simulation.

In this chapter, firstly, a comprehensive research by Salem et al. [Salem et al., 2003a] on HP-Ti consisting of mechanical loading tests and simulation will be reviewed. Then a detailed VPSC simulation based on their experiments is presented. The author will show the comparison between the present simulated results and those of Salem et al. to prove the superiority of SC schemes to Taylor scheme which was adopted in the simulation of Salem et al. Additionally in this chapter, the author will discuss the deformation mechanisms of HP-Ti and their contribution in the experiments of Salem et al.

3.2 Experimental Conditions

This experimental data presented in this section was obtained by Salem et al. [Salem et al., 2003a].

3.2.1 Material

Material in this series of experiment was an α-phase HP-Ti (99.9998%), which was supplied by Alta Group of Johnson Matthey Electronics, Inc., Spokane, WA. The chemical composition of this material is shown in Table 3.1. The raw material was received as a clock-rolled disk with 352 mm diameter and 12 mm thickness. The as-received disk was recrystallized at 800℃ for 1 hour. Then it was water quenched, producing an equiaxed grain structure, whose average grain size was 30 μm. The initial texture is shown in Figure 3.1. It is a typical c-type texture, which means the c-axes of many grains were located 20-35 °to the normal direction of the plate.

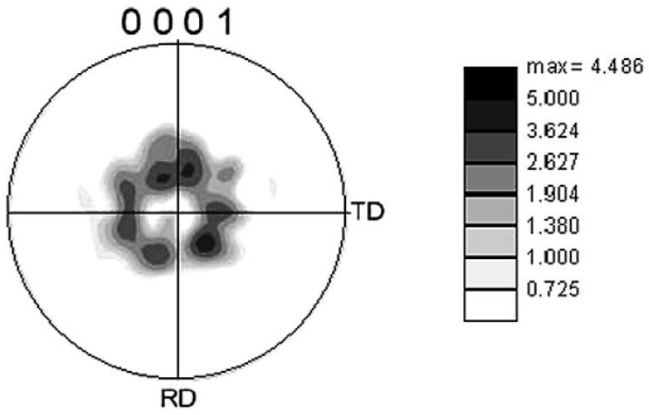

Figure 3.1. The Measured {0001} pole figure of HP-Ti in Salem et al. [Salem et al., 2003a]. Rolling direction (RD) and transverse direction (TD) locate in the plane, while normal direction (ND) is normal to the plate (not labelled).

Table 3.1.
Chemical composition of the HP-Ti sample (Unit: part per million by weight, ppmw; other elements in composition are neglected for less than 1.00 ppmw) [Salem et al., 2003a]

O	Fe	S	C	N	Ti
95	1.3	3	7	11	Balance

3.2.2 Mechanical Testing

There were 4 different loading tests in this experiment set: simple compression along ND and TD, simple shear along RD and plane strain compression along ND. All the tests were conducted at a constant strain-rate.

Simple compression tests were performed on cylindrical shaped samples with 5 mm diameter and 7 mm length. They were machined out of the as-received disk and the axis was kept parallel to the plate normal (Figure 3.2). Two simple compression tests or uniaxial compression tests were conducted at a strain-rate of $0.01s^{-1}$ at room temperature. Tests were interrupted for lubrication at each interval between 0.3-0.4 strain deformation. The frictional effects were dealt with by Teflon sheets lubrication and high pressure grease.

The simple shear tests were performed on a uniaxial testing machine using double shear sample geometry [Kaschner et al., 2010]. Since an exact strain-rate condition of this simple shear test was not available and in the former work [Kaschner et al., 2010] by the same research group they had conducted a similar test with an equivalent strain-rate between $0.001\text{-}0.0015s^{-1}$, an equivalent strain-rate of $0.00125s^{-1}$ was chosen as an

approximation in the present simulation work. Samples for this test were cut along the plane surface of the disk, see in Figure 3.2.

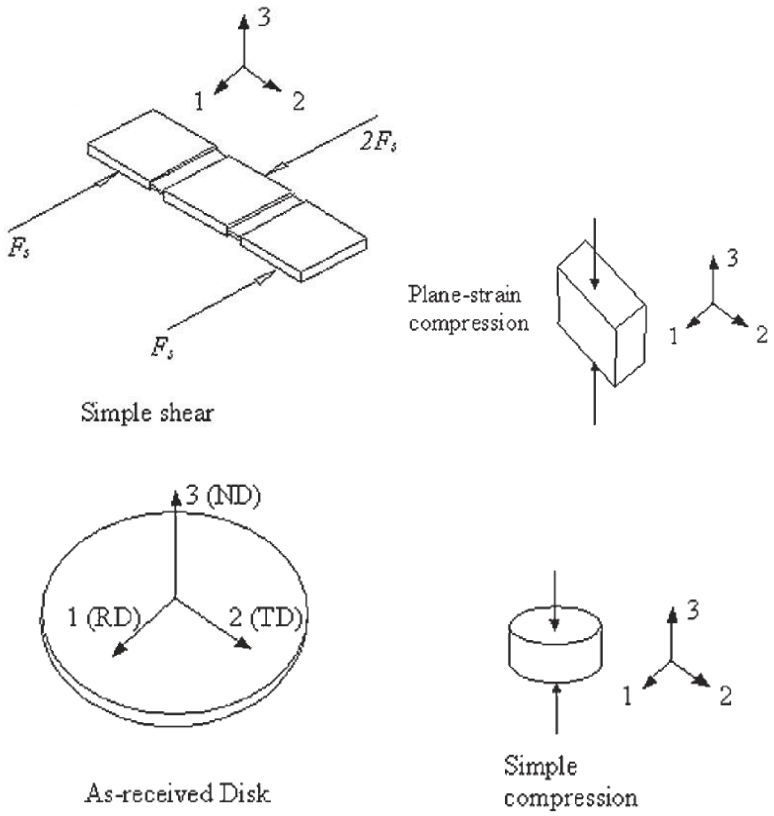

Figure 3.2. Schematics of experiments and specimens in Salem et al. [Salem et al., 2003a].

As for plane strain compression, rectangular shape samples were cut from the raw material and the compression direction was made parallel to the normal of disk. A channel-die fixture was utilized in the test and the Teflon sheets as well as high pressure grease were utilized as lubricants. The relubrication intervals of this test were between each 0.2 true strain increment. A strain-rate of this test was chosen as $0.01s^{-1}$ in the present VPSC simulations, which is kept in accord with the simple compression test. It is

to be noted that an exact experimental strain-rate condition of this test was not presented by the authors in their paper.

3.2.3 Deformation Mechanisms

The stress strain curves measured in the experiments are shown in Figure 3.3.

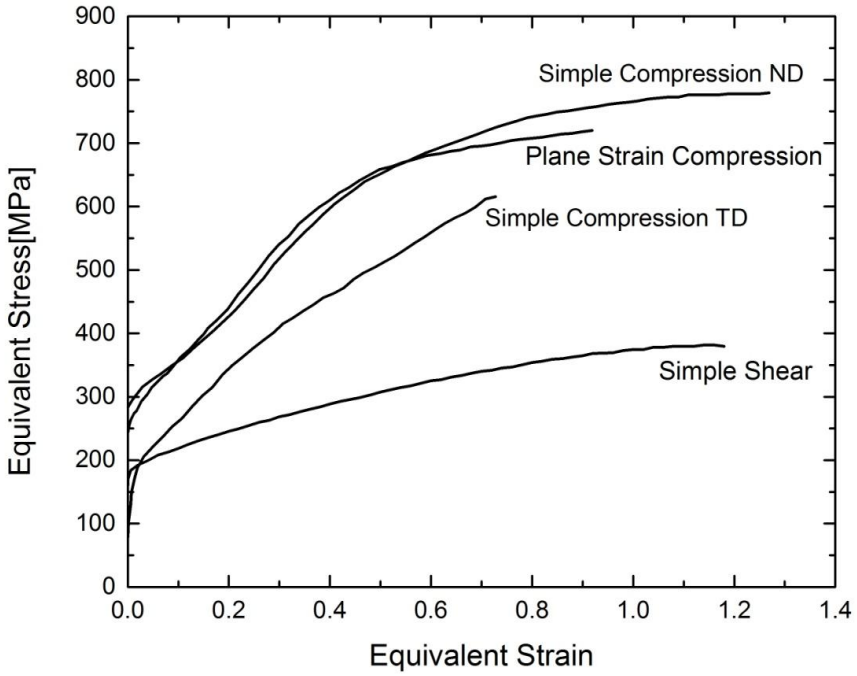

Figure 3.3. Equivalent true stress-equivalent true strain response of mechanical loading tests of HP-Ti [Salem et al., 2003a].

This figure was reproduced with numerical data drawn from the original figure in the literature [Salem et al., 2003a]. Generally, from a comparison between the curves, one could observe that the yield strength in simple shear is the lowest amongst all loading tests, followed by simple compression along TD. ND compression and plane strain

compression have similar yield strength, indicating that ND was the hardest direction. This observation can lead to some reasonable speculation:

• In simple compression along ND and plane strain compression, the dominant deformation mode at early stage has a relatively higher initial CRSS, such as pyramidal <c+a> slip mode according to common experience.

• In simple shear test, easily activated prismatic slip mode can account for the lower yield stress, since it usually has the lowest CRSS at room temperature.

Specifically, simple compression along ND test and plane strain compression test present a three-stage behavior. The detailed strain hardening behavior of these tests as well as simple shear test can be found in Figure 3.4.

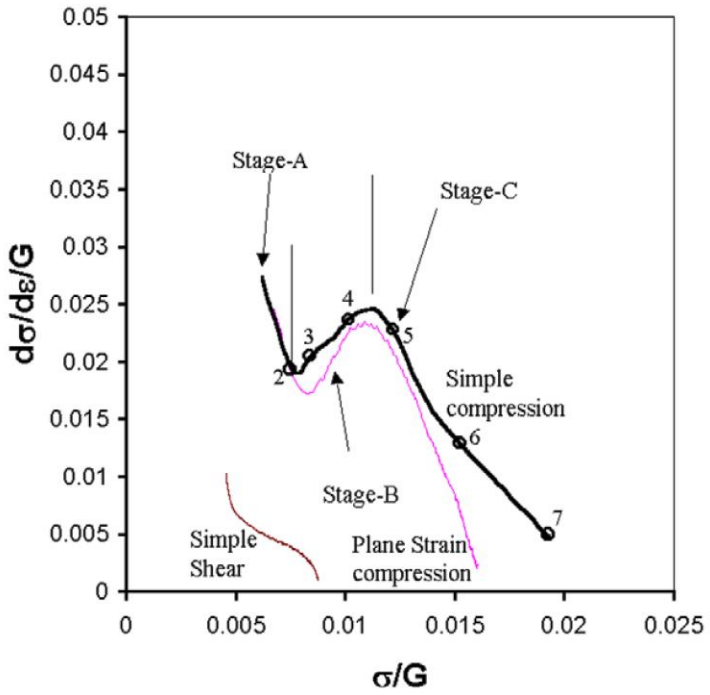

Figure 3.4. Strain hardening response of the mechanical loading tests [Salem et al., 2003a].

In simple compression sample under optical microscope, at equivalent strain of -0.025 ("minus" sign indicates compression), neither annealing twins nor deformation twins have been seen. This sample corresponds to stage A in the figure. When the sample was compressed to -0.05 (with another 0.02 strain compression to reveal slip lines), thin slip lines and thick deformation twins lines were both observed in grains. Salem et al. also claimed that the onset of stage B correlates with the activation of deformation twinning. In other samples with true strains of -0.11, -0.3, -0.5, and -0.93 deformation, the twin density increased substantially corresponding stage C. Moreover, some twin intersections were also observed at lower strain level (equivalent strain -0.3) than in FCC metals, which is much worthy of attention. Through Orientation Imaging Microscopy (OIM) analysis, at true strain of -0.05, only one strong peak at $65°$ appeared in the misorientation distribution, indicating only $\{11\bar{2}2\}$ compressive twin is active at this stage. Figure 3.5 presents a plot of twin volume fraction versus true strain in simple compression. Salem et al. assumed the volume fraction of twins to be the same as the linear density of twins which was calculated by intercept method on the optical micrographs. It needs to be noted that the data for true strain of -0.3 was obtained from the calculation using the OIM map. The plot of twin volume fraction also points out that the twinning activity tended to saturation at a true strain of about -0.2.

For deformed plane strain compression sample, optical microscopy was conducted up to a high strain level. The strain hardening rate there was much lower than in simple compression tests. When equivalent strain was larger than -0.7, evident macroscopic shear bands were observed in the sample characterizing an "X" pattern. This indicates

inhomogeneous and local deformation in the material. However, the localized "X" pattern was not seen in simple compression tests in this work even at true strain of -0.93. Salem et al. carried out further experiments on the HP-Ti samples following the procedure that was applied in their earlier study on FCC metals [Asgari et al., 1997]. In the HP-Ti samples, the examination of microstructures yielded no evidence of localized shear bands which have been observed in FCC metals [Salem et al., 2003a]. This may help to find the reason for the absence of macroscopic shear bands in simple shear test of HP-Ti. Nevertheless, more research is still required to explain this phenomenon clearly.

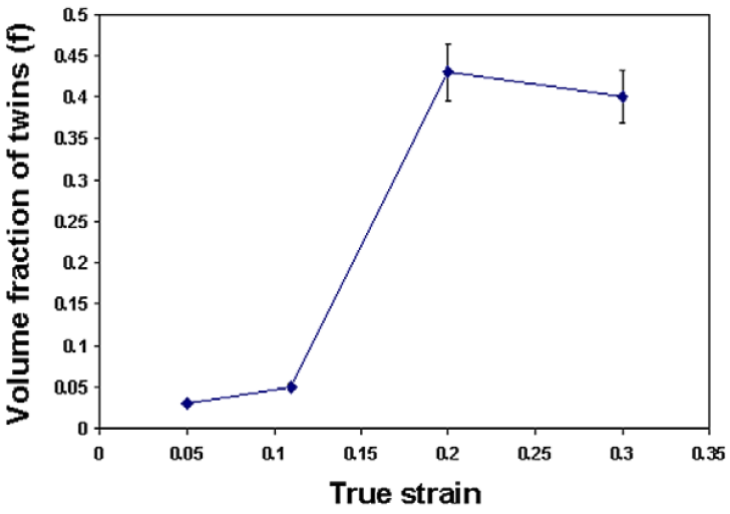

Figure 3.5. Twinning volume fraction evolution in simple compression along ND [Salem et al., 2003a].

As for the simple shear test, micrographs (see Fig. 11 in Salem et al. [Salem et al., 2003a]) were taken from a shear plane which was perpendicular to the disk axis. The shear direction was parallel to the normal direction of the micrographs. From these, one can

observe significantly less deformation twins in simple shear sample than those in simple compression or plane strain compression at the comparable strain levels (compare Figs. 5(h) and Fig. 11 in Salem et al. [Salem et al., 2003a]).

3.3 Modelling Results and Discussion

This section presents the numerical simulation with simulation input conditions, calibration of parameters and comparison of modelling results with those in the literature.

3.3.1 Simulation Input Conditions

Simulation input conditions basically included 4 main types of data: SC calculation settings, orientations/textures data, boundary conditions (loading conditions) and hardening parameters. Each of these conditions was written in an individual file as part of VPSC program.

SC calculation setting was done in the VPSC.in file, which determines a variety of parameters, restrictions and choices during the simulation run. The SC scheme, "neff" was chosen in this simulation, since "neff" and "affine" are two most favourite schemes employed in the literature. An evaluation work will be presented in next chapter to discuss which SC scheme performs the best and the difference between their results.

To reproduce the initial texture of the specimens, 166 initial representative grains/orientations from experiments were provided by the research group of Salem et al. [Salem et al., 2003a].

As for loading conditions, various strain-rate tensor **L** and/or Cauchy stress tensor **σ** as shown below were put into the VPSC7a computer program. They are given as:

(1) Simple compression along ND

$$[L]=\begin{bmatrix}\dot{\varepsilon}_{11} & \dot{\varepsilon}_{12} & \dot{\varepsilon}_{13}\\ \dot{\varepsilon}_{21} & \dot{\varepsilon}_{22} & \dot{\varepsilon}_{23}\\ \dot{\varepsilon}_{31} & \dot{\varepsilon}_{32} & \dot{\varepsilon}_{33}\end{bmatrix},\ [\sigma]=\begin{bmatrix}0 & 0 & 0\\ 0 & 0 & 0\\ 0 & 0 & \sigma_{33}\end{bmatrix},$$

in which $\dot{\varepsilon}_{33}$ and eight "zero" components of **σ** (except σ_{33}) are known conditions. Three diagonal components of **L** should obey the incompressible rule with a sum of zero.

(2) Simple compression along TD

$$[L]=\begin{bmatrix}\dot{\varepsilon}_{11} & \dot{\varepsilon}_{12} & \dot{\varepsilon}_{13}\\ \dot{\varepsilon}_{21} & \dot{\varepsilon}_{22} & \dot{\varepsilon}_{23}\\ \dot{\varepsilon}_{31} & \dot{\varepsilon}_{32} & \dot{\varepsilon}_{33}\end{bmatrix},\ [\sigma]=\begin{bmatrix}0 & 0 & 0\\ 0 & \sigma_{22} & 0\\ 0 & 0 & 0\end{bmatrix}.$$

The loading condition of this test is similar to the one under ND compression.

(3) Simple shear

$$[L]=\begin{bmatrix}0 & \dot{\varepsilon}_{12} & \dot{\varepsilon}_{13}\\ \dot{\varepsilon}_{21} & 0 & \dot{\varepsilon}_{23}\\ \dot{\varepsilon}_{31} & \dot{\varepsilon}_{32} & \dot{\varepsilon}_{33}\end{bmatrix},\ [\sigma]=\begin{bmatrix}\sigma_{11} & \sigma_{12} & 0\\ \sigma_{21} & \sigma_{22} & 0\\ 0 & 0 & 0\end{bmatrix},$$

in which $\dot{\varepsilon}_{12}$ is the known component according to the loading strain-rate.

(4) Plane strain compression

$$[L]=\begin{bmatrix}0 & \dot{\varepsilon}_{12} & \dot{\varepsilon}_{13}\\ \dot{\varepsilon}_{21} & \dot{\varepsilon}_{22} & \dot{\varepsilon}_{23}\\ \dot{\varepsilon}_{31} & \dot{\varepsilon}_{32} & \dot{\varepsilon}_{33}\end{bmatrix},\ [\sigma]=\begin{bmatrix}\sigma_{11} & 0 & 0\\ 0 & 0 & 0\\ 0 & 0 & \sigma_{33}\end{bmatrix},$$

in which $\dot{\varepsilon}_{33}$ is the known component with all "zero" components fixed as well.

In the single crystal data file, Voce hardening parameters and rate sensitivity are determined. Recalling the previously mentioned equation (1.4.3-1):

$$\dot{\varepsilon}_{ij}(\bar{x})=\sum_s m_{ij}^s\dot{\gamma}^s(\bar{x})==\dot{\gamma}_o\sum_s m_{ij}^s\left(\frac{m_{kl}^s\sigma_{kl}(\bar{x})}{\tau_o^s}\right)^n$$

where $\dot{\gamma}_o$, the reference slip rate, was set as a constant of $0.001s^{-1}$ in subroutine files of VPSC program. In this way, quasi-static loading conditions are reflected. Meanwhile, the rate sensitivity n=20 was used in this work. In the original experiment work of Wu et al., a low value of n=50 was applied in the simulation work. In another work by Bouvier et al. [Bouvier et al., 2012], very high rate sensitivity (100<n<200) values were utilized in many cases of titanium deformation. However, a higher value of rate sensitivity will result in significant challenge for numerical simulation, which greatly prolongs the calculation process and even leads to failure for convergence. Moreover, in another work done by Battaini [Battaini, 2008], the same problem was encountered and Battaini claimed that rate sensitivity value above n=20 has little effect on the results [Kocks et al., 1998].

Voce hardening parameters for simulations of tests with different textures can be different, even though the materials are the same. Therefore, respective calibration work (determination of the parameters) should be carried out for each experiment set. Usually, this part of work is accomplished by fitting the simulated results to some of the experimental data, and subsequently comparing the predicted results with the rest of experimental data. The fitted hardening parameters are shown in Table 3.2. Details of determination of the parameters will be discussed in Section 3.3.2.

The 5 deformation modes as underlying mechanisms are chosen according to the experimental observations presented in Section 3.2.3. Prismatic mode usually serves as the dominant slip mode in titanium and has plenty of supporting evidence in literature. Basal and pyramidal slip modes will be activated greatly, when the loading strain is set

along special direction with the crystal orientation. As for twinning, it is already established that the hardening rate changes in ND compression comes from compressive twinning mode. Also, the tensile twin mode is observed commonly in different experiments of titanium. It will also be shown in Section 3.3.3 that tensile twin is necessary for the simulation of TD simple compression test.

Table 3.2.
Voce hardening and PTR parameters for simulation of experiments [Salem et al., 2003a].

No. of s	Mode	τ_0	τ_1	θ_0	θ_1	h^{s1}	h^{s2}	h^{s3}	h^{s4}	h^{s5}	A^{th1}	A^{th2}
1	Prismatic	55	60	45	12	1	1	1	10	1		
2	Basal	120	100	80	0	1	1	1	1	20		
3	Pyramidal<c+a>	120	200	125	45	1	1	1	1	5		
4	Tensile twin	70	0	70	70	1	1	1	1	30	0.8	0.2
5	Compressive twin	135	0	60	60	1	1	1	20	10	0.2	1.0

($h^{ss'}$ is the latent hardening parameter mentioned before, indicating the latent effect of system s' exerted on system s)

From the above table, one can see that the effect of compressive twin on the other deformation modes is of much importance in this simulation because the latent hardening parameters of the other modes caused by compressive twin are large. It is believed that the twinning hardens the stress state by impeding dislocation slip. In ND compression, compressive twin alone dominates strain hardening (or is activated earlier than tensile twin at least), while in TD compression the tensile twin plays the similar role. So the latent hardening parameters between these twin types prevent each other from being activated.

It needs to be noted that there is much experimental data (stress-strain response and texture evolution) of ND compression, in which compressive twin dominates the strain

hardening process. However, there is less measurement for tensile twin and observation about how it works in TD compression test. The calibration of parameters was done with all latent hardening parameters set to "1". This indicates that resistance of each deformation mode will not be influenced by the others. Because of the lack of information for fitting parameters of tensile twin, one can see many latent hardening parameters caused by tensile twin were kept as "1" with no change in the fitting process.

As for PTR threshold values, they are used to control the reorientation of grains from twinning. Since there was no measured data about the texture evolution in TD compression test, A^{th1} and A^{th2} values for tensile twin were determined by the stress-strain curves alone. However, when fitting the threshold values of compressive twin, there was measured texture evolution in ND compression test.

The parameters in Table 3.2 were obtained by fitting the simulated stress-strain curves to the experimental ones for simple compression along ND and TD as well as simple shear. These experiments were able to provide enough information to determine the parameters. For example, simple shear test was dominated by prismatic<a> slip. So the parameters of prismatic <a> could be determined or at least the ranges of its parameters could be narrowed. The other parameters of deformation modes were obtained in similar way. More details of this part will be shown in Section 3.3.2.

The plane strain compression results along with texture results of the simple shear test, which are independently predicted, were used to evaluate the whole work.

3.3.2 Calibration of Parameters

In this section, a brief procedure for fitting the stress strain curves to experiment data is presented as follows:

(1) The values of initial resistance τ_0 on 3 different slip modes are determined by fitting the yield stress of 3 deformation tests to the corresponding measurements. However, it is believed that without twinning modes all the 3 tests cannot be fitted well at the same time (only two at most).

(2) The initial resistance of tensile twin significantly affects the yield stress of simple compression along TD. Similarly, the initial resistance of compressive twin affects the yield stress of simple compression along ND. Further adjustment of yield strength was done by introducing two twinning modes.

(3) The other parameters for prismatic mode, τ_1, θ_0, and θ_1, can be determined with the simple shear experiment data, since prismatic mode almost plays an exclusive role in this test.

(4) τ_1, θ_0, and θ_1 for basal and pyramidal <c+a> are determined by fitting the curves to TD and ND compression measurements, especially at large strain level, because twinning modes tend to saturation at large strain.

(5) The rest of parameters of twinning can be used to adjust the slope of the stress-strain curve at an early stage, especially along ND and TD compression. There is evident change in hardening rate indicating the existence of twinning at small strain level in those two tests. However, these hardening and latent hardening parameters along with PTR threshold values cannot be determined perfectly with this step by step approach. So the

author of this thesis followed the protocol that the adjustment of the latent hardening parameters and PTR threshold values is to be carried out only when there is no way to fit the curves well by changing the single system hardening parameters alone. All the latent hardening parameters were set equal to "1" initially (in this way latent hardening is prohibited), and PTR threshold values were chose as $A^{th1} = 0.15$ and $A^{th2} = 0.40$ by default according to the manual.

3.3.3 Simulation Output Evaluation

The fitting stress-strain response is shown in Figure 3.6 (the Pearson correlations between the measured and simulated data are over 0.99931, which is determined by the TD compression result). It needs to be noted that VPSC program focuses on the plastic deformation stage of the whole stress-strain curve, which means no elastic simulation results will be obtained in this work. Therefore, elastic deformation data is eliminated from the original experiment results. To obtain the experimental plastic data, the elastic strain of each point in original stress-strain curve is calculated with the stresses divided by the Young's modulus of titanium. Then the elastic strain is subtracted from the total strain. A comparison of experimental and simulated stress-strain responses in Figure 3.6 shows good agreement. It is worth noting that the hardening rate changes in ND and TD compression are well reproduced in simulated curves. Figure 3.7 shows the comparison of strain hardening response in simulation and measurement of ND compression, in which the strain hardening rates feature an apparent "three-stages" shape. In simple shear test, linear stress-strain response has been observed, which indicates minimal activation of twinning in this test.

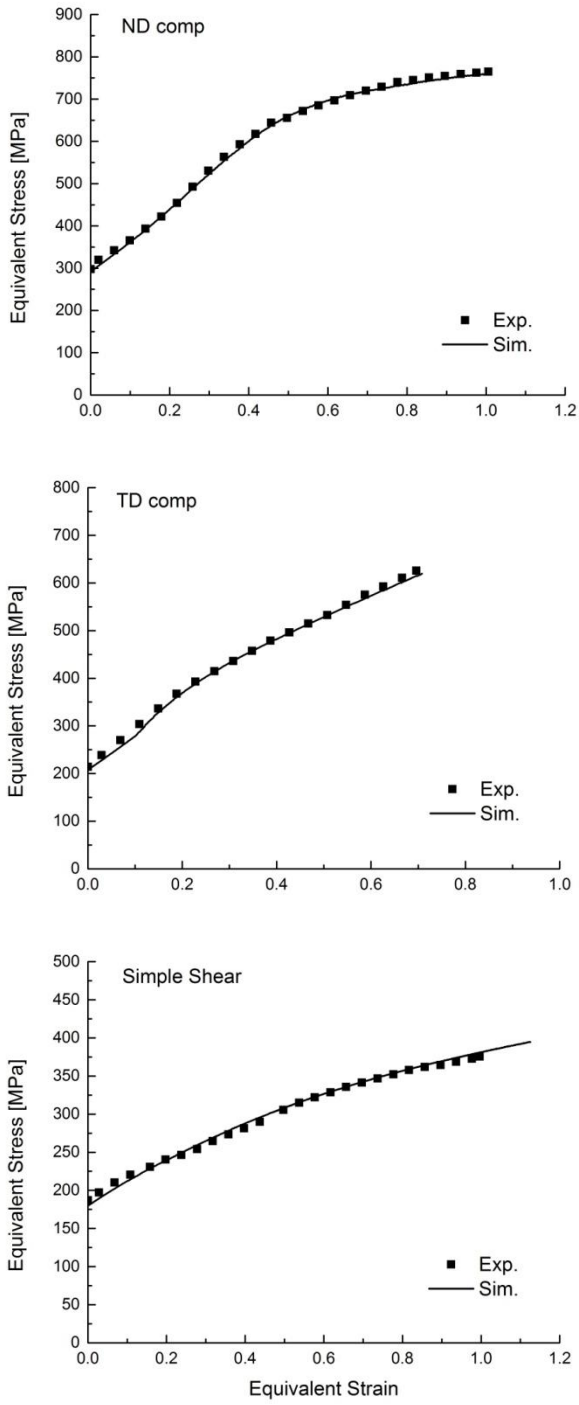

Figure 3.6. Comparison of fitted (Simulated) and experimentally measured equivalent stress-equivalent strain curves (plastic deformation) of 3 deformation tests in Salem et al. [Salem et al., 2003a].

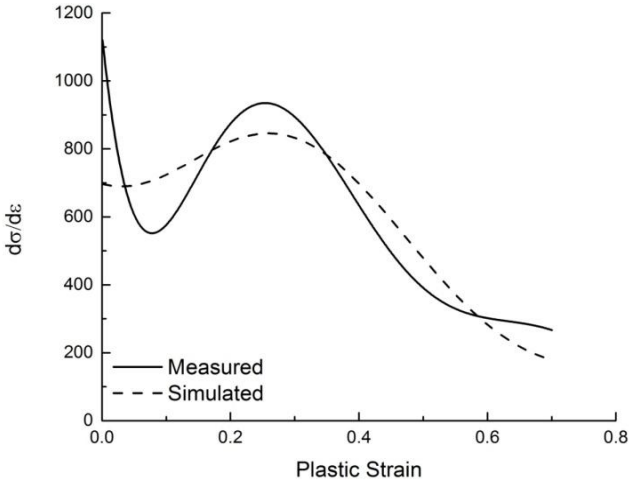

Figure 3.7. Comparison of simulated and measured strain hardening response of titanium in simple compression along ND.

The activation of deformation modes underlying the loading tests can be referred to in the plot of activity calculated by VPSC program (see Figure 3.8). The simulated relative activities also match the experiment observation presented in Section 3.2.3.

In ND compression, loading direction along the c-axis of HCP structure in titanium leads to pyramidal slip mode dominating the deformation until the reorientation of many twinned grains has changed the CRSS of slip modes. As pyramidal slip tends to turn weak for increased resistance, activation of prismatic slip is promoted (see Figure 3.8a). In TD compression test, an exchange of dominating role happens between basal and prismatic slip (see Figure 3.8b). This is due to the different initial texture caused by the in plane loading direction, which has a vital influence on the CRSS of slip/twinning modes. Moreover, the activation of tensile twin at the beginning considerably lowers the yield strength. The yield strength cannot be fitted well without the initial resistance of tensile twin taken into account. Even though the simulation indicates an essential function of

tensile twin, the real mechanism at the beginning of TD compression still remains unknown, which needs further investigation. In simple shear test, a plot of activity reveals the same fact as the experimental observation that twinning has little effect in the deformation mechanism of this test (see Figure 3.8c).

Plane strain compression result is predicted with all the fitted parameters and conditions presented above. This independent result can be used to evaluate this simulation work (see Figure 3.9). The early stage of the predicted curve shows good agreement with measurement and the predicted curve still turns out to have 3 typical stages like simple compression along ND, which matches the measurement very well. The experimentally measured stress-strain responses in ND simple compression and plane strain compression remain close to each other at almost all strain levels during the tests. However, the observation on the plane strain compression sample reveals shear bands existing at large strain. Therefore, the stress state may be lower than theoretical value, since shear bands indicate inhomogeneous and localized deformation which will “soften” the sample material in macro-scale. Moreover, it is worth noting that optical observation on ND simple compression and simple shear samples found no sign of shear bands in the whole strain range of the experiments. So the shear bands are believed to have little effect on the results of these tests.

From the analysis of activity, the underlying mechanisms of plane strain compression turn out to be similar to those in ND simple compression. This serves as a reasonable explanation for the similarity between their stress-strain responses. It is believed that the predicted results could be further improved by incorporating the shear band effect.

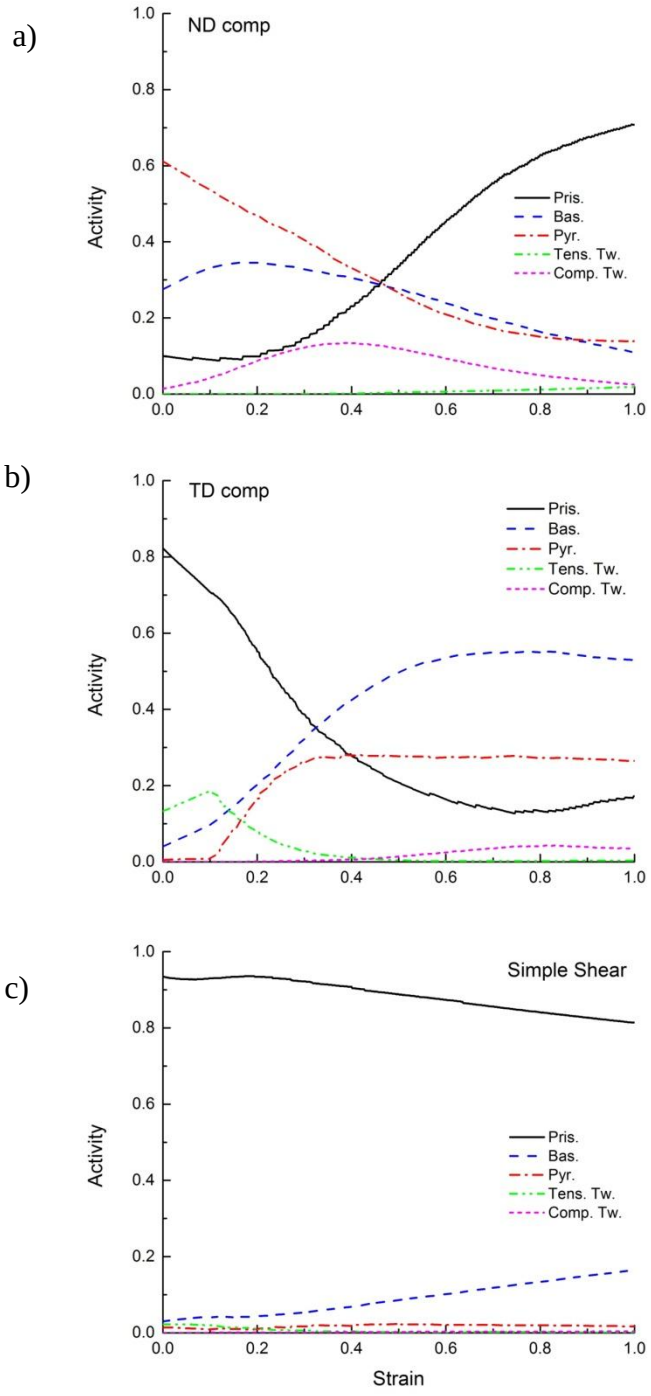

Figure 3.8. Relative activity of each deformation slip/twinning mode in 3 fitted mechanical tests in Salem et al. [Salem et al., 2003a].

a)

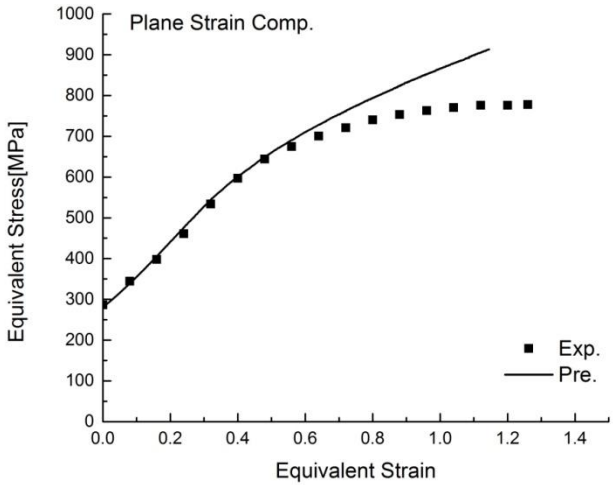

b)

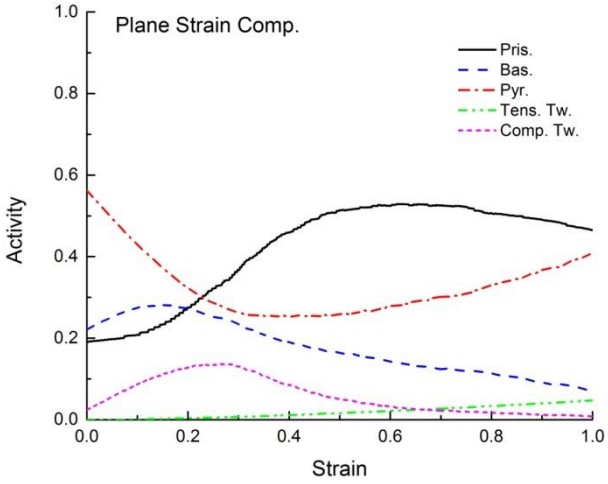

Figure 3.9. a) Comparison of predicted and measured stress-strain response of plane strain compression; b) Relative activity of slip/twinning deformation mode in plane strain compression (experimental data is from Salem et al. [Salem et al., 2003a]).

Despite the agreement between simulated stress-strain curves and the measurements, comparison of textures exhibits some apparent differences (see Figure 3.10). In ND compression, the features of compressive twin were clearly revealed in the texture evolution.

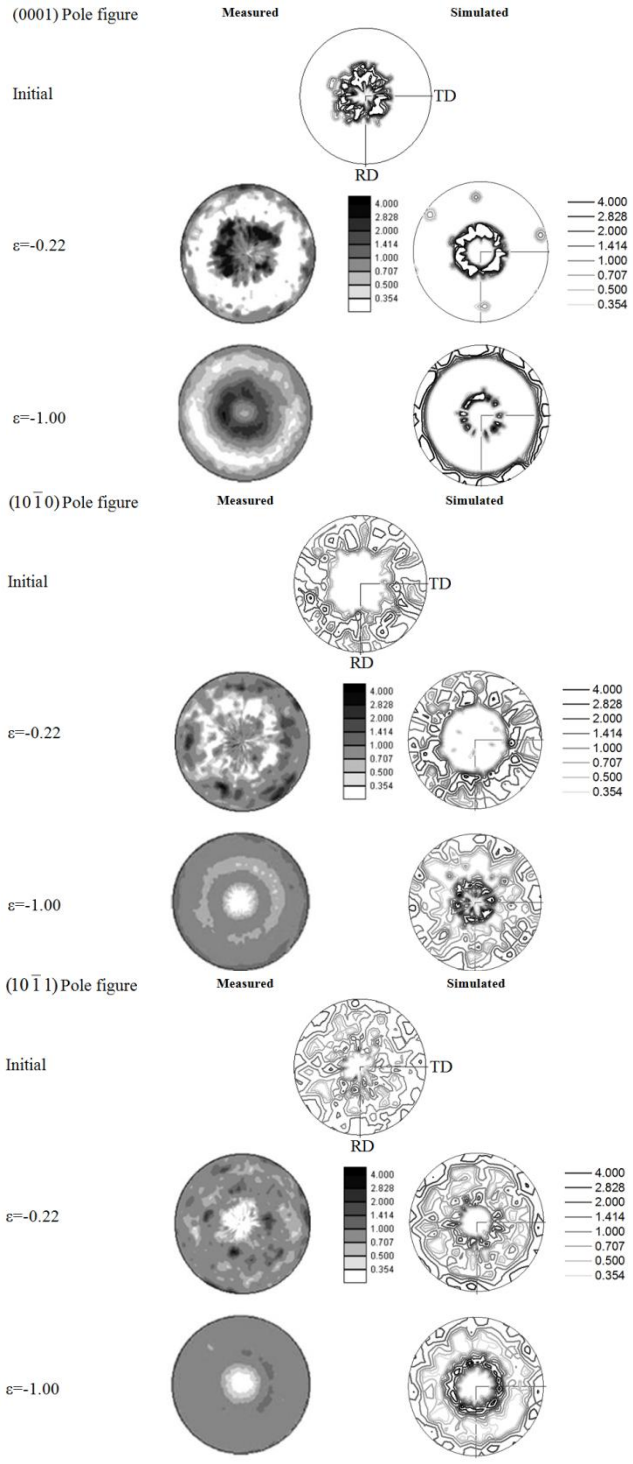

Figure 3.10. Comparison of simulated and measured textures at $\varepsilon = -0.22$ and $\varepsilon = -1.00$ in simple compression along ND (experimental data is from Salem et al. [Salem et al., 2003a]).

In (0001) pole figure, the transformation from a concentration of orientation at the centre of the pole figure to an annular distribution of orientations is due to the compressive twinning and the concentration at the centre of $(10\bar{1}0)$ pole figure is due to this reason as well [Salem et al., 2003a]. However, the simulated texture shows much less twinning activation at $\varepsilon = -0.22$.

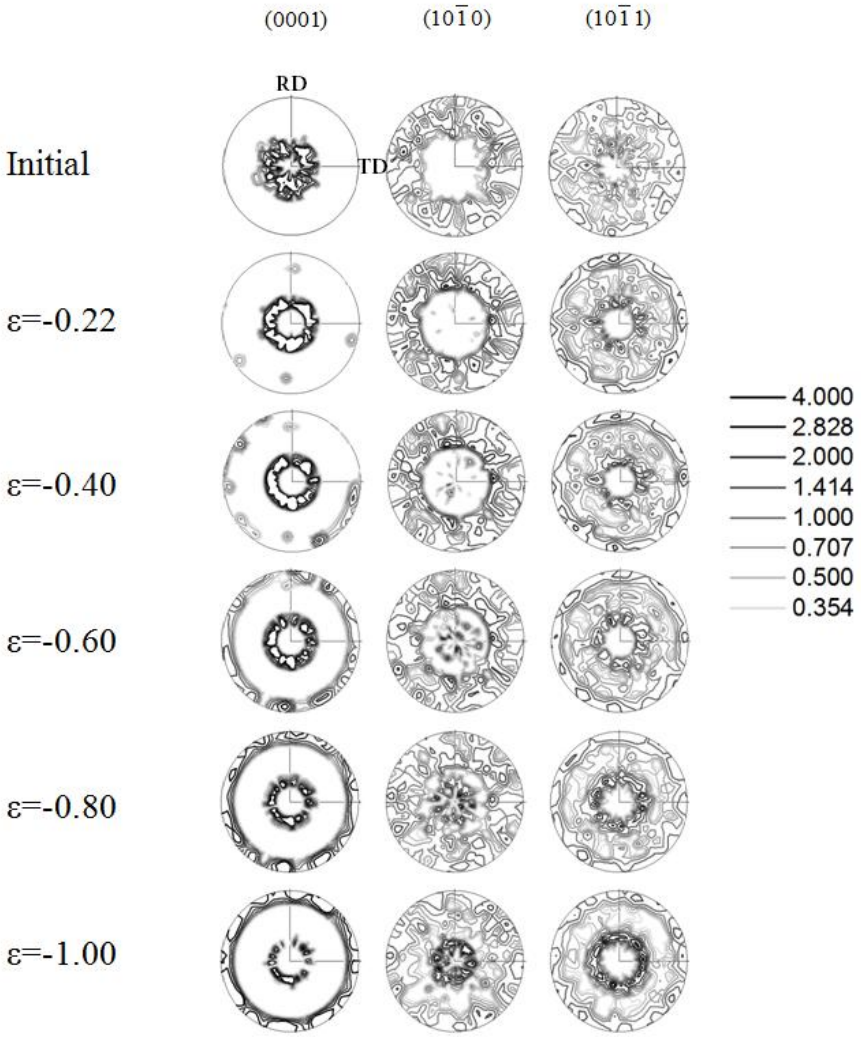

Figure 3.11. Simulated texture evolution in simple compression along ND.

Also, the central distribution of simulated (0001) pole figure at $\varepsilon = -1.00$ is not as strong as the measured one. This problem is probably due to the PTR twinning model implemented in this work. PTR is a simplified twinning model to save the calculation effort, as discussed in Section 2.4.4. In this simulation work, totally 166 grain orientations are considered and the number of orientations remains constant because of PTR model. It is believed that twinning process will produce more new orientations besides the ones of parent grains. So this may result in reduced orientation distribution in simulation compared to the measurement. It is to be noted that 166 initial grains are much less than the number of grains in other simulation works published in literature in the first place.

Texture results for simple shear tests are shown in Figure 3.12. The $(10\bar{1}0)$ pole figure clearly reproduced the measured texture featuring six strong texture components. The predicted (0001) pole figure successfully captured the strong component at the centre, but missed the weaker component near the rim. From the earlier texture evolution and activity analysis, it is likely that the weak component in (0001) pole figure may come from the minimal twinning activation in simple shear tests. It can be observed in predicted texture that little distribution of orientations is present near the edge, as in simulated (0001) pole figure of ND simple compression at $\varepsilon = -0.22$. The same reason for the difference between prediction and measurement may apply here as well. In other words, better twinning model and more initial orientations may improve the final results.

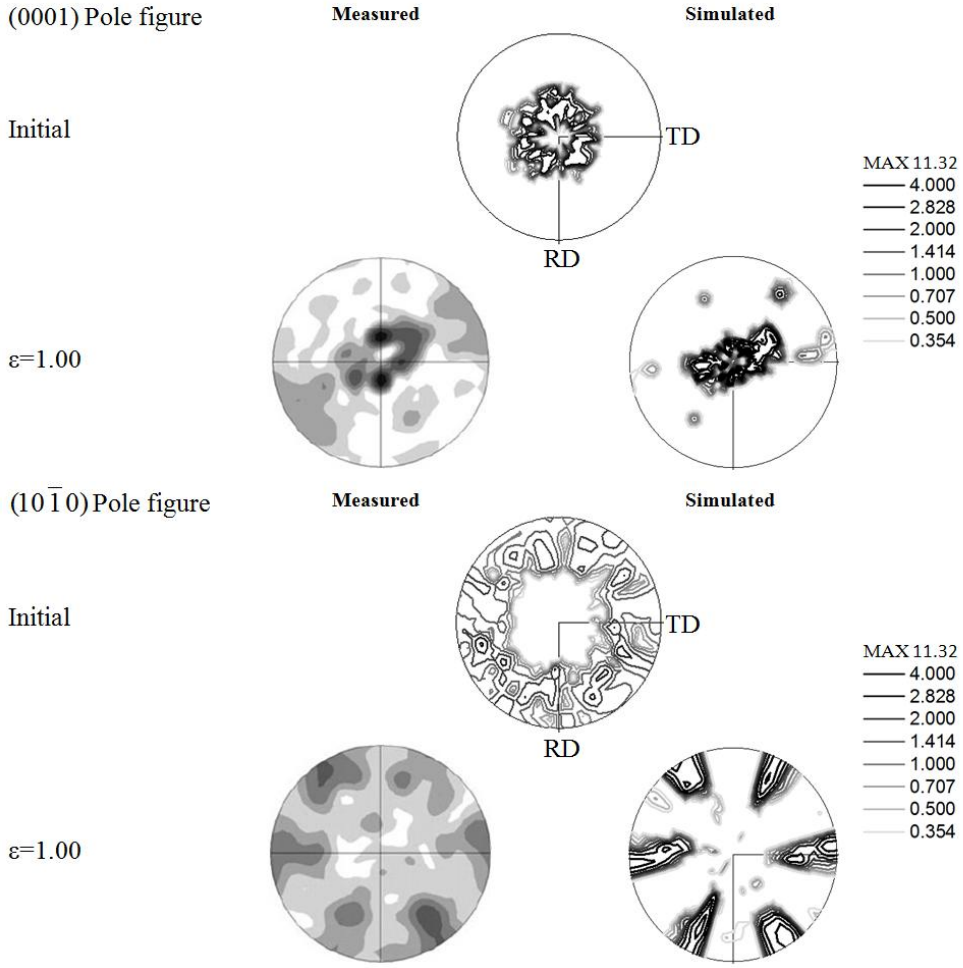

Figure 3.12. Comparison of simulated and measured textures at $\gamma = -1.00$ in simple shear test (experimental data is from Salem et al. [Salem et al., 2003a]).

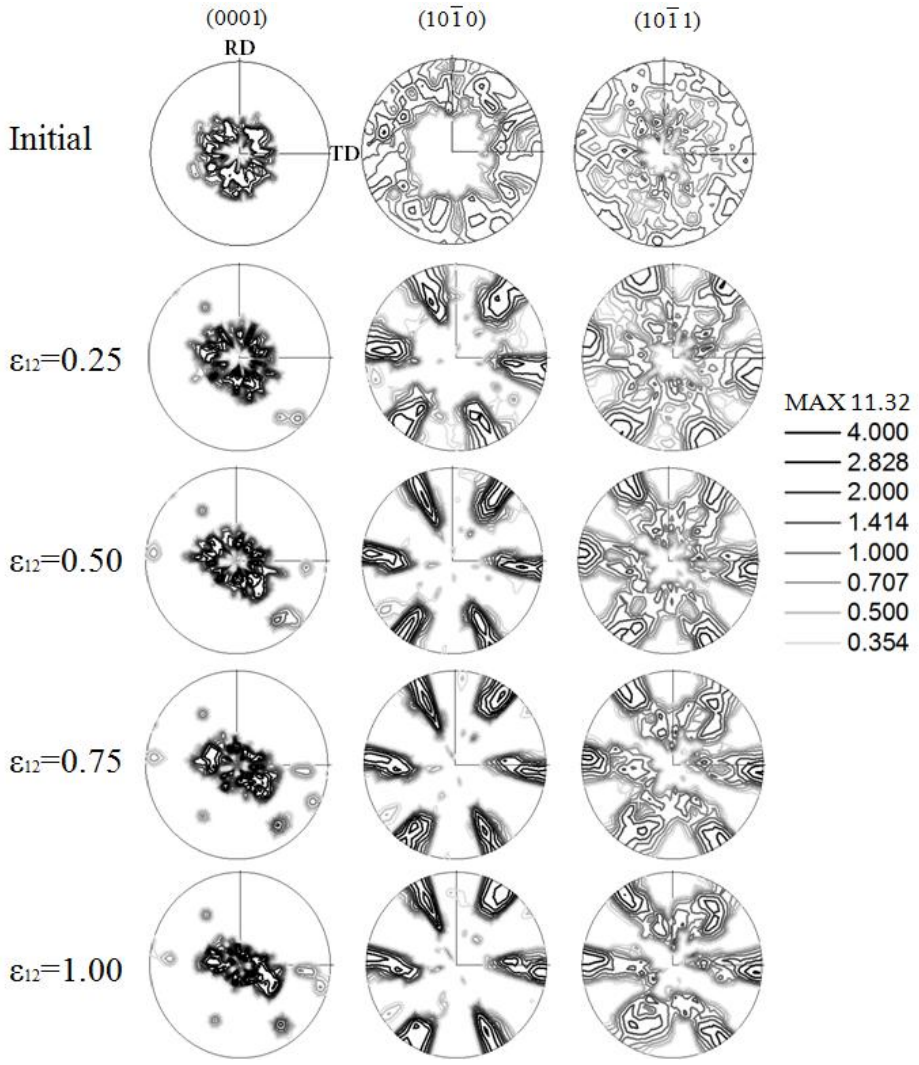

Figure 3.13. Simulated texture evolution in simple shear test.

3.4 Comparison of Results

A simulation work of the experiments of Salem et al. was conducted and presented in another article [Wu et al., 2007]. Wu et al. applied a numerical model which is different from VPSC model. The simulated stress-strain responses are shown in Figure 3.14 (Fig. 3 of Wu et al. [Wu et al., 2007]). The predicted stress of simple shear test was

overestimated in the equivalent strain range of 0.6-1.0. Similarly, the prediction of simple compression along TD test is also higher than measurement at early stage. These flaws of the simulation in Wu et al. [Wu et al., 2007] were eliminated by VPSC model in this thesis (see Figure 3.6).

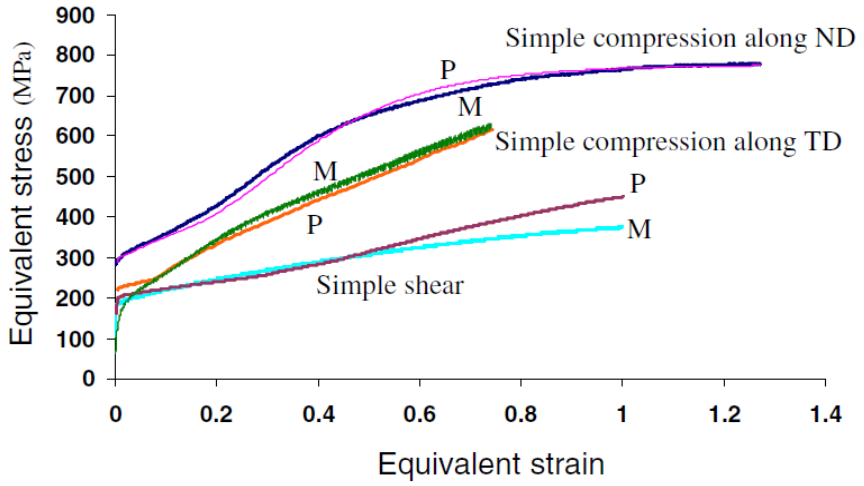

Figure 3.14. Comparison of predicted (P) and measured (M) equivalent stress-equivalent strain curves for different mechanical loading tests on HP-Ti [Wu et al., 2007].

Texture prediction of Wu et al. [Wu et al., 2007] are shown in Figure 3.15, Figure 3.16 and Figure 3.17 (Fig. 6, Fig. 7 and Fig. 8 in Wu et al. [Wu et al., 2007]). These predictions are "closer" to the measurement compared with the results of this thesis, especially for (0001) pole figures of ND compression test (compare Figure 3.10 with Figure 3.15). The reason for this phenomenon has been discussed in Section 3.3.3. Better result can be expected from VPSC simulation with improved twinning model. For the texture prediction of simple shear test, both works missed some of the key features of the measurement (compare Figure 3.12 with Figure 3.17). However, the differences only remain in (0001) pole figure.

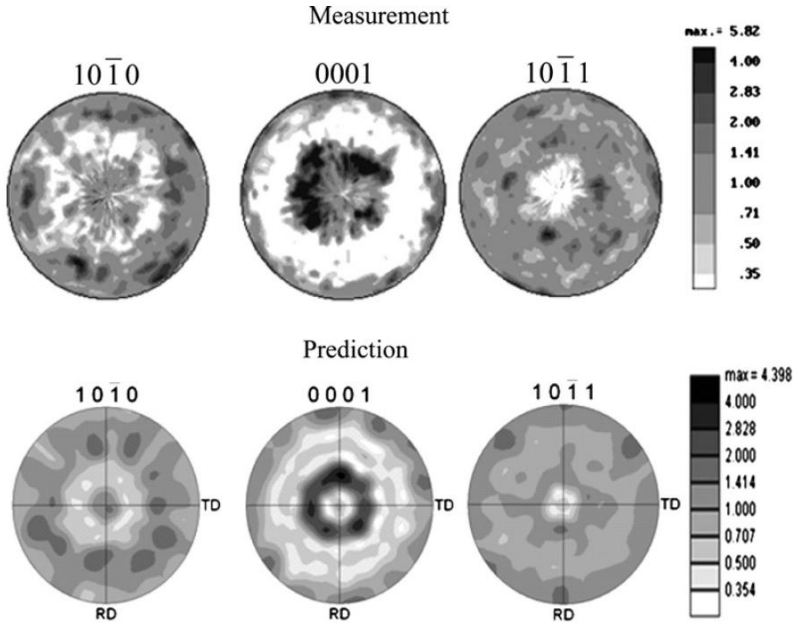

Figure 3.15. Comparison of simulated and measured textures at ε=-0.22 in simple compression along ND of HP-Ti [Wu et al., 2007].

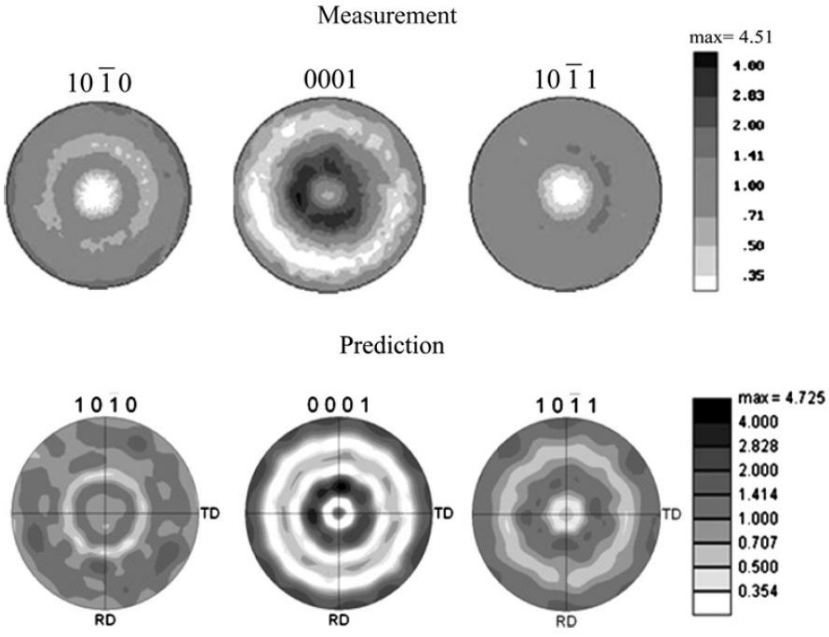

Figure 3.16. Comparison of simulated and measured textures at ε=-1.00 in simple compression along TD of HP-Ti [Wu et al., 2007].

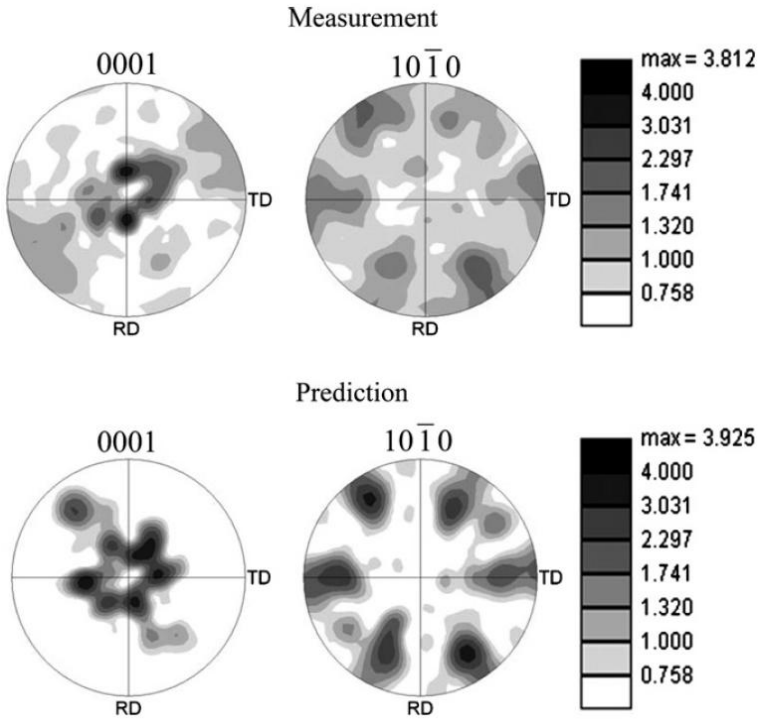

Figure 3.17. Comparison of simulated and measured textures at γ=-1.00 in simple shear of HP-Ti [Wu et al., 2007].

3.5 Summary

In this chapter, VPSC simulations of a series of HP-Ti mechanical tests have been presented. With comparison between the present work and the simulation done by others [Salem et al., 2005; Wu et al., 2007], it is obvious that VPSC model improved the accuracy of the simulation of stress-strain response. However, the texture prediction showed different results. It is worth of noting that the Wu et al. applied a Taylor type crystal plasticity model with a twinning scheme which is more advanced than PTR. The better prediction of stress-strain response may indicate the superiority of SC model to Taylor model even with a simplified twinning scheme. Nevertheless, further studies with

more advanced twinning schemes, such as TDT, are still required to gain a better and more convincing result.

Chapter 4 Evaluation of the Effect of Different Self-Consistent Schemes on Simulation Results

4.1 Introduction

VPSC model is one of the most accurate approaches for macroscopic crystal plasticity modelling, which has already been demonstrated in the previous chapter. However, within the VPSC program, many SC schemes or linearization assumptions have been proposed during the past several decades. Also there are no detailed rules for program users to follow in the selection of a scheme that works best for a specific investigation. At least, in the term of a specific material, it still needs to be determined as to which SC scheme is the most suitable one for titanium.

In this chapter, preliminary discussion and research around this question will be carried out, since the effectiveness of SC scheme relies on a variety of factors. Moreover, the comparison between the simulations of this thesis and other simulations presented by Knezevic et al. [Knezevic et al., 2013] reveals the role of basal<a> slip mode in the deformation of titanium. It is to be noted that both of the simulation studies are based on the same experiments [Nixon et al., 2010].

4.2 Experimental Conditions

A series of tests were conducted on HP-Ti (99.999%) by Nixon et al. (2010) and the reader is referred to Nixon et al. [Nixon et al., 2010] for specific details. For completeness, much of the experimental details from Nixon et al. are reproduced below.

4.2.1 Material

The material used in the above work was purchased from Alpha Aesar of Johnson Matthey Electronics, Inc., Spokane, WA, USA. The raw material was provided in the form of cross-rolled disk with 15.87 mm thick and 254 mm diameter. Through optical microscopy observation, the as-received material was found to have equiaxed grains with average grain size of 20 μm.

Twenty samples were cut from the disk with dimensions of 19.05 mm × 19.05 mm × 15.87 mm, using water jet at the perimeter of the plate, such that two neighboring samples were separated by an angle of 11.32°. Schematic of the raw material and locations of specimen with initial measured texture can be seen in Figure 4.1.

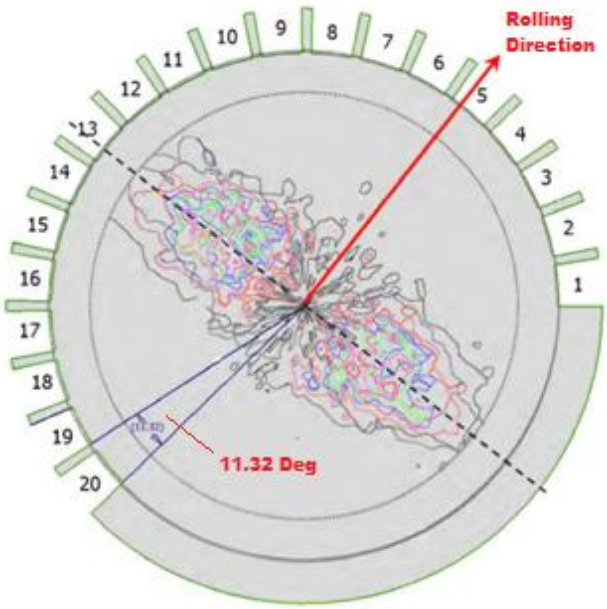

Figure 4.1. Measured (0001) pole figure of basal plane in initial state plotted in the schematic of as-received disk with dimensions of the samples [Nixon et al., 2010].

4.2.2 Mechanical Testing

The experiments conducted in this work consisted of 3 uniaxial tension and 3 uniaxial compression tests. For each of the principal directions (ND, TD and RD), there were two tests corresponding to tensile and compressive loading respectively. These tests were referred to as quasi-static characterization tests with a nominal strain-rate of $0.001s^{-1}$ at room temperature. The geometry of the tensile specimens is shown in Figure 4.2.

a)

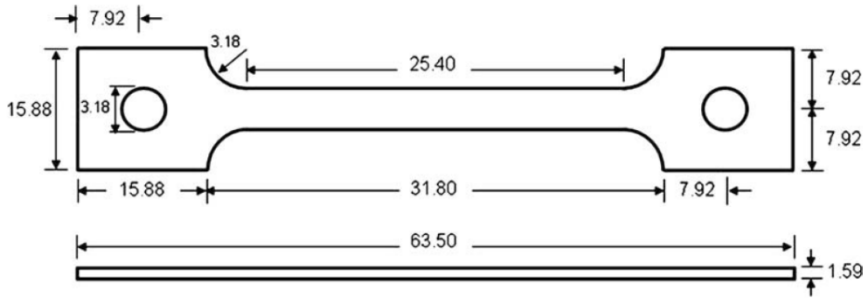

b)

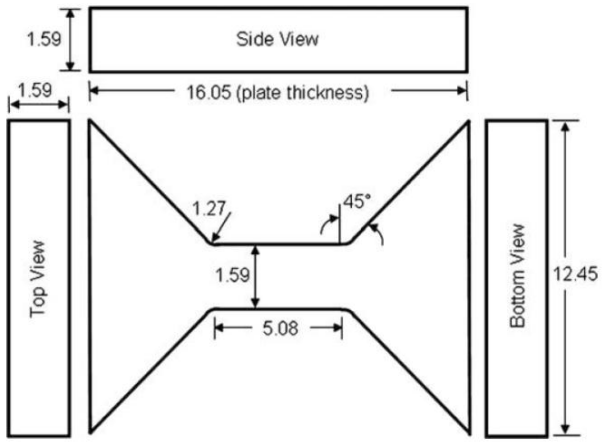

Figure 4.2. a) Geometry and dimensions (mm) of tension specimen used for in-plane tests (RD and TD); b) Geometry and dimensions (mm) of tension specimen used for through-thickness test (TT/ND) [Nixon et al., 2010].

It should be noted that tensile specimen for ND direction has different dimensions from the ones in the other two directions. Because of the geometrical restriction of as-received disk, the miniature ND test specimen caused a 10% error in the final results [Kaschner et al., 2010].

As for compression tests, cylindrical specimens with dimensions of 7.62 mm × 7.62 mm were machined along three directions (two in-plane directions and one through-thickness). In each test, load was applied continuously with no interruptions and the effect of friction has been relieved with Molykote lubricant sprayed onto the platens before tests.

4.2.3 Deformation Mechanisms

The stress strain results of this experiment reveal pronounced anisotropy in this material (Figure 4.3).

However, anisotropy in tension is more evident than in compression, since in tension tests, even the elastic behavior in three directions show apparent difference from each other. During compression process, only minor barreling in the specimens was observed, which makes data of compression test more reliable in simulation.

Further comparison between tension and compression along the same direction leads to more information about the underlying mechanisms.

Along RD direction (Figure 4.4), tension and compression are not significantly different from each other until about 10% strain. In compression test, one can observe sharp increase in hardening rate and slight tendency to decrease after 30% strain. The whole curve has a typical shape with 3 stage of deformation hardening as mentioned earlier, which indicates the existence of twinning mechanism. Moreover, this can be verified by

texture evolution in Figure 4.4 with evidence of large grain reorientation resulting from twinning. Also for tension along RD, the stress state changes gradually with hardening rate monotonically decreasing. The latter behavior is a clear indication of slip dominated deformation.

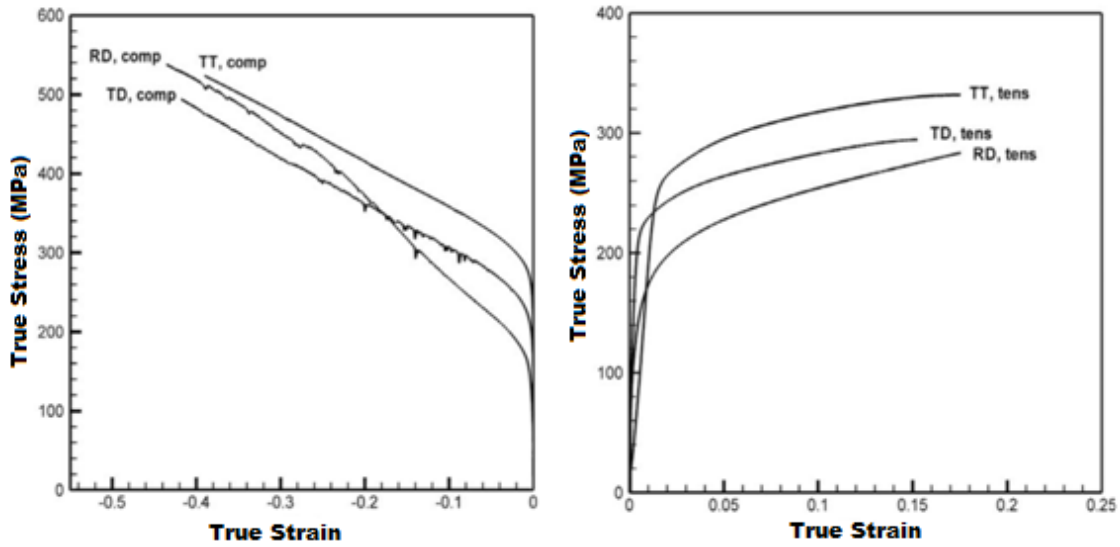

Figure 4.3. Uniaxial compression and tension tests results along rolling (RD), transverse (TD), and normal direction (ND) or through-thickness direction (TT) [Nixon et al., 2010].

However, loading along the transverse direction (TD) does not show features present in RD direction test (Figure 4.5). For both tension and compression, there is no significant change in hardening rate during the deformation process. This may be indicative of little deformation twinning. Moreover, the texture measurement reveals similar conclusion with minimal texture evolution, which is another indication for slip dominated deformation.

a)

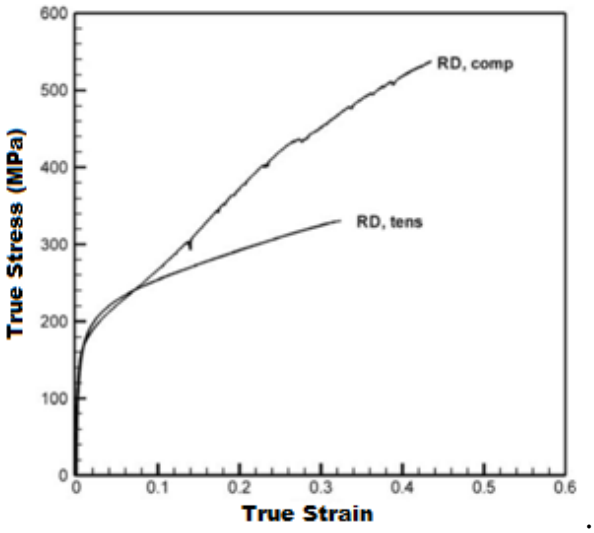

b)

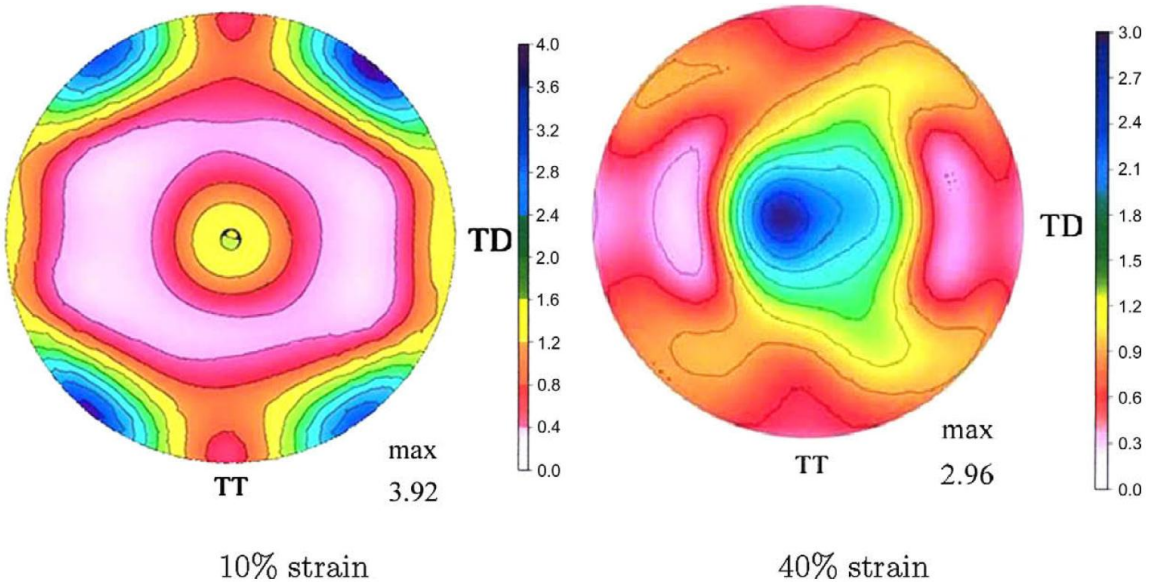

Figure 4.4. a) Tension and compression response along RD; b) (0001) pole figures of compression samples along RD. Scale represents multiples of random distribution (mrd) [Nixon et al., 2010].

a)

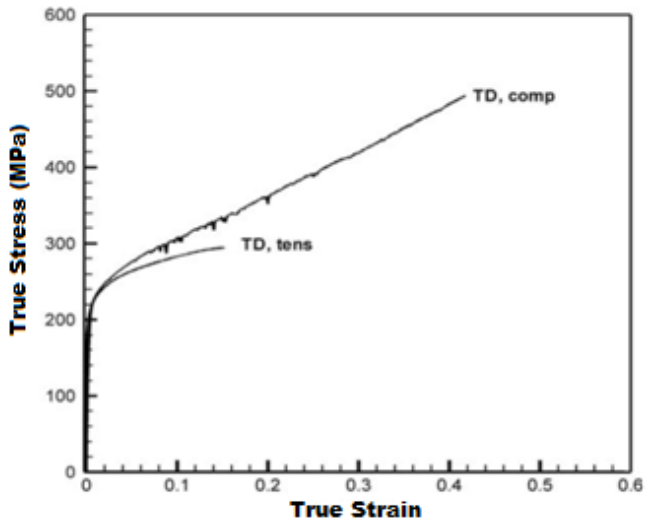

b)

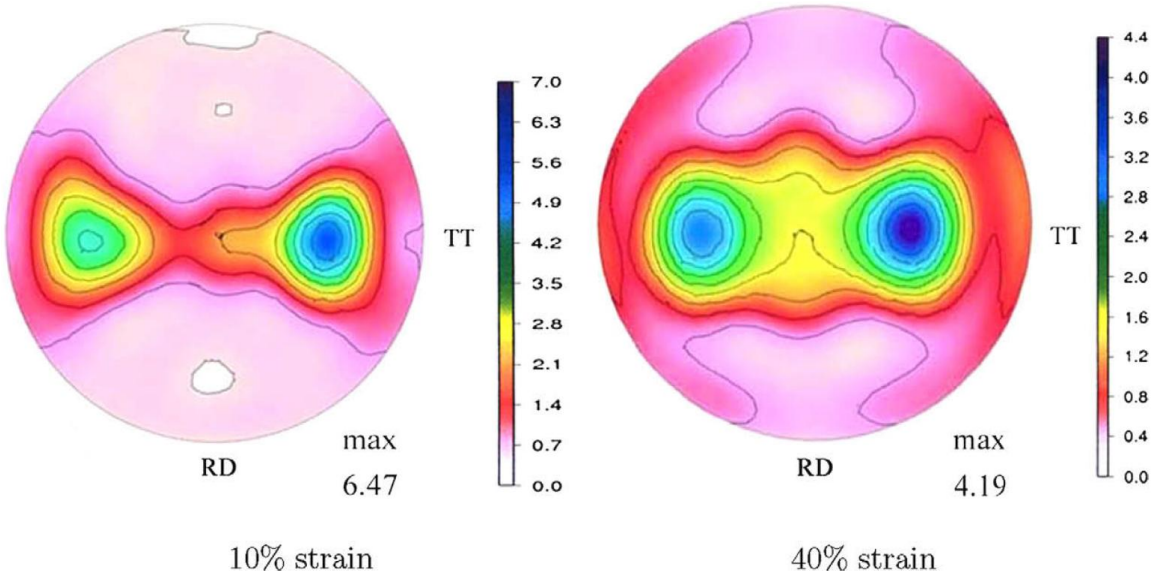

Figure 4.5. a) Tension and compression response along TD; b) (0001) pole figures of compression samples along TD. Scale represents multiples of random distribution (mrd) [Nixon et al., 2010].

At last, quasi-static test results of uniaxial loading along ND/TT direction are shown in Figure 4.6.

a)

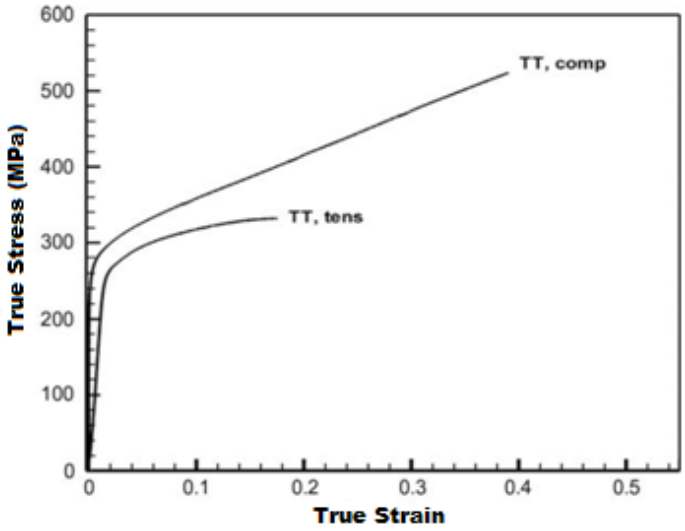

b)

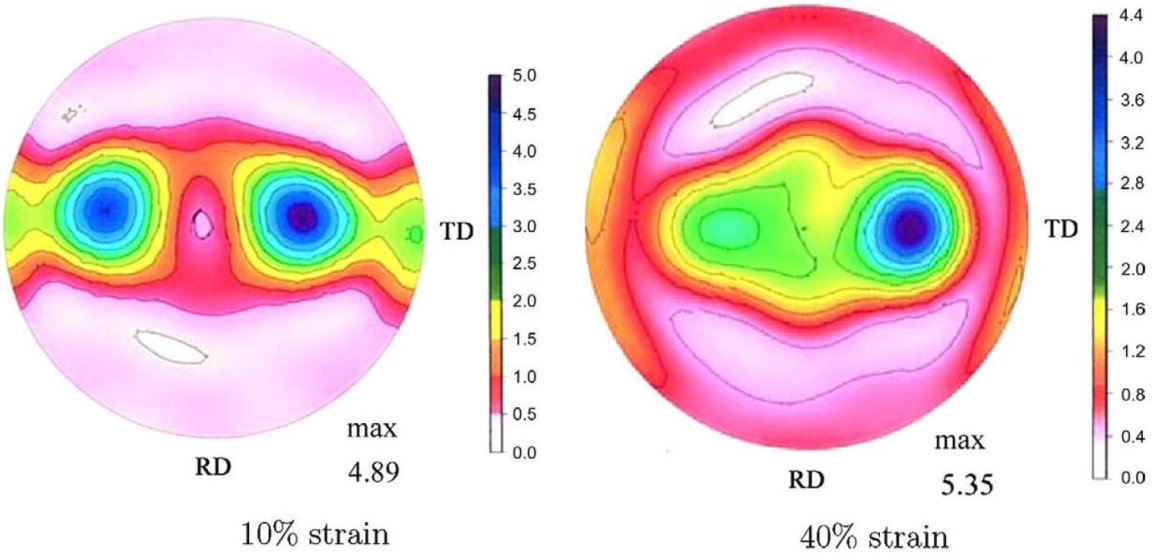

Figure 4.6. a) Tension and compression response along ND/TT; b) (0001) pole figures for compression samples along ND/TT. Scale represents multiples of random distribution (mrd) [Nixon et al., 2010].

It is easily noted that there is a strong tension/compression asymmetry in yielding stress, which acts as a unique feature, and clearly different from the other two groups of tests. This indicates that different deformation mechanisms have been activated in tension and compression tests. Nevertheless, one cannot ignore the possibility that the special geometry of the ND tension sample (see Section 4.2.2) causes the difference between yield stresses. From the view of texture evolution, similar conclusion to TD tests that little twinning systems have been activated can be drawn.

It should be noted that, in all of the tension tests, shear type fracture has been observed, while in other HCP crystal structure materials, for example AZ31B, tensile fracture is typically brittle.

4.3 Modelling Results and Discussion

4.3.1 Simulation Input Conditions

In the simulation work of this experiment set, “affine”, “neff=10”, “secant” and “tangent” SC schemes were adopted in VPSC program in sequence during the calculation. More details of these 4 SC schemes were provided in Section 2.4.2.5.

To generate the initial texture numerically, the researcher utilized 500 grains/orientations as representatives for the sample, which were measured and provided by the research group of Nixon et al. [Nixon et al., 2010]. The reproduced initial texture is shown in Figure 4.7.

Loading conditions/ boundary conditions for these tests appear in a common form, since all of the tests were done under uniaxial loading conditions. As for the common form of

the tensors, the readers are referred to the loading conditions for simple compression in the experiments of Section 3.3.1.

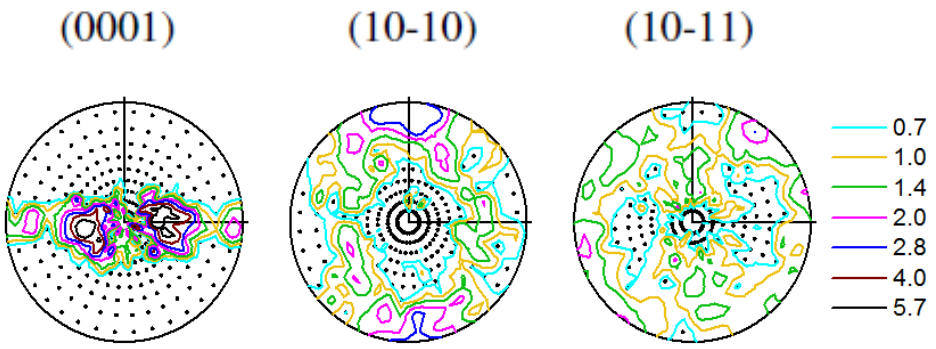

Figure 4.7. Numerical created initial texture of the experiments in Nixon et al. [Nixon et al., 2010].

In the constitutive equation (1.4.3-1),

$$\dot{\varepsilon}_{ij}(\bar{x}) = \sum_s m_{ij}^s \dot{\gamma}^s(\bar{x}) = = \dot{\gamma}_o \sum_s m_{ij}^s \left(\frac{m_{kl}^s \sigma_{kl}(\bar{x})}{\tau_o^s} \right)^n$$

$\dot{\gamma}_o$ is set 1.0 in this work, as stated in Nixon et al. [Nixon et al., 2010]. The magnitude of $\dot{\gamma}_o$ affects Voce hardening parameters. However, it will not influence the final simulation result, as a multiplication factor. So the exact magnitude of Voce hardening parameters has limited significance when compared to the hardening parameters in other simulation works, but the ratio between the resistances of different modes is the one that needs to be noted. As for the rate sensitivity, n=20 is still applied in this simulation.

Voce hardening parameters in the simulation with 4 SC schemes are presented in Table 4.1, with only 4 deformation modes taken into account. In the experimental observation, the compressive twinning is only found to be a secondary twinning mode, which is

activated within the primary tensile twins [Nixon et al., 2010]. Moreover, it should be noted that the experimentally measured ND compression stress-strain curve in this set has a different shape from the one in the former experiment set. In this test, ND compression curve show little evidence of the typical "three-stage" hardening, since the initial texture is different from the one in Salem et al. [Salem et al., 2003a].

Table 4.1.
Voce hardening and PTR parameters for simulation of experiments in Nixon et al. [Nixon et al., 2010].

Affine											
No. of s	Mode	τ_0	τ_1	θ_0	θ_1	h^{s1}	h^{s2}	h^{s3}	h^{s4}	A^{th1}	A^{th2}
1	Prismatic	45	25	300	50	1	1	1	10		
2	Basal	130	70	3000	50	1	1	1	10		
3	Pyramidal<c+a>	160	50	2000	200	1	1	1	1		
4	Tensile twin	180	0	0	0	1	1	1	1	0.15	0.40
neff=10											
No. of s	Mode	τ_0	τ_1	θ_0	θ_1	h^{s1}	h^{s2}	h^{s3}	h^{s4}	A^{th1}	A^{th2}
1	Prismatic	60	30	500	80	1	1	1	10		
2	Basal	130	40	3000	40	1	1	1	10		
3	Pyramidal<c+a>	165	60	2500	180	1	1	1	1		
4	Tensile twin	180	0	0	0	1	1	1	1	0.15	0.40
Secant											
No. of s	Mode	τ_0	τ_1	θ_0	θ_1	h^{s1}	h^{s2}	h^{s3}	h^{s4}	A^{th1}	A^{th2}
1	Prismatic	50	50	100	0	1	1	1	10		
2	Basal	110	60	3000	60	1	1	1	10		
3	Pyramidal<c+a>	160	60	2000	180	1	1	1	1		
4	Tensile twin	195	0	0	0	1	1	1	1	0.15	0.40
Tangent											
No. of s	Mode	τ_0	τ_1	θ_0	θ_1	h^{s1}	h^{s2}	h^{s3}	h^{s4}	A^{th1}	A^{th2}
1	Prismatic	70	35	1000	100	1	1	1	10		
2	Basal	130	40	3000	30	1	1	1	10		
3	Pyramidal<c+a>	155	80	3000	180	1	1	1	1		
4	Tensile twin	180	0	0	0	1	1	1	1	0.15	0.40

($h^{ss'}$ is the latent hardening parameter mentioned before, indicating the latent effect of system s' exerted on system s)

From the latent hardening parameters in this test, it is obvious that the hardening effect of twinning exerted on slip modes is still significant. As for PTR threshold values, the researcher used the default value initially and made no adjustment during the fitting process. The stress-strain curves of RD compression and tension as well as ND compression are set as fitting targets. The remaining experiment results, which are stress-strain responses of ND tension, TD compression and tension along with the measured texture evolution, are used for evaluating the prediction result. In the RD tension test, prismatic <a> slip mode dominates the deformation, which can provide information for determining the parameters of prismatic <a> mode. Other parameters can be obtained with this combination of tests, since all of the deformation modes are activated during these experiments.

4.3.2 Calibration of Parameters

The fitting procedure is shown below to demonstrate the calibration process and to explain the reason for choosing two RD tests and one ND test for fitting:

(1) The 3 quantities of initial resistance τ_0 on slip modes were determined by fitting the yield stress of 3 deformation tests (RD compression, RD tension and ND compression) to the corresponding measurements. In this experiment set, all three yield stresses could be well fitted with only slip modes.

(2) The other parameters for prismatic mode, τ_1, θ_0, and θ_1, were determined with the RD tension experiment data, because prismatic mode is the only dominating mechanism underlying this test.

(3) τ_1, θ_0, and θ_1 for basal and pyramidal <c+a> were determined by fitting the curves to ND compression measurements and the early stage of RD compression. Tensile twinning are least activated within these tests.

(4) All the parameters of tensile twinning were determined with the experimental data of RD compression and that of ND compression test at large strain stage. In RD compression test, twinning volume fraction reaches to 0.8 when true strain equals 0.4, indicating strong influence of twinning mode on stress state.

(5) The latent hardening parameters are determined at the same time when the parameters of tensile twinning are obtained. The stress state is raised through hardening process which comes from the effect exerted on slip dislocations by twinning. The latent hardening parameters are just used to describe this phenomenon.

4.3.3 Simulation Output Evaluation

The fitting stress-strain response is shown in Figure 4.8. The elastic deformation data is also eliminated from the figures, since VPSC provides no elastic stress-strain results. Figure 4.8 shows the results of the different SC schemes where all SC schemes appear to show quite similar results (the Pearson correlations between the measured and simulated data are: 1. RD compression, $p \geq 0.99851$; 2. RD tension, $p \geq 0.99648$; 3. ND compression, $p \geq 0.99609$; the lower bounds are determined by the results of SC schemes with the lowest correlation values). However, in the plot of activity (see Figure 4.9 and Figure 4.10), it is easier to discriminate different schemes. “neff=10” and tangent scheme turn out to be very similar to each other. This is due to the nature of their mathematical expressions which have been presented earlier in Section 2.4.2.5.

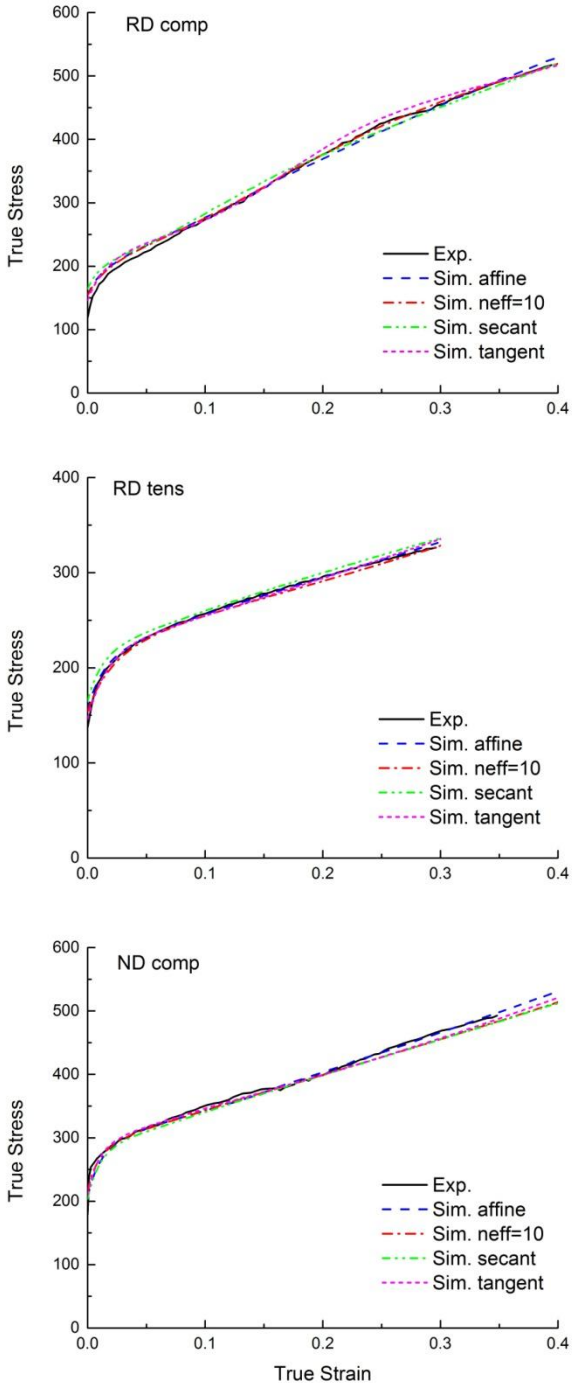

Figure 4.8. Comparison of fitted (Simulated) and experimentally measured true stress-true strain curves (plastic deformation) of 3 deformation tests in Nixon et al. [Nixon et al., 2010].

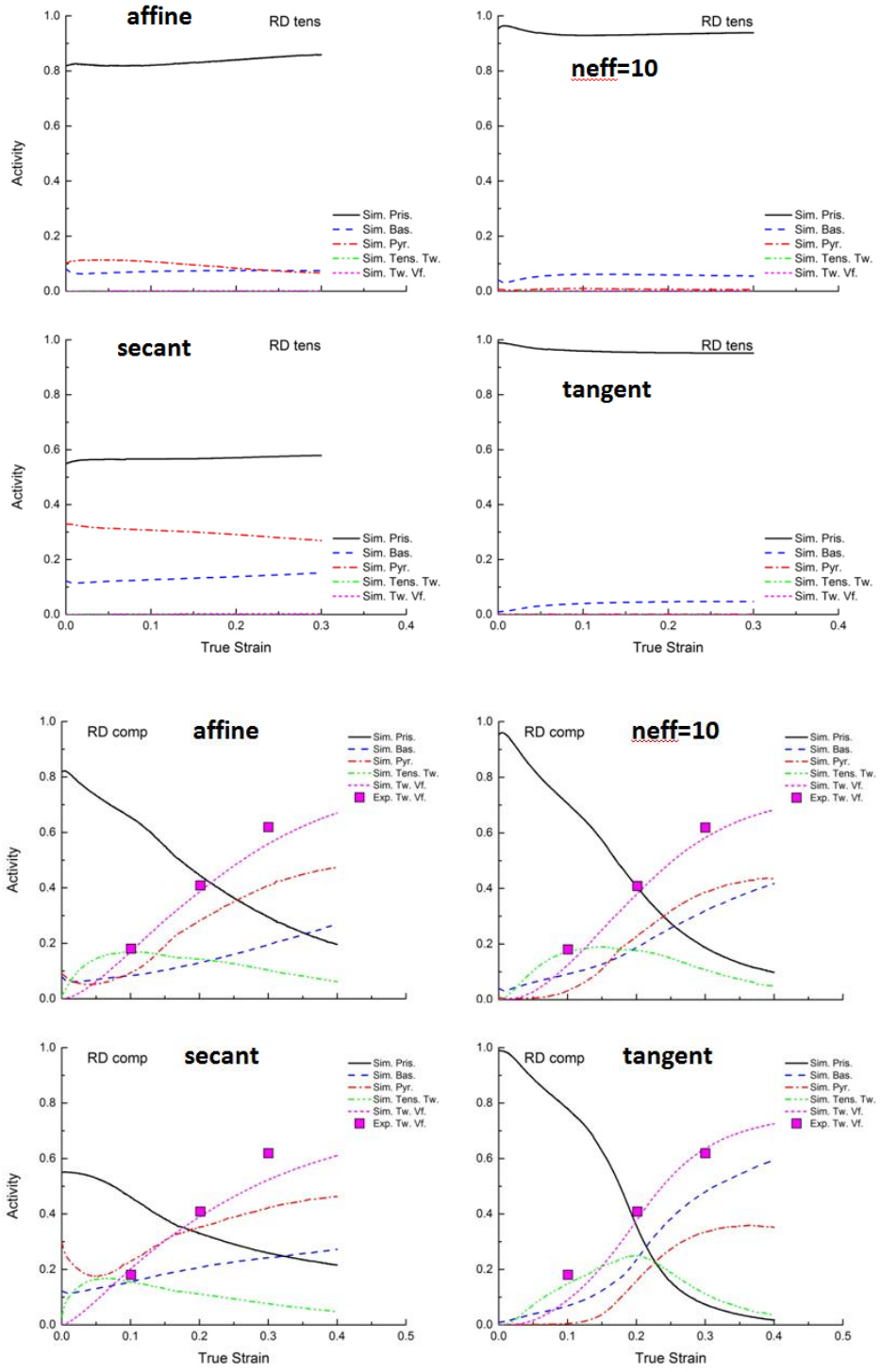

Figure 4.9. Relative activity of deformation modes simulated with 4 different SC schemes in RD tension and compression.

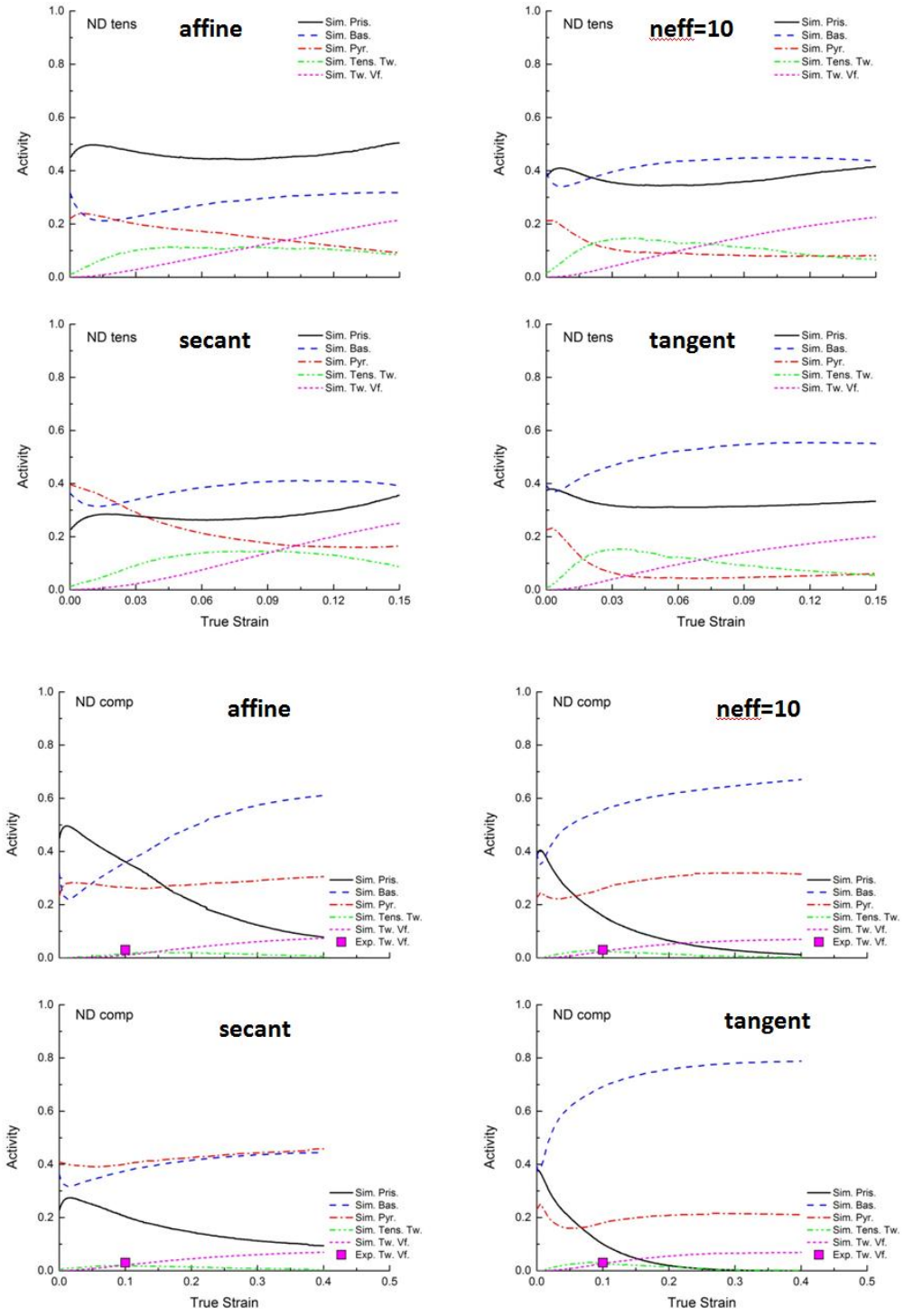

Figure 4.10. Relative activity of deformation modes simulated with 4 different SC schemes in ND tension and compression.

When n=10, these two schemes share the same expression. For n=20 case, it is still difficult to find any significant differences between the different schemes. Secant scheme provided the most distinguishing result and affine scheme result seem to be in the middle of them.

The differences in the prediction of activities is in accord with that described in Wang et al. [Wang et al., 2010a] which is another paper discussing the SC schemes in Mg alloy. But from the stress-strain curves, these relations or differences are not obvious at all in titanium. This may indicate another difference between titanium and magnesium.

Figure 4.11 presents the predicted results of the other three mechanical tests in this work. Clearly, the predictions match the experiments well and the differences among the SC schemes still remain much smaller than expectation (the Pearson correlations between the measured and simulated data are: 1. TD compression, $p \geq 0.99776$; 2. TD tension, $p \geq 0.99362$; 3. ND tension, $p \geq 0.98952$; the lower bounds are determined by the results of SC schemes with the lowest correlation values). Since rate sensitivity "n" can affect the difference amongst the various results, further studies need to be done with higher value of rate sensitivity "n" to discover the real underlying mechanism. The first step will be the improvement of the VPSC model in hand and solve the problem of program collapse while simulating with the cases with higher rate sensitivity "n" (n=20 is the highest value the program can accept at present). On the other hand, the result presented here indicates that different SC schemes do not give rise to much distinction in the results like in other materials, such as magnesium. This result still has significance in guiding the future work about the simulation of titanium.

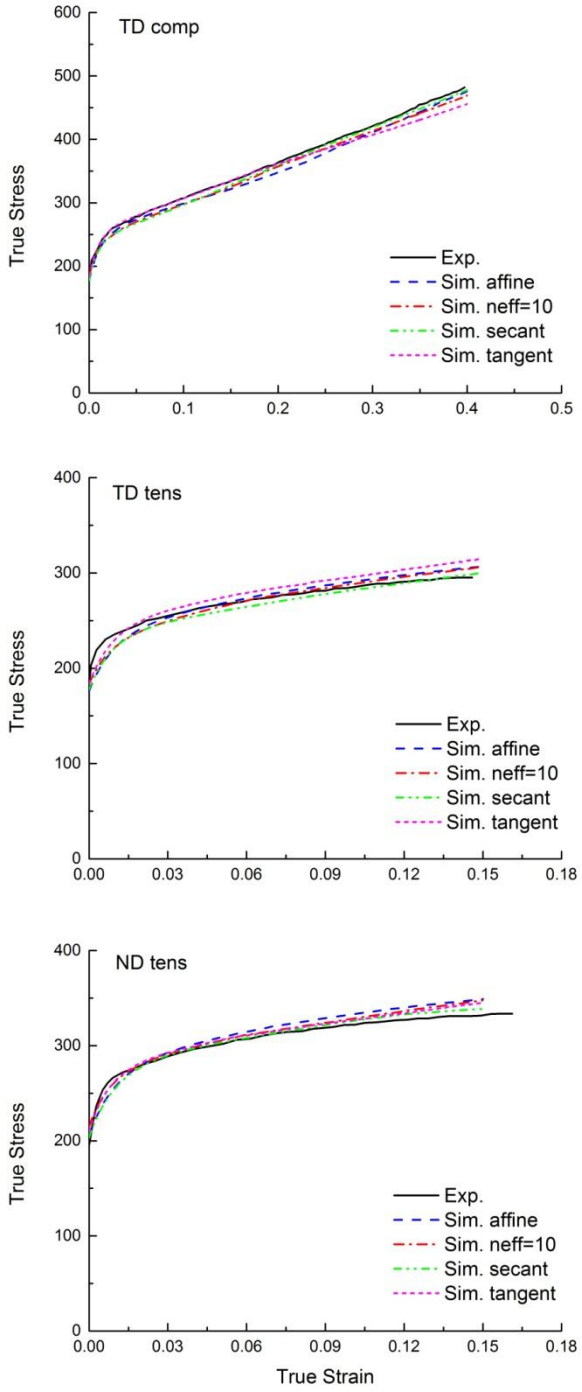

Figure 4.11. Comparison of predicted and experimentally measured true stress-true strain curves (plastic deformation) of 3 deformation tests in Nixon et al. [Nixon et al., 2010].

In the following Figure 4.12, texture evolution predicted using “neff=10” scheme is presented, since the differences in texture evolution predicted by 4 SC schemes are also minimal. From the texture comparison, one can see evident flaws in (0001) pole figures which evolve with increasing strain.

It has already been confirmed that the abnormal concentration of the orientations towards the centre of pole figures is caused by basal <a> slip mode. The author of the thesis conducted a trial simulation without basal <a> taken into account and all the other parameters were kept the same. The result shows no sign of such concentration. Furthermore, the simulation work carried out in Knezevic et al. [Knezevic et al., 2013] adopted VPSC model with 3 deformation modes (without basal <a>). There is no such phenomenon in their prediction of textures either. A comparison between the simulation works of two groups will be presented in detail in Section 4.4.

As has been discussed in Section 2.2.2.2, for polycrystal titanium, the existence of basal <a> slip mode is still under controversy. Based on the result of this thesis, a conclusion can be drawn that basal <a> slip mode is not as common as one of the primary slip modes in the deformation of single crystal titanium. However, the existence of basal slip as, one of the deformation mechanism in VPSC, has improved the accuracy of the results in Knezevic et al. [Knezevic et al., 2013] (see Section 4.4). The introduction of basal <a> gives rise to a better stress-strain response prediction but a rather poor texture evolution prediction.

RD compression

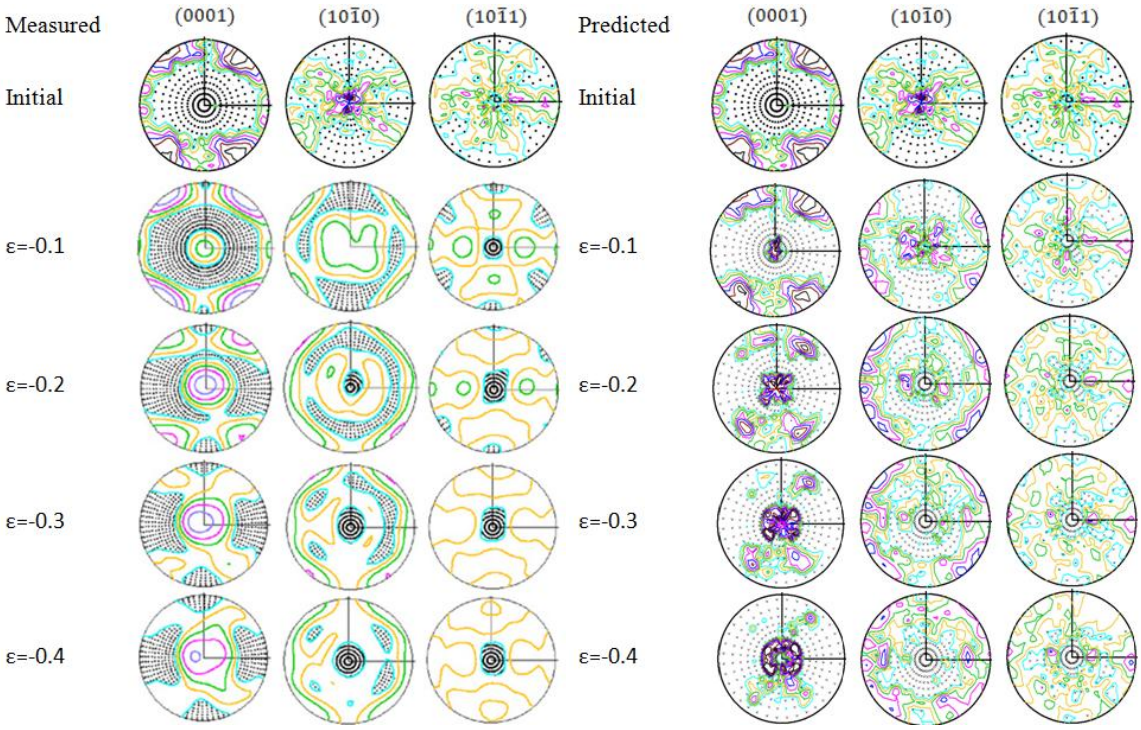

TD compression

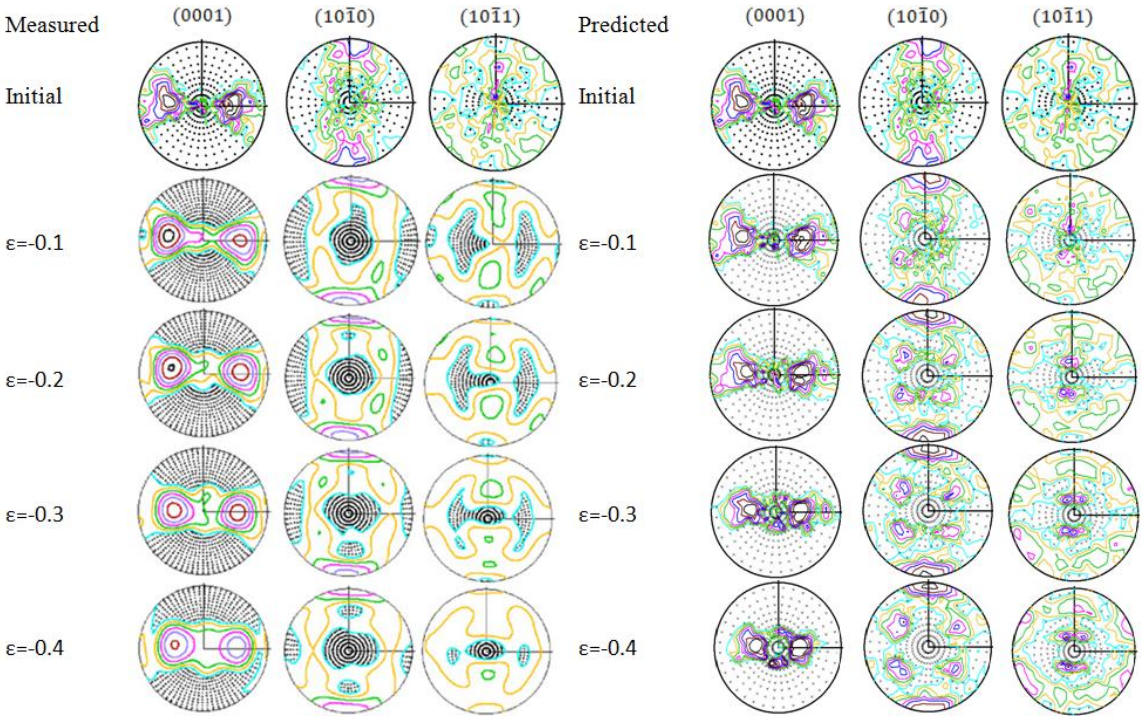

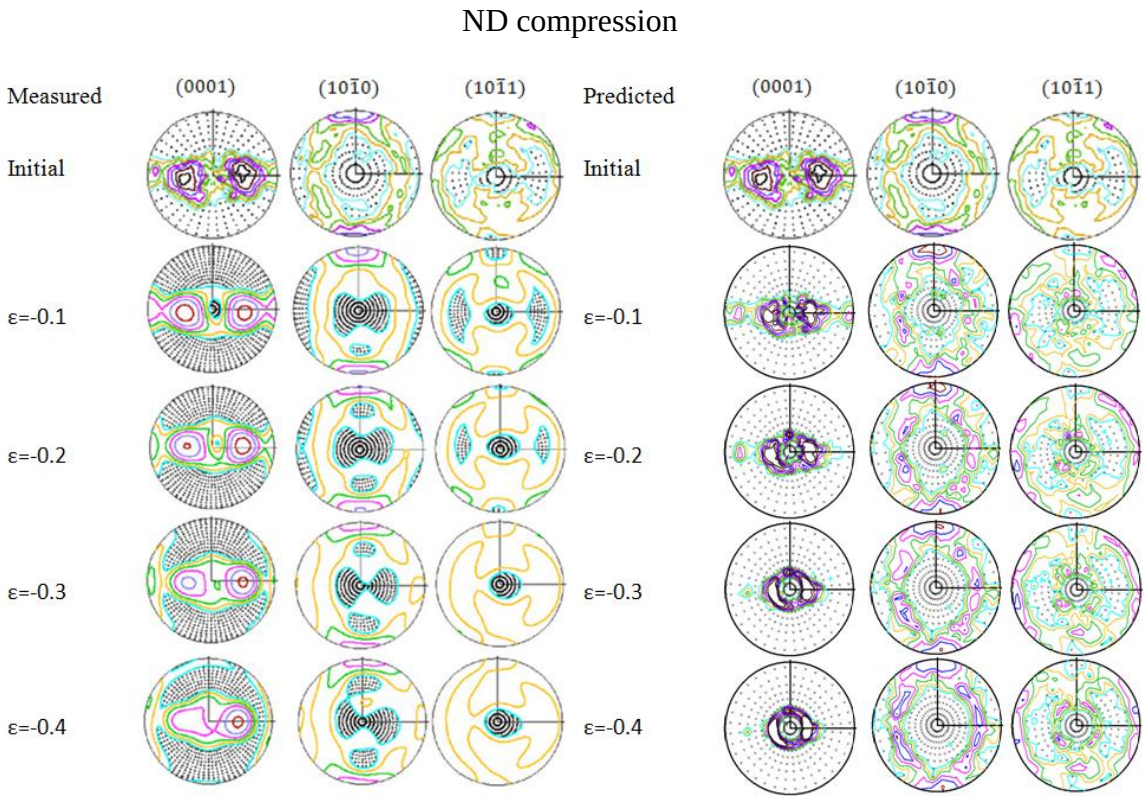

Figure 4.12. Texture evolution comparison of measurement in Knezevic et al. [Knezevic et al., 2013] and prediction of the thesis in three compression tests (pole figures were drawn with the same legend as Figure 4.7).

4.4 Comparison of Results

Knezevic et al. conducted a simulation work using VPSC model which is the same numerical method applied in this thesis. Only 3 deformation modes (prismatic<a>, pyramidal1<c+a> and tensile twin) were considered in their work, while in this thesis, the basal<a> mode was added in for the purpose of studying its function.

The prediction of stress-strain responses in Knezevic et al. [Knezevic et al., 2013] is shown in Figure 4.13 (Fig. 3 in Knezevic et al. [Knezevic et al., 2013]). It is obvious that prediction of TD tension is overestimated compared to the measurement and the results of

TD compression and tension appear to be the same. In Figure 4.11, this evident flaw has been eliminated in the simulation in the present work.

Figure 4.14 shows the predicted textures of 3 compression tests in Knezevic et al. [Knezevic et al., 2013] (no measured and simulated textures of tension tests were provided in the paper).

Compared with Figure 4.12, the (0001) pole figures of ND compression test in Knezevic et al. [Knezevic et al., 2013] are apparently "closer" to the measurement. However, their results cannot be regarded as a good match of the measured data. For example, in the predicted (0001) pole figures of ND compression, there is a "hole" at the center of the distribution. This "hole" can also be seen in the result of this thesis. However, the measured texture shows a solid pattern.

From a comparison of VPSC simulation results and experiments, as presented above, it is obvious that more comprehensive knowledge about the deformation mechanisms underlying the experiments of this work is required. Basal<a> slip may not be the primary slip mode needed to simulate these tests. However, there must be other mechanisms that should be taken into account to obtain a better simulation result.

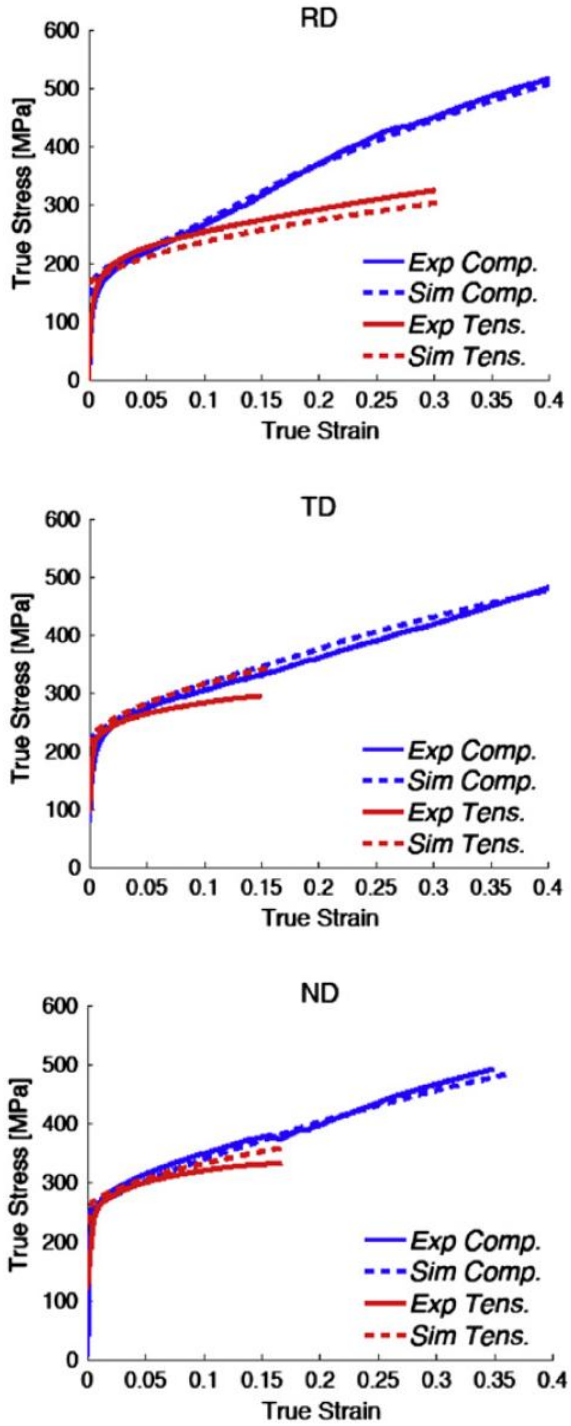

Figure 4.13. Comparison of simulated and measured true stress-true strain curves in different mechanical loading test of HP-Ti [Knezevic et al., 2013].

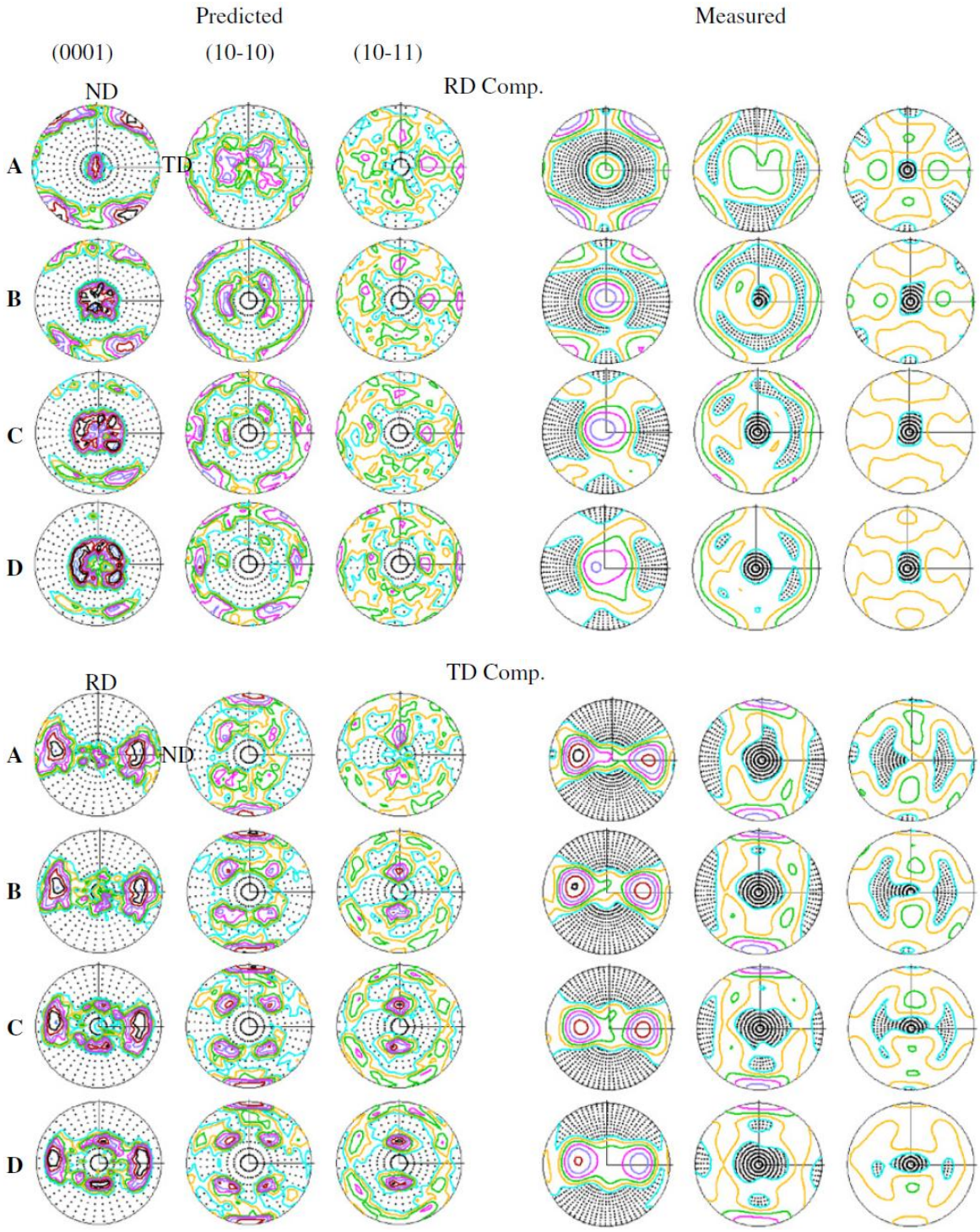
Predicted
Measured
(0001)
(10-10)
(10-11)
RD Comp.
ND
TD
A
B
C
D
TD Comp.
RD
ND
A
B
C
D

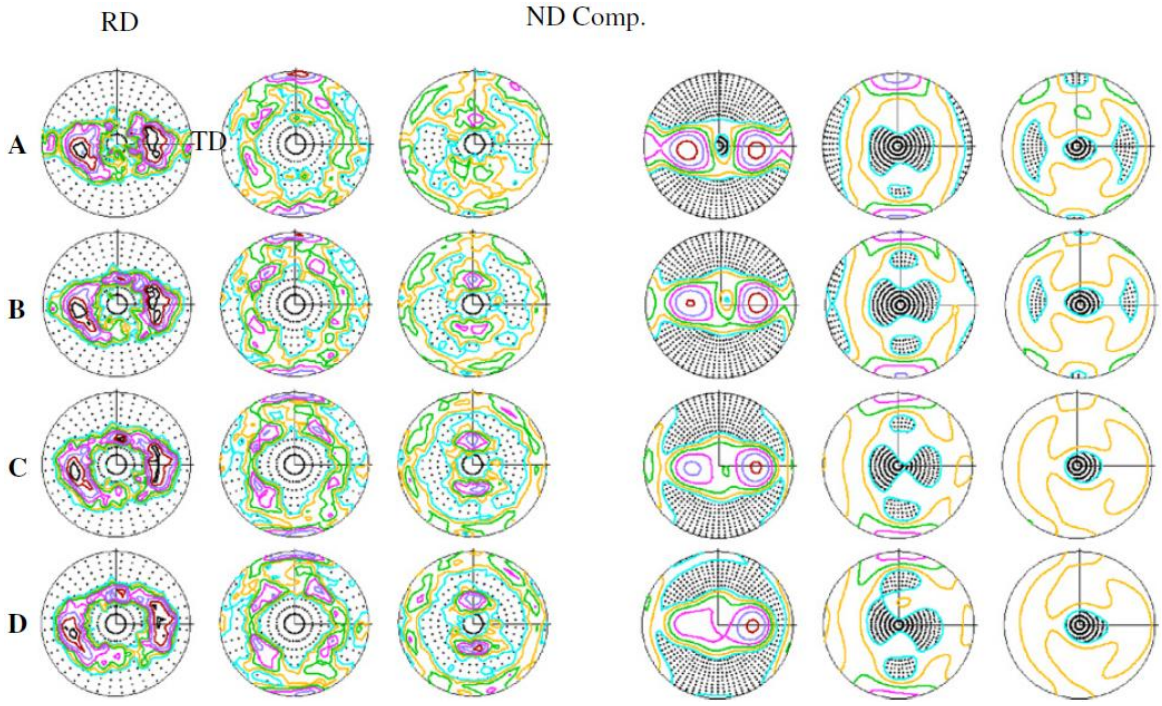

Figure 4.14. Comparison of simulated and measured texture evolution in 3 compression tests of HP-Ti; the letters on the left indicate the samples were deformed to true strains of (A)0.1,(B)0.2,(C)0.3, and (D)0.4 [Knezevic et al., 2013].

4.5 Summary

In this chapter, VPSC simulation on HP-Ti with a different texture from that in last chapter was carried out. Furthermore, different SC schemes in VPSC program have been applied individually for the comparison of their effects. All the SC schemes resulted in quite similar stress-strain predictions, which is different from the case in magnesium alloy [Wang et al., 2010a]. However, the relative activities of underlying deformation modes were easy to discriminate. The differences between SC schemes described in Wang et al. [Wang et al., 2010a] can be observed in the plot activities. This may indicate another unique characteristic of titanium. Nevertheless, further studies are still required, since the

rate sensitivity affects the difference between SC schemes. Evidence from simulation work applying higher value of "n" can provide more convincing conclusion.

A comparison between the simulated results with different numbers of deformation modes revealed the fact that basal <a> no longer serves as primary slip mode in polycrystal HP-Ti. In this thesis, simulation result showed that large amounts of basal<a> slips were activated. However, it was also discovered that the basal <a> mode could undermine the prediction of texture evolution. Both simulation works failed to capture all of the important features in measured texture. So the real mechanisms underlying the deformation of polycrystal titanium have not been entirely revealed yet.

Chapter 5 Simulation of Mechanical Behaviours of CP-Ti

5.1 Introduction

CP-Ti is a widely used material in the family of titanium alloys. Since CP-Ti has more applications than HP-Ti for its higher strength, many researchers have conducted different studies on this material including mechanical experiments and simulation. However, most of the simulation works are focused on specific studies, such as ECAP processing, uniaxial loading and shear tests. Only one type of experiments (such as uniaxial loading test) usually fails to describe the characteristics or anisotropy features of this HCP material. It also leads to difficulty in simulating this material and making a proper prediction for a wide variety of situations.

In this chapter, a VPSC simulation of comprehensive uniaxial loading tests and simple shear tests performed on CP-Ti [Benmhenni et al., 2013] will be presented. Along with the experiments, the Benmhenni et al. also carried out a VPSC simulation. Comparison between the two simulation works reveals the function of twinning mechanism in the simple shear deformation of CP-Ti.

5.2 Experimental Conditions

This series of mechanical tests in CP-Ti were conducted by N. Benmhenni et al. Specific details can be found in the literature [Benmhenni et al., 2013]. For completeness, all of the experimental data reported below including the experimental details of their work are reproduced below from their paper.

5.2.1 Material

The material studied in this chapter is CP-Ti, or T40 to be specific. The as-received thin sheet has 1.6 mm thickness and its chemical composition is given in Table 5.1. The initial texture of the material is shown in Figure 5.1. Compared with Figure 4.1, texture presented here resembles the one used in Chapter 4, only with a different chemical composition.

Table 5.1.
Chemical composition of T40 applied in this work (wt%).

C	H	O	N	Fe	Ti
0.003-0.005	0.017	0.12-0.14	0.005-0.006	0.005-0.008	Balance

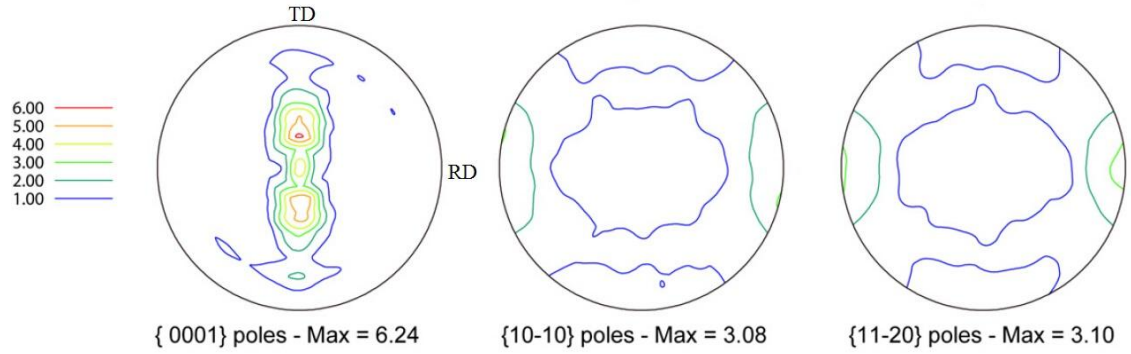

Figure 5.1. The Measured initial pole figure of CP-Ti in this work [Benmhenni et al., 2013].

5.2.2 Mechanical Testing

To reveal the anisotropy in mechanical behaviour of α-titanium, several monotonic simple shear tests along different directions in the plane of sheet as well as 6 uniaxial loading tests were performed at room temperature.

The geometry of the uniaxial loading specimens is shown in Figure 5.2. All the tests were performed at a constant strain-rate of $0.001s^{-1}$ and repeated three times at least to make sure the stability of experimental results. It is worth noting that, for compression tests, the dimensions of the samples are not ideal to reduce friction to minimum, due to the restriction from the initial size of as-received material.

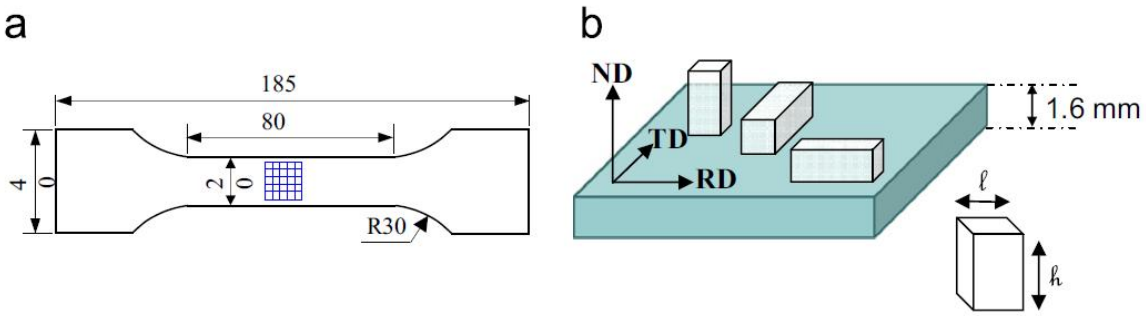

Figure 5.2. a) Geometry schematic of the tensile specimen and associated grid for measuring the strain. Dimensions are indicated in unit of mm. b) Geometry of the compressive specimen. l=3 mm and h=4 mm for RD and TD tests; l=2 mm and h=1.6 mm for ND test [Benmhenni et al., 2013].

Simple shear tests were performed at a constant von Mises equivalent strain-rate $0.001s^{-1}$ (shear strain $0.00173s^{-1}$). To ensure the accuracy of the strain measurement, a non contact video-extensometry was applied. The schematic of the specimen and the loading condition is shown in Figure 5.3. The photo of the simple shear device can be found in Fig. 1 of Bouvier et al. [Bouvier et al., 2006]. The shear specimen has a 30 mm length, 18 mm width and 1.6 mm thickness rectangular shape. The width of the gauge area is set as 2 mm according to related discovery on optimization of simple shear test [Bouvier et al., 2006]. Totally, three simple shear tests were run in this work with different angles equal to 0 °, 90 °and 135 °with respect to the RD direction in the normal plane.

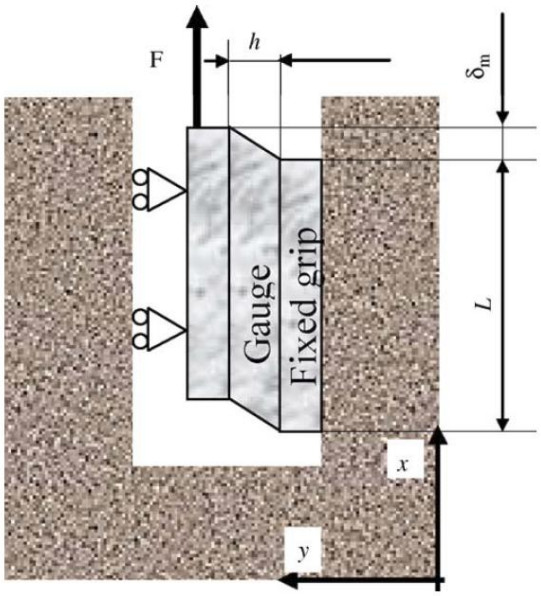

Figure 5.3. Schematic of the assembled simple shear sample and device. L and h are the length and width of the gauge area respectively, and δ_m stands for the displacement of two grips [Bouvier et al., 2006].

5.2.3 Deformation Mechanisms

The measured stress strain responses from the above experiments are shown in Figure 5.4. This figure is also reproduced with data extracted from the initial paper for a clear view. The anisotropy of CP-Ti shown in this work is very similar to that in HP-Ti from last chapter. This may due to the similarity of underlying textures in two materials and the purity only increases the yield strength level without changing the relationships between different rolling or loading directions. So, it is reasonable to believe that similar slip and twinning mechanisms are activated in this work. For the analysis of the experimental stress-strain responses of uniaxial loading tests, the readers are referred to Section 4.2.3.

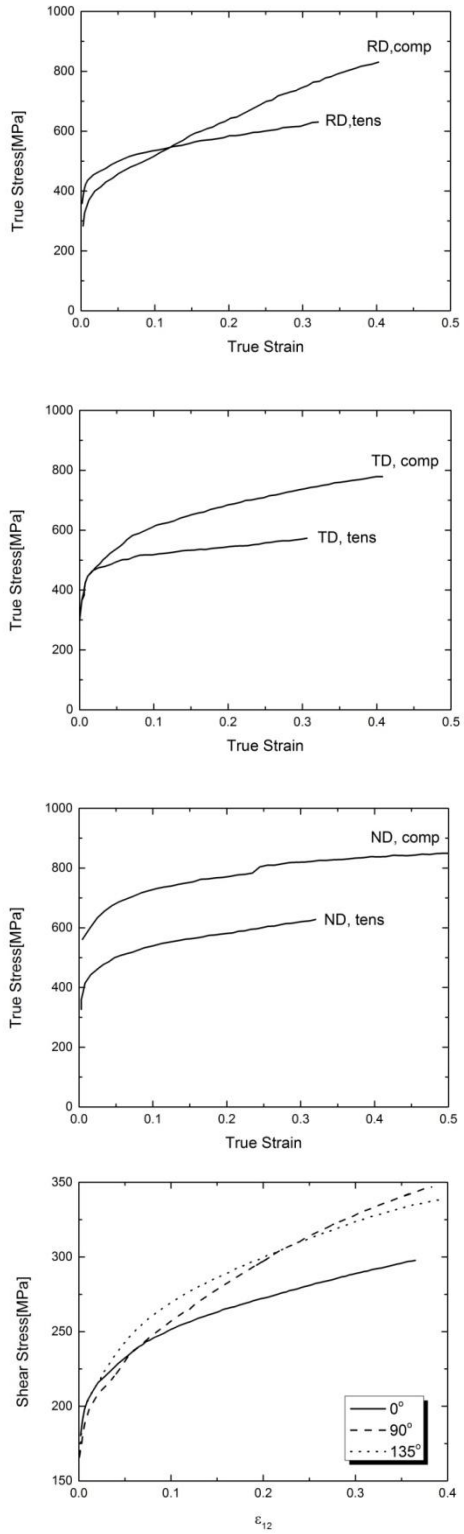

Figure 5.4. True stress-true strain responses of different tests on CP-Ti.

For the simple shear tests, the stress-strain responses have shown pronounced anisotropy as well. This may be an implicit indication that different mechanisms have been triggered in these tests. However, their experimental investigation [Bouvier et al., 2012] has indicated that very low amount of twins were present during all the tests, which will be discussed along with the simulation results of this thesis later.

5.3 Modelling Results and Discussion

The following part will present the numerical simulation done in this work, with simulation input conditions and calibration of parameters. A comparison of present VPSC simulations and those of the others will be presented in Section 5.4.

5.3.1 Simulation Input Conditions

For this simulation work, the "neff=10" SC scheme was selected for its better compatibility with different rate sensitivity and acceptable predicting ability shown in last chapter.

Since the initial texture of this work resembles the last one in the present work, the researcher chose to use the same numerical reproduction as initial input texture. It contains 500 different grains/orientations as representatives. The comparison between the measurement and reproduction is shown in Figure 5.5.

The loading conditions for tests in this work have already been discussed in former chapters. It is worth noting that different uniaxial loading directions can be described by different strain-rate tensors or Cauchy tensors, which has been mentioned before. As for different shear directions, the researcher chose to rotate the initial texture of the sample while holding the loading conditions as constant. So the textures were reoriented by 90 °

and 135 ° in corresponding test and the loading conditions for 0 ° were applied in three simple shear tests simulation (same as the one applied in simple shear test in Chapter 3).

a)

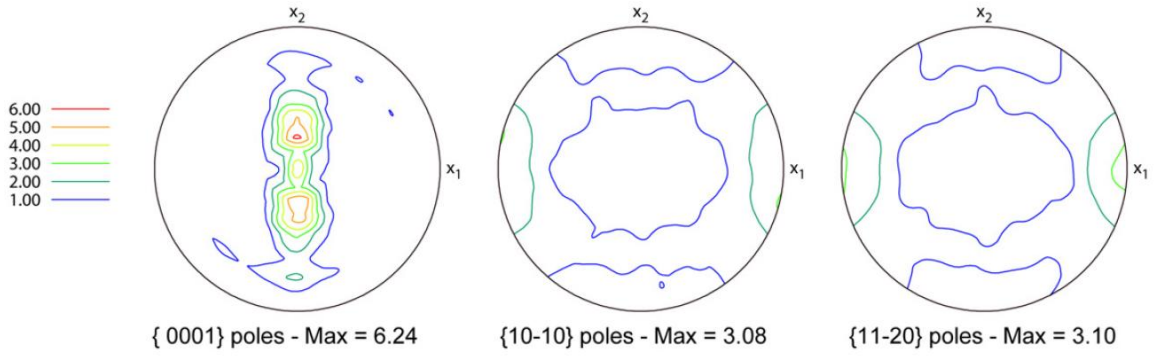

b)

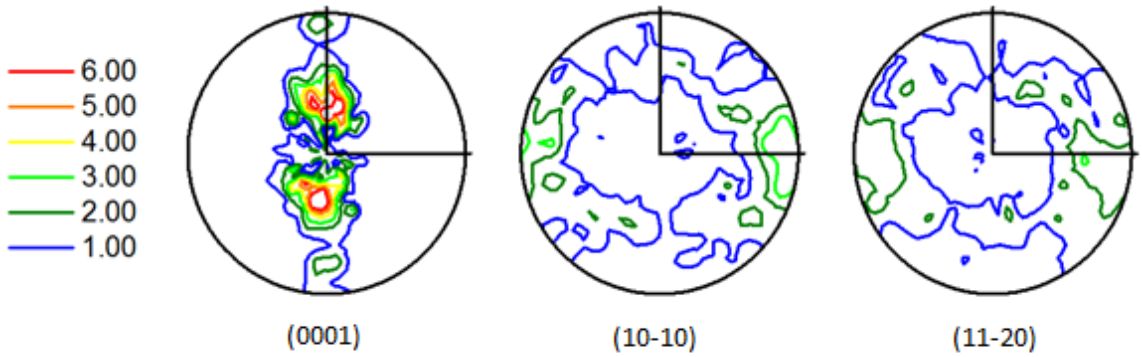

Figure 5.5. a) Measured initial texture in experiment from literature [Benmhenni et al., 2013]; b) Numerically reproduced initial texture. ($x_1$and x_2 indicate RD and TD directions).

In the constitutive equation, $\dot{\gamma}_o$, the reference slip rate, is set to a value of $0.001s^{-1}$ and rate sensitivity n=20. Voce hardening parameters can be found in Table 5.2. Since the similarity in initial textures, the researcher chose RD tension, RD compression and ND

compression to fit the stress-strain response and obtain the parameters, which is inspired by the work in Chapter 4. The remaining experimental data is used to evaluate the prediction, which consists of 6 different mechanical tests.

Table 5.2.
Voce hardening and PTR parameters for CP-Ti tests.

No. of s	Mode	τ_0	τ_1	θ_0	θ_1	h^{s1}	h^{s2}	h^{s3}	h^{s4}	A^{th1}	A^{th2}
1	Prismatic	120	30	500	60	1	1	1	3		
2	Basal	180	50	300	10	1	1	1	1		
3	Pyramidal<c+a>	380	50	2000	30	1	1	1	1		
4	Tensile twin	200	0	170	170	1	1	1	1	0.30	0.70

($h^{ss'}$ is the latent hardening parameter mentioned before, indicating the latent effect of system s' exerted on system s)

From the initial resistance of deformation modes represented by τ_0, it can be seen that almost all the slip/twinning modes are more difficult to be activated, compared with the hardening parameters of HP-Ti in last chapter. This is due to the fact that atoms of the solute in titanium alloy serve as obstacles for dislocations to slip and twinning to be activated. In this work, CRSS ratio Prismatic: Basal: Pyramidal: Tensile Twinning=1:1.15:3.17:1.67 is close to the parameters in HP-Ti for slip modes, which is 1:2.17:2.75:3. So the impurity of the material increases the resistance of slip modes proportionately. However, the significant difference lies in tensile twinning and the latent hardening effect appears to be weaker in this work. But the high hardening rate (represented by θ_0 and θ_1) of tensile twin still indicates strong impeding effect from the solute. It can lead to an indirect conclusion that the impurity affects the twinning activation in a different way from the slip modes. More specific underlying details require further studies.

5.3.2 Simulation Output Evaluation

Because of the similarity between this work and that in Chapter 4, the same procedure is followed here. It needs to be noted that there is not only one choice of combination of tests to fit the parameters. As long as each of the experiments can reveal the activation of one or two deformation modes (in ideal situation), then it is easy to determine the related parameters step by step. For example, 0 ℃RD simple shear test can replace the RD tension test to obtain parameters of prismatic mode, because prismatic mode dominates the deformation process in both of the tests. In another instance, twinning mode is greatly activated in RD compression. However, it is usually impossible to conduct a twinning dominated mechanical test. So one can determine the twinning parameters after the confirmation of slip parameters. This is the essential principle of the researcher during the fitting process and the options of fitting targets vary from different textures and materials.

The fitting stress-strain response is presented in Figure 5.6 with elastic deformation eliminated from the curves with the same method as that in former chapters (the Pearson correlations between the measured and simulated data are over 0.9931, which is determined by the ND compression result).

The activity plots in Figure 5.7 also show evidence supporting the author's former choice on these three tests to do the fitting. In RD tension test, prismatic slip mode dominates the deformation through all of the strain scale. Also, in ND compression, other slip modes replace prismatic mode and provide the information for determining their parameters. At last, twinning parameters can be obtained by RD compression, since in this test the volume fraction of twinning is much higher than in the other two.

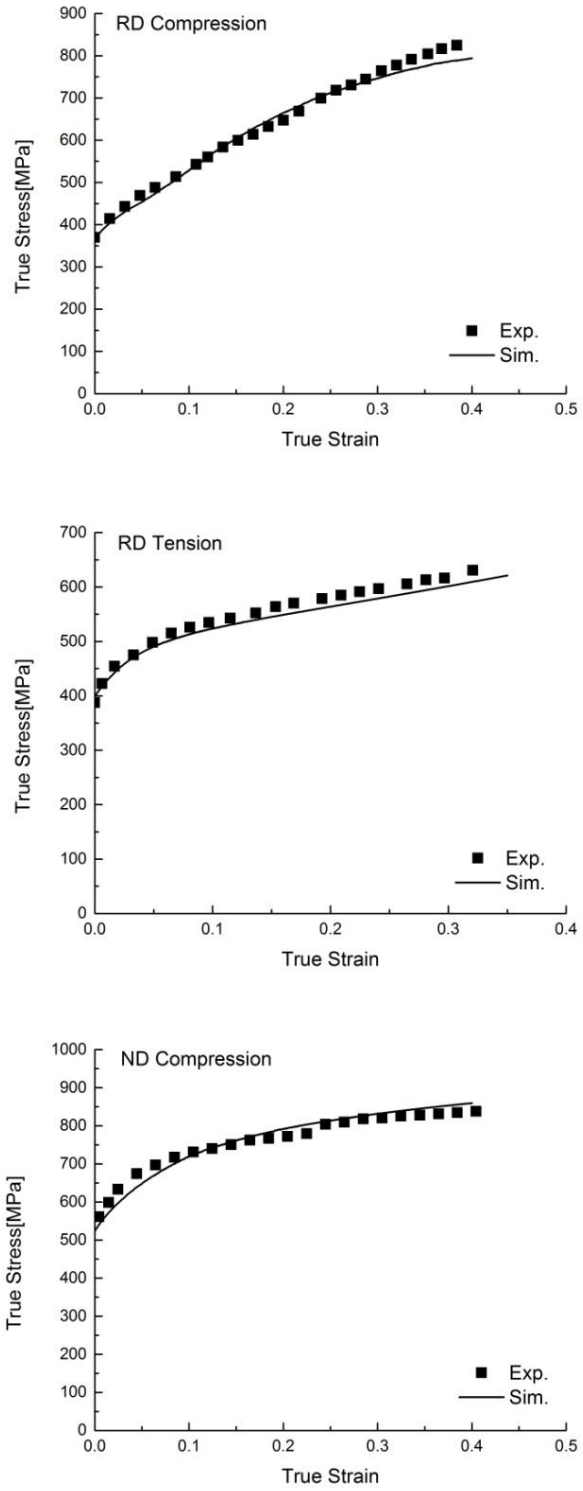

Figure 5.6. Comparison of fitted (Simulated) and experimentally measured true stress-true strain curves (plastic deformation) of 3 tests in CP-Ti [Benmhenni et al., 2013].

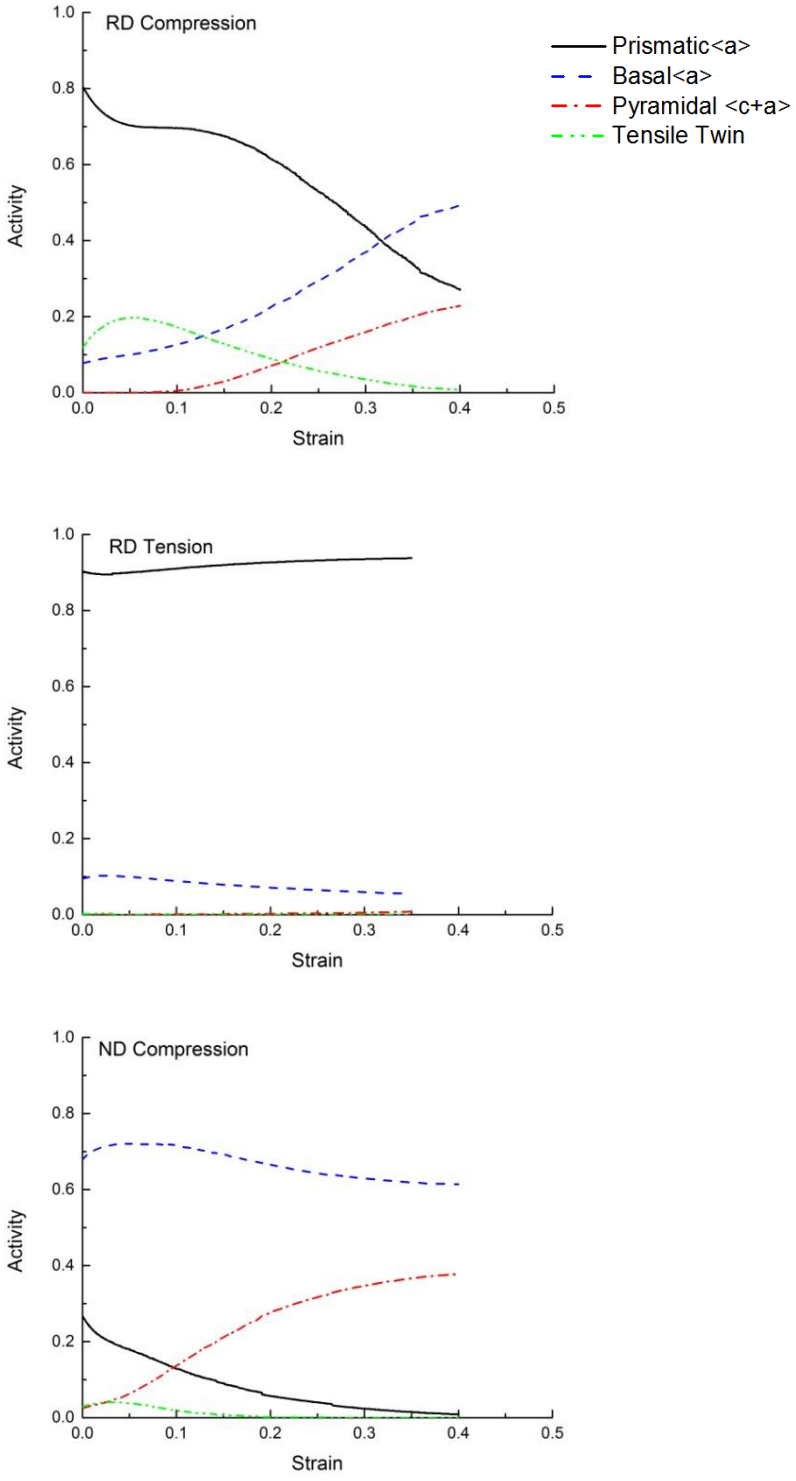

Figure 5.7. Relative activity of each deformation slip/twinning mode in 3 fitted mechanical loading tests in CP-Ti.

Figure 5.8 presents the other three uniaxial loading tests as predicted results (the Pearson correlations between the measured and simulated data are over 0.99336, which is determined by the TD tension result). There are some mismatches in the prediction of stresses at large strain level in TD tension test and lower predicted hardening rate in TD compression test. However, all these differences in stresses between prediction and measurement are approximately below 10%.

With the activity plot in Figure 5.9 and analysis of the underlying mechanisms in the three predicted tests, the reason for these mismatches can be found. In TD tension, the increasing activity of prismatic mode indicates that the hardening rate is mainly determined by prismatic slip at this time. Back to Table 5.2, the asymptotic hardening rate θ_1 of prismatic is apparently higher that the other two slip modes. However, prismatic slip mode also dominates the hardening rate in RD tension test, in which the fitted hardening rate is slightly lower than the measurement. So this is an inevitable error by choosing RD tension as fitting target and leaving TD tension for evaluation. For the mismatch in TD compression, a similar conclusion can be drawn by checking the activities of TD and RD compression tests as well. Basal slip mode plays an important role in hardening process in these two tests and the author believes that this prediction is the best balanced result.

The results for simple shear tests are shown in Figure 5.10 (the Pearson correlations between the measured and simulated data are over 0.99622, which is determined by the 0°RD simple shear test with the "poorest" simulated result) and Figure 5.11. Results of uniaxial loading tests simulation appears to be better than simple shear tests.

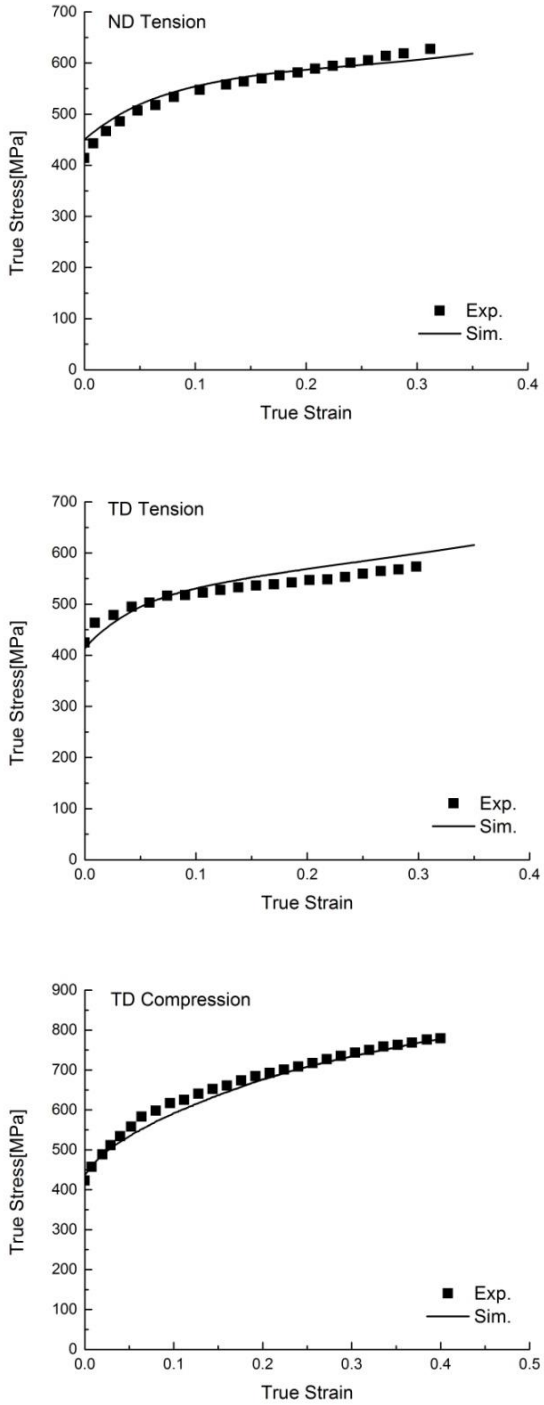

Figure 5.8. Comparison of predicted and measured stress-strain response of ND tension, TD tension and TD compression tests in CP-Ti [Benmhenni et al., 2013].

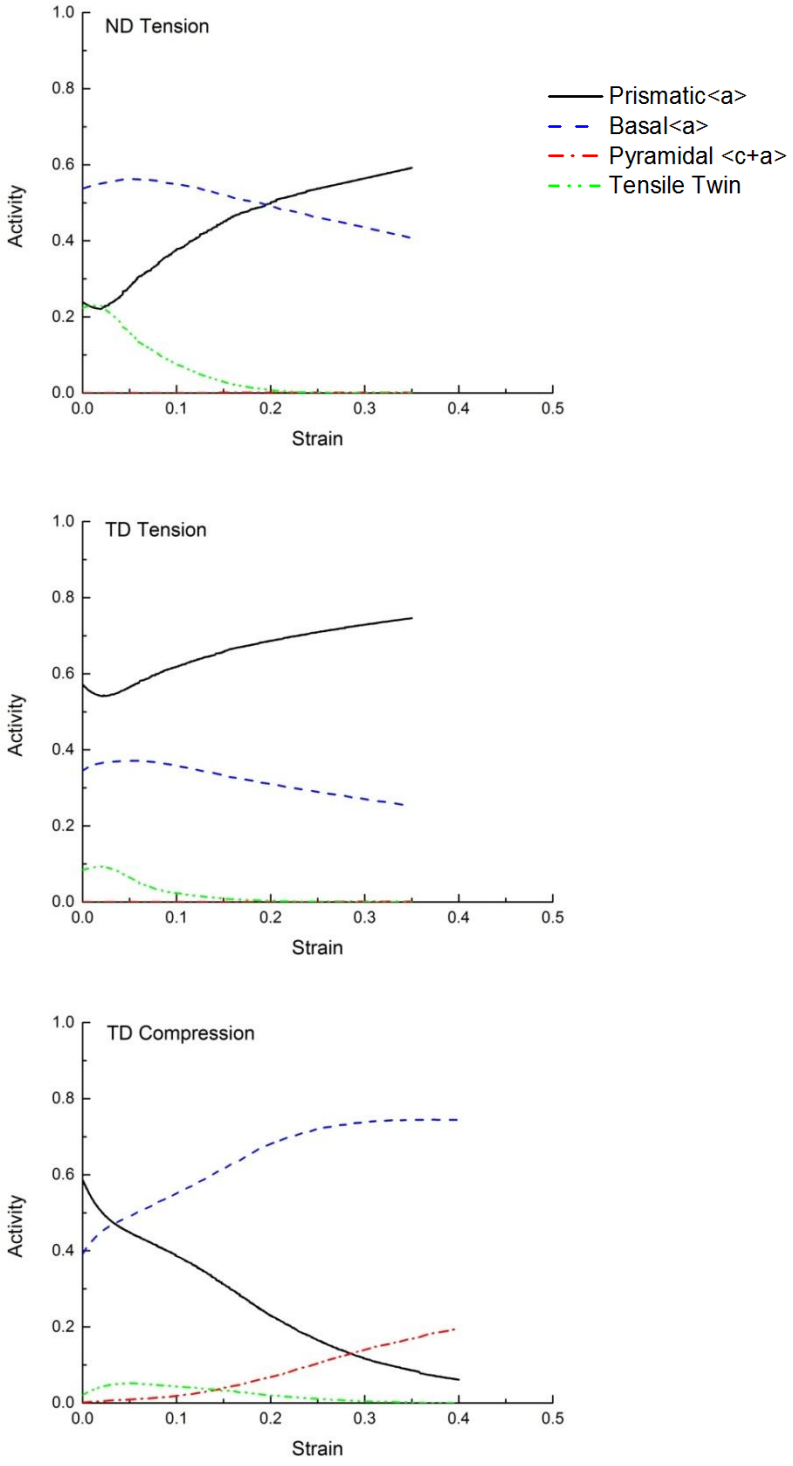

Figure 5.9. Relative activity of each deformation slip/twinning mode in 3 predicted uniaxial loading mechanical tests in CP-Ti.

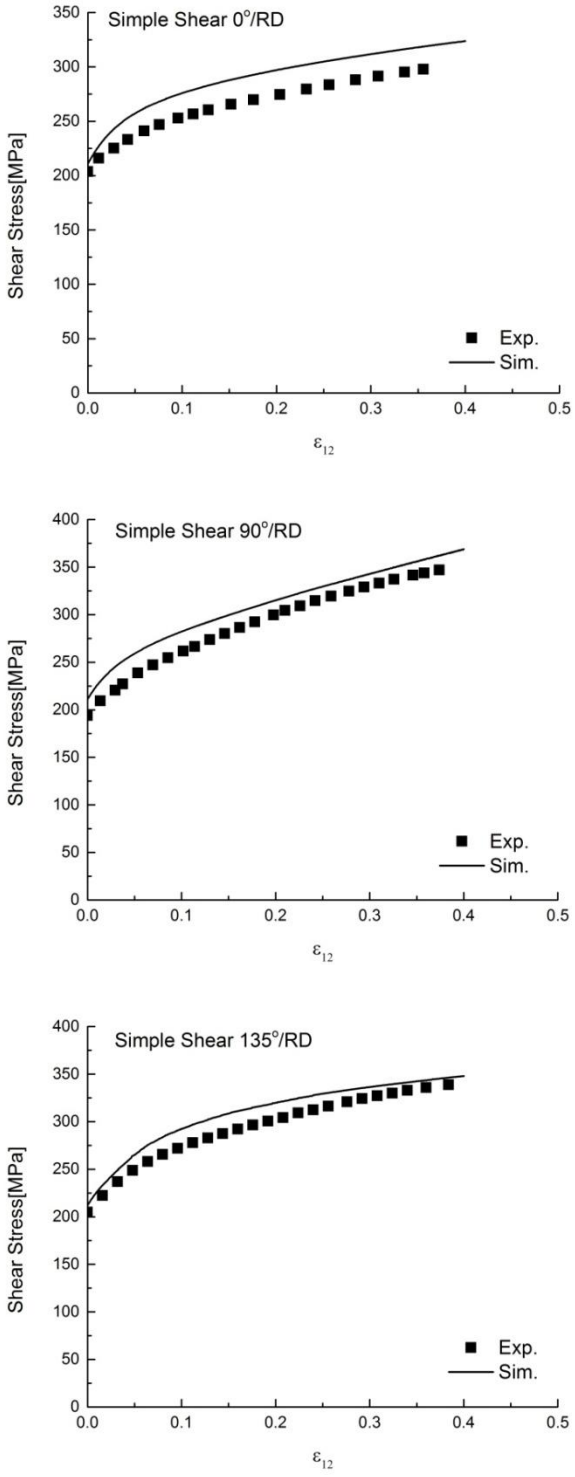

Figure 5.10. Comparison of predicted and measured stress-strain response of three simple shear tests in CP-Ti [Benmhenni et al., 2013].

However, the simple shear predicted curves still managed to reproduce the general shapes of the experimental curves and the initial yield stresses are well predicted too. As to the difference in hardening rate, it may be caused by the application of approximate initial texture. Moreover, it is not known as to how Benmhenni et al. obtained the specimens from the raw material sheet (which part of the sheet). Therefore, it is not known if the initial sample textures for simple shear tests and uniaxial loading tests are exactly the same, which may have an unexpected influence on the results. It also needs to be noted that Benmhenni et al. have already claimed that the specimens used in this work did not have the ideal dimensions intended for the tests, due to the restriction of the raw material size. In the present simulations of the experiments, the author found the ND tension experiment result may have significant error compared to other tension tests results, which may support the comments of Benmhenni et al.

Another reasonable speculation (perhaps not the only reason), for simple shear tests, is that there is an unavoidable problem undermining the accuracy of experimental results with the devices applied in this work. Though Benmhenni et al. has managed to minimize this negative effect by adapting the geometry of samples, the real shear stress at the centre of specimens is still at least 1% higher than the measured result [Bouvier et al., 2006].

Based on the activity plot, a conclusion can be drawn easily that the underlying mechanisms in 0 °RD and 90 °RD are similar and have almost the same relative activity. From the view of initial texture, these two loading directions are not symmetric to each other. However, the result of 135 °RD test shows a sign of twinning activation, which means slip modes have encountered larger obstacles due to this different loading direction.

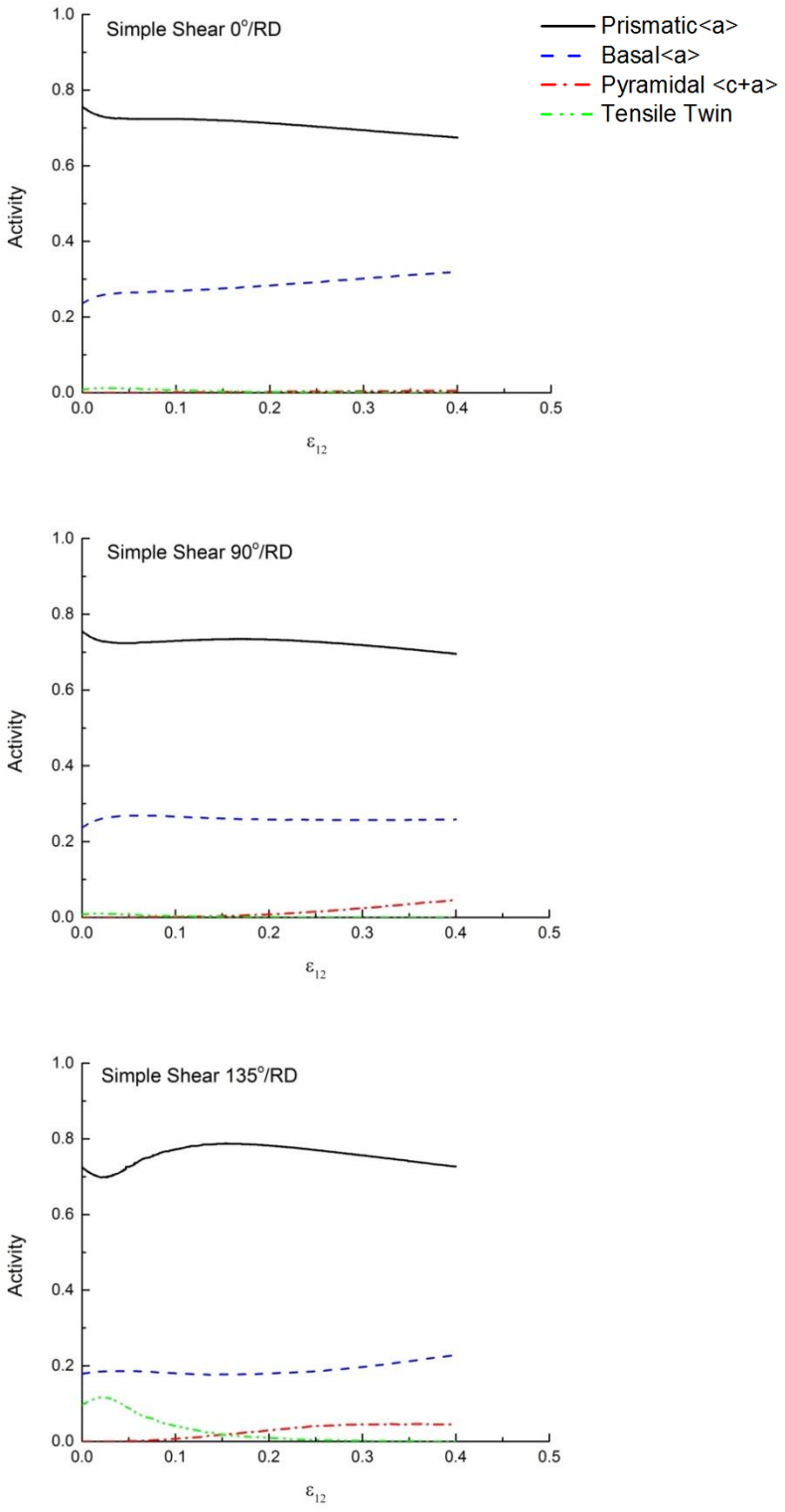

Figure 5.11. Relative activity of each deformation slip/twinning mode in 3 predicted simple shear tests in CP-Ti.

The textures of deformed samples are shown in Figure 5.12. The measured pole figure has also been rotated by an angle corresponding to the simulation. The predicted result of (0001) pole figures matches the measurement very well. The other two pole figures also have predicted the concentration of the orientations correctly, only with more intensity. This is a common phenomenon in simulation of simple shear tests shown in this thesis, which can also be observed in former chapters. The error in the prediction may be caused by the use of the PTR model is the VPSC simulations, because this model never changes the total orientations.

From the pole figures, it can be seen that the final textures of 0°RD and 90°RD tests are similar to each other. But 135°RD test shows a different type of pattern. It has been verified by conducting a trial without twinning mode that the difference is caused by the reorientation of tensile twin. Moreover, Benmhenni et al. conducted a simulation of their experiments with VPSC as well. The twinning mode was not taken into account in their program. The predicted result of 135°RD simple shear test shown in Benmhenni et al. [Benmhenni et al., 2013] presented an apparently different distribution from the measured texture (see Section 5.4). Therefore, twinning is a necessary deformation mode in this test, which is opposite to the opinion in the literature [Benmhenni et al., 2013].

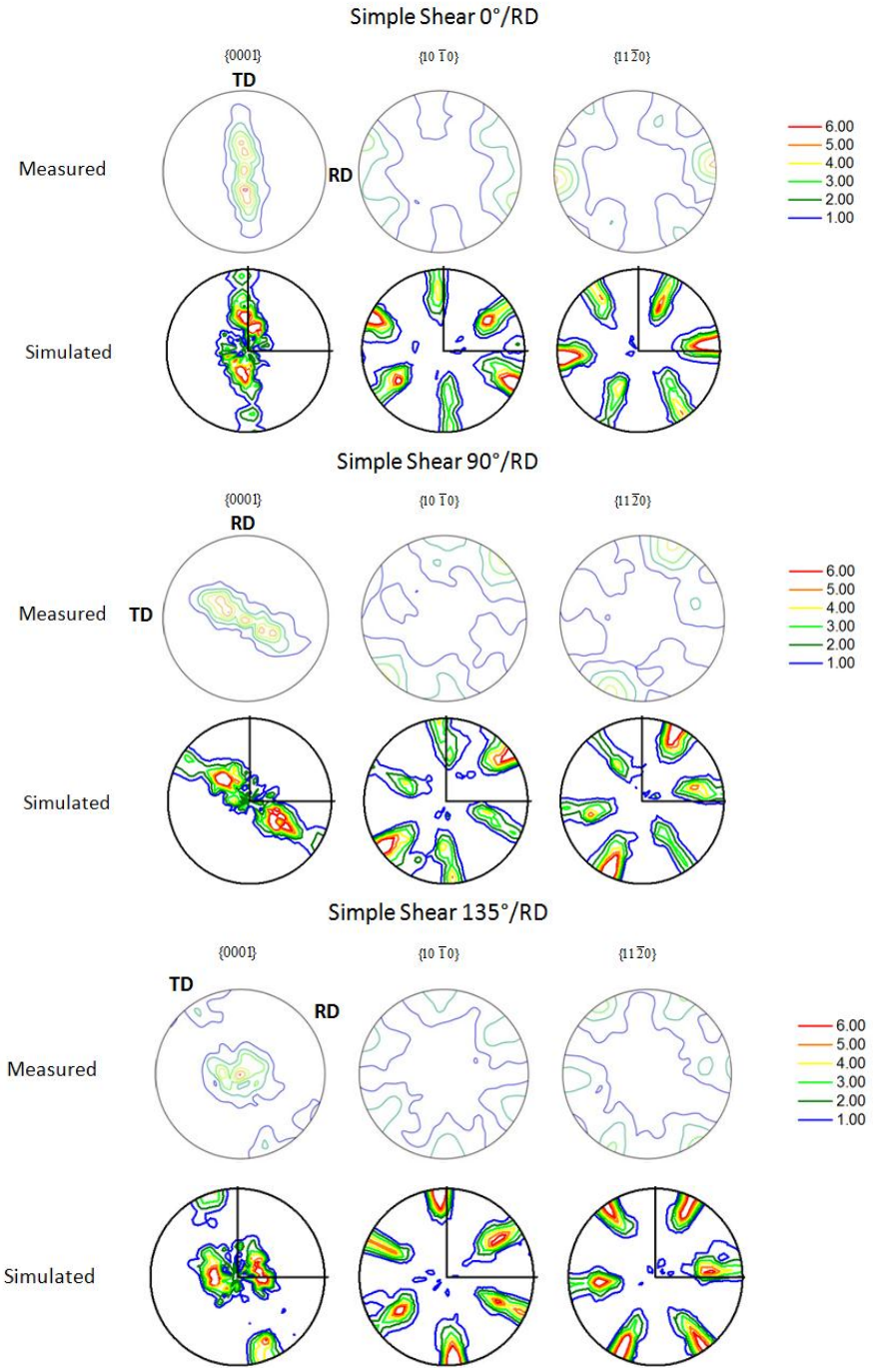

Figure 5.12. Comparison of simulated and measured textures [Benmhenni et al., 2013] at $\varepsilon = -0.4$ in three simple shear tests of CP-Ti (the same legend is applied to the simulated results).

5.4 Comparison of Results

In this section, the simulation result of Benmhenni et al. will be presented. Comparison between their results and the author's in this thesis will reveal the deformation mechanism of simple shear tests in this work [Benmhenni et al., 2013].

The fitted stress-strain curves of Benmhenni et al. are shown in Figure 5.13 (Fig. 6 in Benmhenni et al. [Benmhenni et al., 2013]). According to the former discussion (see Section 3.3.1 and Section 4.3.1) with regard to the selection of tests to fit the parameters, it can be anticipated that the choice of 3 simple shear tests undermines the accuracy of the final prediction in Benmhenni et al. [Benmhenni et al., 2013].

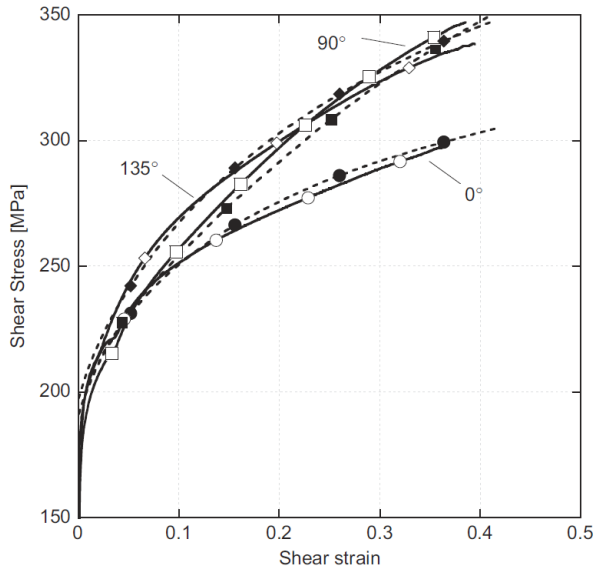

Figure 5.13. Comparison between simulated and measured stress-strain response of 3 simple shear tests in Benmhenni et al. [Benmhenni et al., 2013].

The predicted results of 3 compression tests in Benmhenni et al. [Benmhenni et al., 2013] are presented in Figure 5.14 (Fig. 12 in Benmhenni et al. [Benmhenni et al., 2013]).

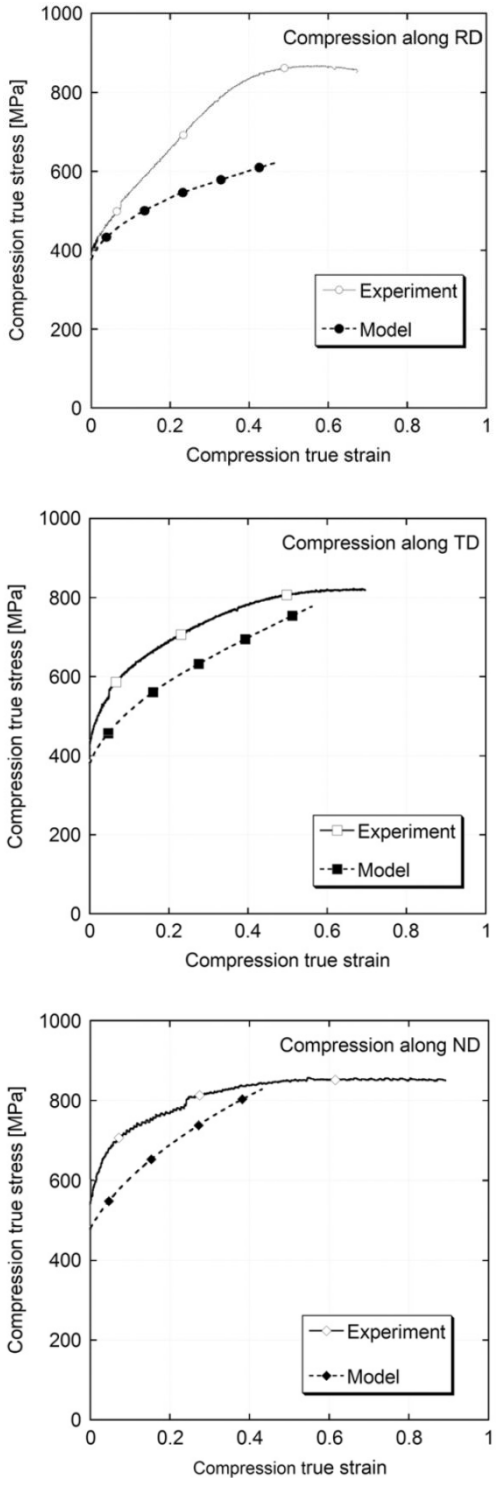

Figure 5.14. Comparison of simulated and measured stress-strain responses of 3 compression tests of CP-Ti in Benmhenni et al. [Benmhenni et al., 2013].

The results appear to be quite poor prediction compared with those of this thesis. This is due to the twinning mode which is not considered in the simulation of Benmhenni et al. [Benmhenni et al., 2013].

From the plot of activities (see Figure 5.7 and Figure 5.9), it can be seen that tensile twinning is activated in uniaxial loading tests with non-negligible volume fraction.

Figure 5.15 (Fig. 7 in Benmhenni et al. [Benmhenni et al., 2013]) shows the prediction of textures in simple shear tests of Benmhenni et al. [Benmhenni et al., 2013]. The results of 0 ℀RD and 90 ℀RD tests are similar to those of this thesis, which resemble the measurement. However, 135 ℀RD test result presented the simulated texture of this experiment without the twinning mode taken into account. It can be seen that the shape of the pattern is similar to those of the other two tests which have no twinning activated. With the comparison between the prediction of texture in Benmhenni et al. [Benmhenni et al., 2013] and that in this thesis, the conclusion that tensile twinning plays an essential role in the simple shear deformation of CP-Ti, can be drawn.

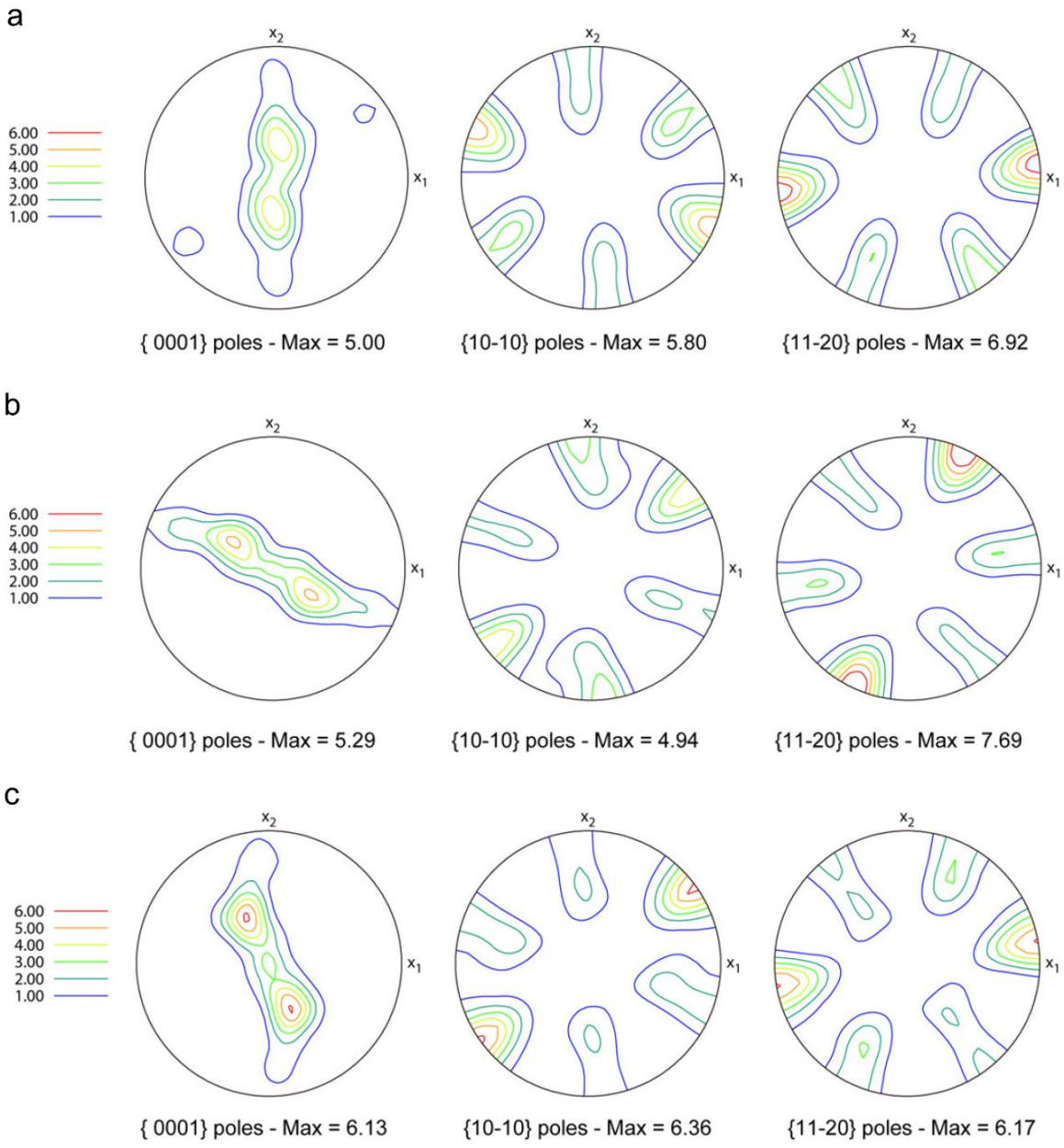

Figure 5.15. Predicted texture results of simple shear test along (a) 0 ºRD, (b) 90 ºRD and (c) 135 ºRD in Benmhenni et al. [Benmhenni et al., 2013] (the principle directions are the same as those in Figure 5.12).

5.5 Summary

In this chapter, a simulation work based on 9 mechanical tests has been carried out. The stress-strain response simulation generally matches the measurement. Except for the hardening rate, the yield strength and tendency of the curves both give good agreement with the experiments. Simulated results of both the stress-strain responses and the texture evolution in this thesis are closer to the experimental data than the simulated results of Benmhenni et al. [Benmhenni et al., 2013]. Moreover, the author of this thesis also proved that the tensile twinning is necessary in simple shear tests, which accounts for the failure of the texture simulation of Benmhenni et al. [Benmhenni et al., 2013].

Chapter 6 Conclusions

In this thesis, VPSC simulation on three groups of different experiments has been done. It has to be noted that this thesis is focused on plastic strain of titanium, since VPSC model provides no result of elastic deformation. Moreover, the "VPSC7a" code applied in this work cannot deal with the cases with rate sensitivity n>20, which needs to be improved in programming. The PTR model implemented in the code also undermines some of the results shown in this thesis, because PTR is only a simplified twinning model which can be replaced with advanced ones to obtain a better result. Still, several conclusions can be drawn after analyzing the work presented above:

1) VPSC method works well in simulating HP-Ti and CP-Ti, which can be proved by simulation works on two different textures of HP-Ti and one CP-Ti with 9 experiments. This method prevails on Taylor type models and leads to better simulated results of stress-strain responses.

2) In titanium material, different SC schemes result in quite similar simulation results of stress-strain responses with evidence in the simulation work of Chapter 4.

3) In polycrystal titanium, basal <a> is no longer a primary slip mode. Simulation with basal mode presents good stress-strain response prediction but much worse texture evolution. From the simulation activity plot, one can see basal slip plays important role in the predicted results. Therefore, the participation of basal slip in the deformation is doubtful.

4) In simple shear tests with different loading directions, tensile twin can be activated and serves as essential parts of the texture reorientation in some of the tests, depending on the

angle between the shear direction and textures. In this regard, the former conclusion in Benmhenni et al. [Benmhenni et al., 2013] is undermined by the results of this thesis.

Bibliography

Adib A. M. L., Baptista C. A. R. P., Barboza M. J. R., Haga C., and Marques C. C. F. Aircraft engine bleed system tubes: Material and failure mode analysis. *Engineering Failure Analysis*, Volume 14, Issue 8:1605-1617, 2007.

Agnew S. R., Tomé C. N., Brown D. W., Holden T. M., and Vogel S. C. Study of slip mechanisms in magnesium alloy by neutron diffraction and modeling. *Scr Mater, 48*, 1003–1008, 2003.

Akhtar A. Basal slip and twinning in *α*-titanium single crystals. *Metall Trans A, 6A*, 1105–1113, 1975.

Akhtar A., Teghtsoonian E. Prismatic slip in α-titanium single crystals. *Metall Trans A, 6A*, 2201–2208, 1975.

Armstrong R., Codd I., Douthwaite R. M., and Petch N. J. The plastic deformation of polycrystalline aggregates. *Philos Mag A, 7*, 45–58, 1961.

Asgari S., El-Danaf E., Kalidindi S. R., and Doherty R. D. Strain hardening regimes and microstructural evolution during large strain compression of low stacking fault energy fcc alloys that form deformation twins. *Metall and Mater Trans A, 28A*, 1781-1795, 1997.

Balasubramanian S., Anand L. Plasticity of initially textured hexagonal polycrystals at high homologous temperatures: application to titanium. *Acta Mater, 50*, 133–148, 2002.

Battaini M., Deformation Behaviour and Twinning Mechanisms of Commercially Pure Titanium Alloys. *Ph. D. Thesis.*Monash University: Department of Materials Engineering, 2008.

Beaudoin A. J., Dawson P. R., Mathur K. K., Kocks U. F., and Korsekwa D. A. Application of polycrystal plasticity to sheet forming. *Comput Methods Appl Mech Eng, 117*, 49–70, 1994.

Bell R. L., Cahn R. W. The nucleation problem in deformation twinning. *Acta Metall, 1* (6), 752–753, 1953.

Benmhenni N., Bouvier S., Brenner R., Chauveau T., and Bacroix B. Micromechanical modeling of monotonic loading of CP α-Ti: Correlation between macroscopic and microscopic behavior. *Materials Science & Engineering A, 573*, 222-233, 2013.

Bishop J. F. W., Hill R. A theoretical derivation of the plastic properties of polycrystalline face-centred metal. *Philos Mag, 42* (334), 1298–1307, 1951a.

Bishop J. F. W., Hill R. A theory of the plastic distortion of polycrystalline aggregate under combined stresses. *Philos Mag, 42* (327), 414–427, 1951b.

Bouvier S., Haddadi H., Levée P., and Teodosiu C. Simple shear tests: Experimental techniques and characterization of the plastic anisotropy of rolled sheets at large strains. *Journal of Materials Processing Technology, 172*, 96-103, 2006.

Bouvier S., Benmhenni N., Tirry W., Gregory F., Nixon M. E., Cazacu O., and Rabet L. Hardening in relation with microstructure evolution of high purity α-titanium deformed under monotonic and cyclic simple shear loadings at room temperature. *Mater Sci Eng A, 535*, 12-21, 2012.

Braisaz T., Ruterana P., Nouet G., Serra A., Komninou P., Kehagias T., and Karakostas T. High-resolution electron microscopy study of the $(10\bar{1}2)$ twin and defects analysis in deformed polycrystalline _-titanium. *Philos Mag Lett*, *74* (5), 331–338, 1996.

Calnan E. A., Clews C. J. B. The development of deformation textures in metals - Part III. Hexagonal structures. *Philos Mag*, *42*, 919–931, 1951.

Canova G. R. Self-consistent methods: application to the prediction of the deformation texture of polyphase materials. *Mater Sci Eng A, 175*, 37–42, 1994.

Cass T. R. Slip modes and dislocation substructures in titanium and titanium-aluminium single crystals. In Jaffee, R. & Promisel, N. (Eds.), *The Science, Technology and Application of Titanium*, (pp. 459–477). Pergamon Press, 1968.

Cheneau-Späth N., Driver J. H. Plane strain compression of titanium crystals. *Mater Sci Forum*, *157-162*, 639–644, 1994.

Chichili D. R., Ramesh K. T., and Hemker K. J. The high-strain-rate response of alpha-titanium: experiments, deformation mechanisms and modeling. *Acta Mater*, *46* (3), 1025–1043, 1998.

Chin G. Y., Mammel W. L. Computer solutions of the Taylor analysis for axisymmetric flow. *Trans Met Soc AIME*, *239* (9), 1400–1405, 1967.

Chin G. Y., Mammel W. L., and Dolan M. T. Taylor's theory of texture for axisymmetric flow in body-centered cubic metals. *Trans Met Soc AIME, 239* (11), 1854–1855, 1967.

Christian J. W., Mahajan S. Deformation twinning. *Prog Mater Sci*, *39*, 1–157, 1995.

Churchman A. T. The slip modes of titanium and the effect of purity on their occurrence during tensile deformation of single crystals. *Proc R Soc Lond A, 226* (1165), 216–226, 1954.

Conrad H. Effect of interstitial solutes on the strength and ductility of titanium. *Prog Mater Sci*, *26*, 123–403, 1981.

Döner M., Conrad H. Deformation mechanisms in commercial Ti- 50A (0.5 at. pct O_{eq}) at intermediate and high temperatures ($0.3\text{-}0.6T_m$). *Metall Trans*, *4*, 2809–2817. 1973.

Dragomir I. C., Li D. S., Castello-Branco G. A., Garmetstam H., Suyder R. L., Ribarik G., and Ungar T. Evolution of dislocation density and character in hot rolled titanium determined by X-ray diffraction. *Mater Charact*, *55* (1), 66–74, 2005.

Emsley, John. Titanium. *Nature's Building Blocks: An A-Z Guide to the Elements*. Oxford, England, UK: Oxford University Press, 2001.

Farenc S., Caillard D., and Couret A. An *in situ* study of prismatic glide in *α* titanium at low temperatures. *Acta Metall Mater*, *41* (9), 2701–2709, 1993.

Fundenberger J. J., Philippe M. J., Wagner F., and Esling C. Modelling and prediction of mechanical properties for materials with hexagonal symmetry (zinc, titanium and zirconium alloys). *Acta Mater*, *45* (10), 4041–4055, 1997.

Garde A. M., Santhanam A. T., and Reed-Hill R. E. The significance of dynamic strain aging in titanium. *Acta Metall*, *20* (2), 215–220, 1972.

Garde A. M., Aigeltinger E., and Reed-Hill R. E. Relationship between deformation twinning and the stress-strain behavior of polycrystalline titanium and zirconium at 77K. *Metall Trans, 4*, 2461–2468, 1973.

Glavicic M. G., Salem A. A., and Semiatin S. L. X-ray line-broadening analysis of deformation mechanisms during rolling of commercial-purity titanium. *Acta Mater, 52*, 647–655, 2004.

Gray III G. T. Influence of strain rate and temperature on the structure, property behavior of high purity titanium. *J Phy IV JP, C3*, 423–428, 1997.

Hill R. Continuum micro-mechanics of elastoplastic polycrystals. *J Mech Phys Solids, 13*, 89–101, 1965.

Hill R. The essential structure of constitutive laws for metal composites and polycrystals. *J Mech Phys Solids, 15* (2), 79–95, 1967.

Hosford W. F. *The Mechanics of Crystals and Textured Polycrystals*. Oxford University Press, 1993.

Huang W., Zan X., Nie X., Gong M., Wang Y., and Xia Y. Experimental study on the dynamic tensile behavior of a poly-crystal pure titanium at elevated temperatures. *Mater Sci Eng A, 443* (1-2), 33–41, 2007.

Hutchinson J. W. Bounds and self-consistent estimates for creep of polycrystalline materials. *Proc R Soc London, A 348*, 101-121, 1976.

Hutchinson W. B. Elastic-plastic behaviour of polycrystalline metals and composites. *Proc R Soc Lond A, 319* (1537), 247–272, 1970.

Jones I. P., Hutchinson W. B. Stress-state dependence of slip in titanium-6Al-4V and other h.c.p. metals. *Acta Metall, 29*, 951–968, 1981.

Kalidindi S. R., Bronkhorst C. A., and Anand, L. Crystallographic texture evolution in bulk deformation processsing of FCC metals. *J Mech Phys Solids, 40* (3), 537–569, 1992.

Kalidindi S. R. Incorporation of deformation twinning in crystal plasticity models. *J Mech Phys Solids*, 46, 267, 1998.

Kalidindi S. R. Modeling anisotropic strain hardening and deformation textures in low stacking fault energy fcc metals. *Int J Plast, 17*, 837–860, 2001.

Kalidindi S. R., Salem A. A., and Doherty R. D.. Role of deformation twinning on strain hardening in cubic and hexagonal polycrystalline metals. *Adv Eng Mater, 5* (4), 229–232, 2003.

Kaschner G. C., Lovato M. L., Stout M. G., Proust G., Liu C., Beyerlein I. J., Usov I., Wang Y., and Tomé C. N. Mini-Tensile Experiments of Clock-Rolled Zirconium Plate. *Experimental Mechanics, 50*, 65-70, 2010.

Kim I., Kim J., Shin D. H., Liao X. Z., and Zhu Y. T. Deformation twins in pure titanium processed by equal channel angular pressing. *Scr Mater, 48*, 813–817, 2003.

Knezevic M., Lebensohn R. A., Cazacu O., Revil-Baudard B., Proust G., Vogel S. C., and Nixon M. E. Modeling bending of α-titanium with embedded polycrystal plasticity in implicit finite elements. *Materials Science & Engineering A, 564*, 116-126, 2013.

Kocks U. F., Chandra C. H. Slip geometry in partially contrained deformation. *Acta Metall, 30*, 695–709, 1982.

Kocks U. F., Tomé C. N., and Wenk H.-R. *Texture and Anisotropy: Preferred Orientations in Polycrystals and their Effect on Materials Properties*. Cambridge: Cambridge University Press, 1998.

Lebensohn R. A., Tomé C. N. A self-consistent anisotropic approach for the simulation of plastic deformation and texture development of polycrystals - Application to zirconium alloys. *Acta Metall Mater, 41 (1993)*, 2611-2624, 1993.

Lebensohn R. A., Solas D., Canova G. R., and Brechet Y. Modelling damage of Al-Zn-Mg alloys. *Acta Mater, 44*, 315-325, 1996.

Lebensohn R. A., Canova G. R. A self-consistent approach for modelling texture development of two-phase polycrystals: application to titanium alloys. *Acta Mater, 45* (9), 3687–3694, 1997.

Lebensohn R. A., Turner P. A., and Canova G. R. Recent advances in modelling polycrystals with complex microstructures. *Comput Mater Sci, 9*, 229–236, 1997.

Lebensohn R. A., Tomé C. N., and Maudlin P. J. An extended self-consistent visco-plastic formulation: application to polycrystals with voids. *Int Report of Los Alamos Nat. Lab* LA-UR-03-1193, 2003.

Lebensohn R. A., Tomé C. N., and Maudlin P. J. A selfconsistent formulation for the prediction of the anisotropic behavior of viscoplastic polycrystals with voids. *J Mech Phys Solids, 52*, 249-278, 2004.

Legrand B. Structure du coeur des dislocations vis $1/3< 11\bar{2}0 >$dans le titane. *Philos Mag A, 52* (1), 83 – 97, 1985.

Liu X., Chu P. K., and Ding C. Surface modification of titanium, titanium alloys, and related materials for biomedical applications. *Materials Science and Engineering*, R: Reports, Volume 47, Issues 3-4:49_121, 2004.

Lütjering G., Williams J. C. *Titanium*. 2nd edition. Berlin: Springer-Verlag, 2007.

MacEwen S. R., Tomé C. N., and Faber Jr J. Residual stresses in annealed zircaloy. *Acta Metall, 37* (3), 979–989, 1989.

Marin E. B., Dawson P. R. Elastoplastic finite element analyses of metal deformations using polycrystal constitutive models. *Comput Methods Appl Mech Eng, 165* (1-4), 23–41, 1998.

Masson R., Bornert M., Suquet P., and Zaoui A. An affine formulation for the prediction of the effective properties of nonlinear composites and polycrystals. *J Mech Phys Solids, 48*, 1203-1227, 2000.

McHargue G. J., Hammond, J. P. Deformation mechanisms in titanium at elevated temperatures. *Acta Metall, 1*, 700–705, 1953.

Medina Perilla J. A., Gil Sevillano J. Two-dimensional sections of the yield locus of a Ti-6alloy with a strong transverse-type crystallographicatexture. *Mater Sci Eng A, 201*, 103–110, 1995.

Minonishi Y., Ishioka S., Koiwa M., Morozumi S., and Yamaguchi M. The core structure of a $\frac{1}{3} < \bar{1}\bar{1}23 >$ screw dislocation in h.c.p. metals. *Philos Mag A, 44* (6), 1225 – 1237, 1981.

Minonishi Y., Morozumi S., and Yoshinaga H. $\{11\bar{2}2\} < \bar{1}\bar{1}23 >$ slip in titanium. *Scr Metall, 16*, 427–430, 1982a.

Minonishi Y., Ishioka S., Koiwa M., and Morozumi S. Motion of a $\frac{1}{3} < \bar{1}\bar{1}23 >$ screw dislocation in a model h.c.p. lattice. *Philos Mag A*, *46* (5), 761 –770, 1982b.

Minonishi Y., Ishioka S., Koiwa M., Morozumi S., and Yamaguchi M. The core structures of a $\frac{1}{3} < \bar{1}\bar{1}23 > \{11\bar{2}2\}$ edge dislocation under applied shear stresses in an h.c.p. model crystal. *Philos Mag A*, *45* (5), 835 – 850, 1982c.

Minonishi Y., Morozumi S., and Yoshinaga H. Accomodation around $< 10\bar{1}1 >$ twins in titanium. *Scr Metall*, *19*, 1241–1245, 1985.

Mullins S., Patchett B. M. Deformation microstructure in titanium sheet metal. *Metall Mater Trans A*, *12A*, 853–863, 1981.

Murayama Y., Obara K., and Ikeda K. Effect of twinning on the deformation behavior of textured sheets of pure titanium in uniaxial test. *Mater Trans , JIM*, *28* (7), 564–578, 1987.

Murayama Y., Obara K., and Ikeda K. Effects of deformation twinning on the deformation behavior of textured titanium sheets in plane strain compression tests. *Mater Trans , JIM*, *33* (9), 854–861, 1991.

Myagchilov S., Dawson P. R. Evolution of texture in aggregates of crystals exhibiting both slip and twinning. *Modell Simul Mater Sci Eng*, *7*, 975–1004, 1999.

Naka S., Lasalmonie A., Costa P., and Kubin L. P. The low-temperature plastic deformation of α-titanium and the core structure of a-type screw dislocation. *Philos Mag A*, *57* (5), 717–740, 1988.

Naka S., Kubin L. P., and Perrier C. The plasticity of titanium at low and medium temperatures. *Philos Mag A*, *63* (5), 1035–1043, 1991.

Nemat-Nasser S., Guo W. G., and Cheng J. Y. Mechanical properties and deformation of commercially pure titanium. *Acta Mater*, *47* (13), 3705–3720, 1999.

Nixon M. E., Cazacu O., and Lebensohn R. A. Anisotropic response of high-purity α-titanium: Experimental characterization and constitutive modeling. *Int J Plast*, *26*, 516-532, 2010.

Numakura H., Minonishi Y., and Koiwa M. $< \bar{1}\bar{1}23 > \{10\bar{1}1\}$ slip in titanium polycrystals at room temperature. *Scr Metall*, *20*, 1581–1586, 1986.

Partridge P. G. The Crystallography and Deformation Modes of Hexagonal Close-Packed Metals. *Metallurgical Reviews* 118, 1967.

Paton N. E., Backofen W. A. Plastic deformation of titanium at elevated temperatures. *Metall Trans*, *1*, 2839–2847, 1970.

Philippe M. J., Serghat M., Van Houtte P., and Esling C. Modelling of texture evolution for materials of hexagonal symmetry - II. Application to zirconium and titanium *α* or near *α* alloys. *Acta Metall Mater*, *43* (4), 1619–1630, 1995.

Philippe M. J., Bouzy E., and Fundenberger J. J. Textures and anistropy of titanium alloys. *Mater Sci Forum*, *273-275*, 511–522, 1998.

Pochettino A. A., Gannio N., Vial Edwards C., and Penelle R. Texture and pyramidal slip in Ti, Zr and their alloys. *Scr Metall Mater*, *27*, 1859–1863, 1992.

Proust G., Tomé C. N., and Kaschner G. C. Modeling texture, twinning and hardening evolution during deformation of hexagonal materials. *Acta Mater*, *55* (6), 2137–2148, 2007.

Proust G., Tomé C. N., Jain A., and Agnew S. R. Modeling the effect of twinning and detwinning during strain-path changes of magnesium alloy AZ31. *Int. J. Plasticity, 25*, 861-880, 2009.

Rack H. J., Qazi J. I. Titanium alloys for biomedical applications. *Materials Science and Engineering C*, Volume 26, Issue 8:1269-1277, 2006.

Rosi F. D., Dube C. A., and Alexander B. H. Mechanism of plastic flow in titanium - determination of slip and twinning elements. *Trans Met Soc AIME, 5* (2), 257–265, 1953.

Rosi F. D. Mechanism of plastic flow in titanium: manifestations and dynamics of glide. *J Met, 6* (1), 58–69, 1954.

Rosi F. D., Perkins F. C., and Seigle L. L. Mechanism of plastic flow in titanium at low and high temperatures. *Trans Met Soc AIME, 8* (2), 115–122, 1956.

Salem A. A., Kalidindi S. R., and Doherty R. D. Strain hardening regimes and microstructure evolution during large strain compression of high purity titanium. *Scr Mater, 46*, 419–423, 2002.

Salem A. A., Kalidindi S. R., and Doherty R. D. Strain hardening of titanium: role of deformation twinning. *Acta Mater, 51*, 4225–4237, 2003a.

Salem A. A., Kalidindi S. R., Doherty R. D., Glavicic M. G., and Semiatin S. L. Effect of texture and deformation temperature on the strain hardening response of polycrystalline α-titanium. In Lutjering, G. & Albrecht, J. (Eds.), *Ti-2003: science and technology*, (pp. 1429–1436)., Hamburg, Germany. Wiley, 2003b.

Salem A. A., Kalidindi S. R., and Semiatin S. L. Strain hardening due to deformation twinning in α-titanium: constitutive relations and crystal plasticity modeling. *Acta Mater, 53*, 3495–3502, 2005.

Salem A. A., Kalidindi S. R., Doherty R. D., and Semiatin S. L. Strain hardening due to deformation twinning in α-titanium: mechanisms. *Metall Mater Trans A, 37A*(1), 259–268, 2006.

Santhanam A. T., Reed-Hill R. E. The influence of strain rate dependent work hardening on the necking strain in α-titanium at elevated temperatures. *Metall Trans, 2*, 2619–2622, 1971.

Serra A., Bacon D. J. A new model for $\{10\bar{1}2\}$ twin growth in hcp metals. *Philos Mag A, 73* (2), 333–343, 1996.

Shechtman D., Brandon D. G. Orientation dependent slip in polycrystalline titanium. *J Mater Sci, 8* (9), 1233–1237, 1973.

Smirnov A. R., Moskalenko V. A. Correlation between substructure and mechanical properties of α-Ti at varying deformation temperatures 4.2-373 K. *Mater Sci Eng A, 327* (2), 138–143, 2002.

Solas D. E., Tomé C. N. Texture and strain localization prediction using a N-site polycrystal model. *Int J Plast, 17* (5), 737–753, 2001.

Song S. G., Gray III G. T. Influence of temperature and strain rate on slip and twinning behavior of Zr. *Metall Mater Trans A, 26A*(10), 2665–2675, 1995a.

Song S. G., Gray III G. T. Structural interpretation of the nucleation and growth of deformation twins in Zr and Ti - I. Application of the coincidence site lattice (CSL)

theory to twinning problems in h.c.p. structures. *Acta Metall Mater*, *43* (6), 2325–2337, 1995b.

Song S. G., Gray III G. T. Structural interpretation of the nucleation and growth of deformation twins in Zr and Ti - II. TEM study of twin morphology and defect reactions during twinning. *Acta Metall Mater*, *43* (6), 2339–2350, 1995c.

Taylor G. I. Plastic strain in metals. *J Inst Metals*, *62*, 307–324, 1938-1939.

Teixeira J. D. C., Appolaire B., Aeby-Gautier E., Denis S., Cailletaud G., and Späth N. Transformation kinetics and microstructures of Ti17 titanium alloy during continuous cooling. *Material Science and Engineering A*, Volume 448, Issues 1-2:135-145, 2007.

Tomé C. N., Canova G. R., Kocks U. F., Christodoulou N., and Jonas J. J. The relation between macroscopic and microscopic strain hardening in F.C.C. polycyrstals. *Acta Metall*, *32* (10), 1637–1653, 1984.

Tomé C. N., Lehensohn R. A., and Kocks U. F. A model for texture development dominated by deformation twinning: application to zirconium alloys. *Acta Metall Mater*, *39* (11), 2667–2680, 1991.

Tomé C. N., Maudlin P. J., Lebensohn R. A., and Kaschner G. C. Mechanical repsonse of zirconium - I. Derivation of a polycrystal constitutive law and finite element analysis. *Acta Mater*, *49*, 3085–3096, 2001.

Tomé C. N., Lebensohn R. A. Self consistent homogeneization methods for texture and anisotropy. In D. Raabe, F. Roters, F. Barlat, & L. Q. Chen (Eds.), *Continuum scale simulation of engineering materials: fundamentals, microstructures, process applications* (pp. 473-499). Weinheim: Wiley-VCH Verlag GmbH & Co. KGaA, 2004.

Van Houtte P. Simulation of the rolling and shear texture of brass by the Taylor theory adapted for mechanical twinning. *Acta Metall*, *26* (4), 591–604, 1978.

Van Houtte P., Li S., and Engler O. Taylor-type homogenization methods for texture and anisotropy. In D. Raabe, F. Roters, F. Barlat, & L. Q. Chen (Eds.), *Continuum scale simulation of engineering materials: fundamentals, microstructures, process applications* (pp. 459–472). Weinheim: Wiley-VCH Verlag GmbH & Co. KGaA, 2004.

Van Houtte P., Kanjarla A. K., Van Bael A., Seefeldt M., and Delannay L. Multiscale modelling of the plastic anistropy and deformation texture of polycrystalline materials. *Eur J Mech A Solids*, *25*, 634–648, 2006.

Walpole L. J. On the overall elastic moduli of composite materials. *J Mech Phys Solids*, *17*, 235-251, 1969.

Wang H., Raeisinia B., Wu P. D., Agnew S. R., and Tomé C. N. Evaluation of self-consistent polycrystal plasticity models for magnesium alloy AZ31B sheet. *International Journal of Solids and Structures, 47*, 2905-2917, 2010a.

Wang H., Wu P. D., Tomé C. N., and Huang Y. A finite strain elastic–viscoplastic self-consistent model for polycrystalline materials. *Journal of the Mechanics and Physics of Solids, 58*, 594-612, 2010b.

Wang H., Wu P. D., Tomé C. N., and Wang J. A constitutive model of twinning and detwinning for hexagonal close packed polycrystals. *Materials Science & Engineering A, 555*, 93-98, 2012.

Wang W., Wang M., Jie Z., Sun F., and Huang D. Research on the microstructure and wear resistance of titanium alloy structural members repaired by laser cladding. *Optics and Lasers in Engineering*, Volume 46, Issue 11:810-816, 2008.

Williams D. N., Eppelsheimer D. S. A theoretical investigation of the deformaiton textures of titanium. *J Inst Metals, 81*, 553–562, 1952-1953b.

Williams J. C., Blackburn M. J. The identification of a non-basal slip vector in titanium and titanium-aluminum alloys. *Phys Status Solidi, 25*, K1–K3, 1968.

Williams J. C., Sommer A. W., and Tung P. P. The influence of oxygen concentration on the internal stress and dislocation arrangements in α titanium. *Metall Trans, 3*, 2979–2984, 1972.

Wu X., Kalidindi S. R., Necker C., and Salem A. A. Prediction of crystallographic texture evolution and anisotropic stress-strain curves during large plastic strains in high purity α-titanium using a Taylor-type crystal plasticity model. *Acta Mater, 55* (2), 423–432, 2007.

Xiaoli T., Haicheng G., Shufen Z., and Laird C. Loading mode dependence of deformation microstructure in a high-purity titanium single crystal oriented for difficult glide. *Mater Sci Eng A, 189*, 77–84, 1994.

Zaefferer S. A study of active deformation systems in titanium alloys: dependence on alloy composition and correlation with deformation texture. *Mater Sci Eng A, 344*, 20–30, 2003.